CFD modeling of biomass combustion and gasification in fluidized bed reactors

Yang, Miao

2023

Total number of authors:
1

CFD modeling of biomass combustion and gasification in fluidized bed reactors

CFD modeling of biomass combustion and gasification in fluidized bed reactors

by Miao Yang

LUND
UNIVERSITY

Thesis for the degree of Doctor of Philosophy
Thesis advisors: Prof. Xue-Song Bai, Dr. Hesameddin Fatehi and Dr. Leilei Xu
Faculty opponent: Prof. Fabien Halter

To be presented, with the permission of the Faculty of Engineering of Lund University, for public criticism at KC:A lecture hall of the Department of Energy Sciences on March 31, 2023 (Friday) at 10:00.

Organization		Document name	
LUND UNIVERSITY		**DOCTORAL DISSERTATION**	
Department of Energy Sciences P.O. Box 118, SE–221 00 LUND Sweden		Date of disputation 2023-03-31	
		Sponsoring organization Swedish Energy Agency (STEM) through KC-CECOST, Knut & Alice Wallenberg foundation, China Scholarship Council (CSC), Swedish National Infrastructure for Computing (SNIC)	
Author(s) Miao Yang			

Title and subtitle

CFD modeling of biomass combustion and gasification in fluidized bed reactors

Abstract

Biomass is an environmentally friendly renewable energy source and carbon-neutral fuel alternative. Direct combustion/gasification of biomass in the dense particle-fluid system is an important pathway to biomass energy utilization. To efficiently utilize biomass for energy conversion, a full understanding of biomass thermal conversion in lab/industrial-scale equipment is essential. This thesis aims to gain a deeper understanding of the physical and chemical mechanisms of biomass combustion/gasification in fluidized bed (FB) furnaces using computational fluid dynamics (CFD) simulations.

A three-dimensional reactive CFD model based on the Eulerian-Lagrangian method is developed to investigate the hydrodynamics, heat transfer, and gasification/combustion characteristics of biomass in multiple-scale FB furnaces. The CFD model considered here is based on the multi-phase particle-in-cell (MP-PIC) collision model and the coarse grain method (CGM). CGM is computationally efficient; however, it can cause numerical instability if the clustered parcels pass through small computational cells, resulting in the overloading of solid particles in the cells. To address this issue, a distribution kernel method (DKM) is proposed. This method is to spread the solid volume and source terms of the parcel to the surrounding domain. The numerical stiffness problem caused by the CGM clustering can be remedied using DKM. Validation of the model is performed using experimental data from various lab-scale reactors. The validated model is employed to investigate further the heat transfer and biomass combustion/gasification process.

Biomass pyrolysis produces a large variety of species in the products, which poses great challenges to the modeling of biomass gasification. A conventional single-step pyrolysis model is widely employed in FB simulations due to its low computational cost. However, the prediction of pyrolysis products of this model under varying operating temperatures needs to be improved. To address this issue, an empirical pyrolysis model based on element conservation law is developed. The empirical parameters are based on a number of experiments from the literature. The simulation results agree well with the experimental data under different operating conditions. The pyrolysis model improves the sensitivity of gasification product yields to operating temperature. Furthermore, the mixture characteristics of the biomass and sand particles and the effect of the operating conditions on the yields of gasification products are analyzed.

The validated CFD model is employed to investigate the fluidization, combustion, and emission processes in industrial-scale FB furnaces. A major challenge in the CFD simulation of industrial-scale FB furnaces is the enormous computational time and memory required to track quadrillions of particles in the systems. The CFD model coupling MP-PIC and CGM greatly reduces the computational cost, and the DKM overcomes the unavoidable particle overloading issue due to the refined mesh in complex geometry. The CFD predictions agree well with onsite temperature experiments in the furnace. The CFD results are used to understand the granular flow and the impact of operating conditions on the physical and chemical processes in biomass FB-fired furnaces.

Key words

Biomass combustion and gasification, CFD simulation, Fluidized bed furnace, Distribution kernel method, Empirical pyrolysis model

Classification system and/or index terms (if any)

Supplementary bibliographical information	Language English
ISSN and key title 0282-1990	ISBN 978-91-8039-513-7 (print) 978-91-8039-512-0 (pdf)

Recipient's notes	Number of pages 165	Price
	Security classification	

I, the undersigned, being the copyright owner of the abstract of the above-mentioned dissertation, hereby grant to all reference sources the permission to publish and disseminate the abstract of the above-mentioned dissertation.

Signature _____   Date _____2023-02-15_____

CFD modeling of biomass combustion and gasification in fluidized bed reactors

by Miao Yang

LUND
UNIVERSITY

A doctoral thesis at a university in Sweden takes either the form of a single, cohesive research study (monograph) or a summary of research papers (compilation thesis), which the doctoral student has written alone or together with one or several other author(s).

In the latter case the thesis consists of two parts. An introductory text puts the research work into context and summarizes the main points of the papers. Then, the research publications themselves are reproduced, together with a description of the individual contributions of the authors. The research papers may either have been already published or are manuscripts at various stages (in press, submitted, or in draft).

Contents

Acknowledgements

First of all, I would like to express my sincere gratitude to my main supervisor Prof. Xue-Song Bai, for providing me with the opportunity to delve into the scientific research field. I have greatly benefited from his rigorous scientific research attitude, the wealth of knowledge, and continuous enterprising spirit. Many memorable scenes, e.g., the valuable instructions, project discussion, and word-for-word revision of the article, will remain with me for the rest of my life.

My gratitude also goes to Dr. Hesameddin Fatehi and Dr. Leilei Xu for their valuable suggestions and article revision; to Dr. Robert-Zoltàn Szàsz for helping me solve many computer problems; to Prof. Magnus Genrup for assisting me with the registration issue before my arrival; to Prof. Johan Revstedt, Prof. Christer Fureby, and Dr. Rixin Yu, for imparting a great deal of knowledge on numerical modeling in their courses. My gratitude also goes to my co-authors, Dr. Shenghui Zhong for providing timely assistance when I was in dire need, and to Dr. Tian Li, Dr. Jingyuan Zhang, Prof. Terese Løvås, Peter Ottosson, and Dr. Seyed Morteza Mousavi, for providing valuable suggestions. I would also like to express my appreciation to Dr. Shijie and Dr. Leilei, as well as their families, Yuanyuan Cao and Nuo Xu, and Yang Liu and Ruirui, for creating many memorable moments in my daily life over the past four years. My office roommates, Morteza, and Francesco Pignatelli are both excellent and kind individuals who have brought much laughter to our office. When I first arrived in this unfamiliar country, I never forget the kind, friendly, and sunny office roommate, Michael Bertsch, who help me adjust to the new environment. I am also grateful to my living roommates, Dr. Yan Zhang and Dr. Xiufei Li, who took care of me in daily life and helped improve my programming skills, and to Qianyan Xu, for sharing a lot of delicious food with me, greatly improving my diet level.

Furthermore, I would like to express my gratitude to my colleagues in our group, Dr. Senbin Yu, Dr. Shijie Liu, Dr. Yaopeng Li, Dr. Li Guo, Dr. Haoran Zhao, Dr. Yuqian Chen, Sheng Feng, Yuchen Zhou, Mark Treacy, Yingdong Wang, Yipeng Li, and Longjuang Ji, who has been with me for a long time. It has been

an honor and a pleasure to work with and learn from all of you. Lots of thanks go to my Chinese friends, Heng Hu, who brought much joy into our department; Xiaoqiang Zhang, who mentored fitness for many friends; to Dr. Zhen Cao, Danan Yang, Dequan Xu, Yuxiang Lim, Zhan Liu, Shuo Yang, Qingfang Fan, and Wubin Wong, who created a friendly environment in the unfamiliar territory. I am also grateful to my friends, Yue Qiu, Zhe Xing, Zhiyong Wu, and Li Liu, for organizing many sports, which helped me stay healthy despite the heavy pressure of scientific research.

Lastly, I would like to extend my gratitude to my family. Thanks to my parents for their unwavering support and encouragement. Thanks to my brother and sister-in-law for their care for our parents in my absence. Thanks to my nieces and nephews for their love and support.

Popular science summary

Biomass, such as trees, crops, flowers, plants, etc., is found all over Earth. Dry biomass, just like coal, petroleum, and natural gas, can be used for burning, heating, cooking, and generating electricity. Unlike coal, it can grow quickly when trees are cut down. Carbon dioxide in the atmosphere is absorbed into biomass – thus, biomass is a renewable and carbon-neutral fuel. It is abundant on Earth and easily accessible. Thus, one can use biomass instead of coal for heat and power production because there is a finite amount of coal on the planet, and burning coal emits greenhouse gas and other pollutants into the atmosphere. A simple question is how does one get more heat from less biomass when it is burning? To answer this question, one has first to figure out what happens when biomass is burned.

Biomass combustion can be performed in a device called a fluidized bed (FB) furnace, in which a high-temperature nonreactive material, such as sand and limestone, reaches a state like boiling water by the upward air. To optimize the combustion system, one should do a series of experiments to see what are the best operating conditions. If the device is small, one can manufacture it easily. But, if the size of the device is tens of meters high, the cost of this experiment is relatively expensive. So, one wishes to have a "magic tool" that could show biomass burning without doing the experiments. Computational fluid dynamics (CFD) is the best "magic tool" to achieve it. This method is based on a series of mathematical equations, which is solved using a supercomputer to replicate a real-life scenario of biomass combustion. With this method, one can stop/start biomass burning at any time, or one can go anywhere in the furnace and see what happens there.

This method is powerful and cheap; however, there are two sides to every coin. In the process of developing this method, there are many challenges. Imagine a device in which a large number of small biomass particles are constantly moving and burning. How does one replicate this process in a computer most accurately? An ideal way is to track each particle, where it goes, and how it burns. This is however unrealistic because the number of particles is incalculable, especially in large devices. One uses a method that clusters a number of particles into different groups. This method is called the "coarse grain method" (CGM). Only one particle in the group is tracked, and all other particles are represented by this particle. The computational time is therefore significantly reduced. Just like thousands of families/groups travel by car, bus, or train, and live in hotel rooms, one can figure out the movement and location of each individual simply by locating the vehicles or hotel of each family/group. The method,

however, also introduces some problems. One assumes the family/group will live in the same room all the time in this method. Let's say there are thousands of families/groups living in a hotel with various size rooms. The large room can accommodate any group while the small room cannot. The conventional method is to throw out the extra members in the small room, and the families/groups will complain. I propose in this thesis a method that spreads the member of the families/groups living in the small rooms to the neighboring rooms. I call this method the "distribution kernel method" (DKM).

In addition to the problems discussed above, another challenge exists in biomass combustion. Biomass combustion can be divided into three stages: evaporation of water, first-stage chemical reactions, which are called pyrolysis, and second-stage chemical reactions, which are called charcoal burning. In the first stage, biomass pyrolysis produces a lot of different kinds of gases, for example, hydrogen, carbon monoxide, or methane. In fact, the masses of these different gases are different at different operating temperatures of the devices. Just like cooking, different temperatures will generate different flavors. In the conventional method, biomass burning produces the same masses of these gases at various operating temperatures. It's a poor and inaccurate approach. In this thesis, I considered more constraints to simulate the masses of different pyrolysis gases. Thus, one can better replicate biomass combustion at different temperatures. After implementing the developed methods and models in a computer code, I have used this 'magic tool' to replicate and simulate biomass combustion in large-size devices that are tens of meters high. One industrial furnace that I simulated is the Kraftringen FB furnace at Örtofta. Few people who do biomass-burning research have been able to do it.

The main contribution of this thesis is to develop the "magic tool" to replicate/simulate biomass burning in industrial devices. Firstly, I used the group method, namely CGM, to reduce the computational time and used the neighbor-sharing method, namely DKM, to improve the computational accuracy. Secondly, I improved the prediction accuracy of gases produced from biomass pyrolysis. Thirdly, I used the "magic tool" to replicate/simulate biomass burning in large-scale industrial FB furnaces. The work aids the understanding of how chemical energy from biomass is converted to heat and power and helps engineers in the industry to develop strategies to improve the performance of their devices, e.g., reduction of pollutant emission from their devices.

Abstract

Biomass is an environmentally friendly renewable energy source and carbon-neutral fuel alternative. Direct combustion/gasification of biomass in the dense particle-fluid system is an important pathway to biomass energy utilization. To efficiently utilize biomass for energy conversion, a full understanding of biomass thermal conversion in lab/industrial-scale equipment is essential. This thesis aims to gain a deeper understanding of the physical and chemical mechanisms of biomass combustion/gasification in fluidized bed (FB) furnaces using computational fluid dynamics (CFD) simulations.

A three-dimensional reactive CFD model based on the Eulerian-Lagrangian method is developed to investigate the hydrodynamics, heat transfer, and gasification/combustion characteristics of biomass in multiple-scale FB furnaces. The CFD model considered here is based on the multi-phase particle-in-cell (MP-PIC) collision model and the coarse grain method (CGM). CGM is computationally efficient; however, it can cause numerical instability if the clustered parcels pass through small computational cells, resulting in the overloading of solid particles in the cells. To address this issue, a distribution kernel method (DKM) is proposed. This method is to spread the solid volume and source terms of the parcel to the surrounding domain. The numerical stiffness problem caused by the CGM clustering can be remedied using DKM. Validation of the model is performed using experimental data from various lab-scale reactors. The validated model is employed to investigate further the heat transfer and biomass combustion/gasification process.

Biomass pyrolysis produces a large variety of species in the products, which poses great challenges to the modeling of biomass gasification. A conventional single-step pyrolysis model is widely employed in FB simulations due to its low computational cost. However, the prediction of pyrolysis products of this model under varying operating temperatures needs to be improved. To address this issue, an empirical pyrolysis model based on element conservation law is developed. The empirical parameters are based on a number of experiments from the literature. The simulation results agree well with the experimental data under different operating conditions. The pyrolysis model improves the sensitivity of gasification product yields to operating temperature. Furthermore, the mixture characteristics of the biomass and sand particles and the effect of the operating conditions on the yields of gasification products are analyzed.

The validated CFD model is employed to investigate the fluidization, combustion, and emission processes in industrial-scale FB furnaces. A major challenge

in the CFD simulation of industrial-scale FB furnaces is the enormous computational time and memory required to track quadrillions of particles in the systems. The CFD model coupling MP-PIC and CGM greatly reduces the computational cost, and the DKM overcomes the unavoidable particle overloading issue due to the refined mesh in complex geometry. The CFD predictions agree well with onsite temperature experiments in the furnace. The CFD results are used to understand the granular flow and the impact of operating conditions on the physical and chemical processes in biomass FB-fired furnaces.

Nomenclature

Abbreviations

1-D	One-dimensional
2-D	Two-dimensional
3-D	Three-dimensional
BFB	Bubbling fluidized bed
BGK	Bhatnagar, Gross, and Krook
CAM	Cube averaging method
CFD	Comutational fluid dynamics
CFL	Courant–Friedrichs–Lewy
CGM	Coarse grain method
DAF	Dry ash free
DBM	Diffusion-based method
DCFB	Dual circulating fluidized bed
DEM	Discrete element method
DFB	Dual fluidized bed
DKM	Distribution kernel method
DNS	Direct numerical simulation
DPM	Discrete particle model
DPVM	Divided particle volume method
DVC	Depolymerization, vaporization, and crosslinking
EAR	Equivalent air ratio
FB	Fluidized bed
FBG	Fluidized bed gasifier
FG	Functional group
FVM	Finite volume method
FWO	Flynn–Wall–Ozawa
GFEC	Gross final energy consumption
GHG	Greenhous gas
KAS	Kissinager-Akahira-Sunose
KTDG	Kinetic theory of dense gases
KTGF	Kinetic theory of granular flows
LSD	Linear spring-dashpot
MM	Mixture model
MP-PIC	Multi-phase particle-in-cell
MPI	Message-passing interface
PaSR	Partially Stirred Reactor
PCM	Particle centroid method
PISO	Pressure implicit with splitting of Operator
PSD	Particle size distribution
RANS	Reynolds averaged Navier-Stokes
SIMPLE	Semi-implicit method for pressure-linked equations
SNCR	Selective non-catalytic reduction

SR   Steam-to-biomass ratio   TFM   Two fluid model

SSP   Same size parcel

SSW   Same statistic weight   TGM   Two-grid method

Chapter 1

Introduction

1.1 Motivation

Global warming, caused by greenhouse gas (GHG) emissions, is a significant societal challenge. Since the Industrial Revolution, the global average temperature has increased by 1.01 °C. From 1880 to 1980, the temperature rose by an average of 0.07 °C per decade, but in the last 40 years, it has risen by an average of 0.18 °C per decade [1], making it imperative to take action to mitigate global warming.

Fossil fuels, e.g., coal, petroleum, and natural gas, are the biggest contributors to GHG emissions, accounting for 81% of total energy consumption, as shown in Fig. 1.1. In 2019, the gross final energy consumption (GFEC) of all energy
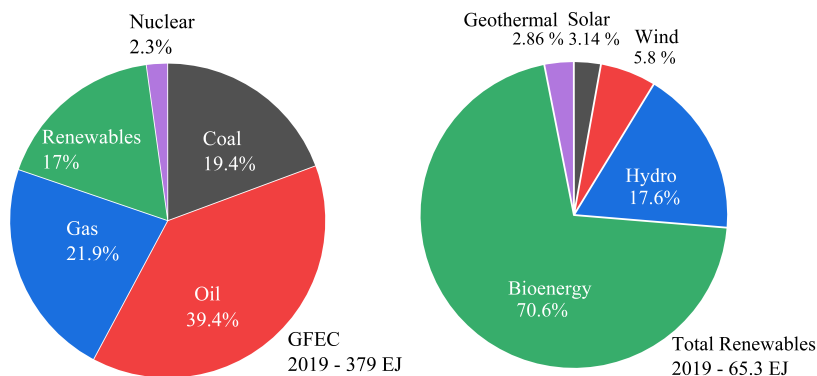
Figure 1.1: Global final energy consumption (GFEC) in 2019 [2].

sources was 379 EJ. GFEC is defined as the total final consumption of all energy sources, including electricity and heat consumption at all end-use sectors. Replacing fossil fuels with renewable energy can significantly reduce GHG emissions. In 2019, 17% of gross final energy consumption came from renewables, e.g., solar, wind, geothermal, and biomass. Sweden is among the world's leaders in the use of renewable energy, with 41% of the country's total energy supply and 58% of final energy consumption coming from renewables, see Figure 1.2. This trend is accelerating, with renewable energy accounting for 48.5% in 2021 [2].

Table 1.1: Domestic supply of biomass in continents in 2019 [2]. Note: All values except the solid ratios are in EJ.

Region	Total	Municipal Waste	Industrial Waste	Biogas	Liquid Biofuels	Solid Biofuels	Solid Ratio
Africa	16.0	0.00	0.00	0.00	0.00	16.0	1.000
Americas	11.6	0.29	0.07	0.19	3.00	8.05	0.694
Asia	21.2	0.20	0.55	0.50	0.62	19.3	0.91
Europe	7.49	0.92	0.52	0.72	0.63	4.70	0.628
Oceania	0.25	0.00	0.00	0.02	0.01	0.22	0.88
EU-28	6.45	0.85	0.19	0.70	0.63	4.07	0.63

In renewable energy share, 67.2% is biomass energy, as shown in Fig. 1.1. Biomass energy is derived from solar energy stored in living organisms in the form of chemical energy, either directly or indirectly through the photosynthesis of plants. It is a preferred alternative to fossil fuels due to its abundance, short regeneration cycle, and easy accessibility [3, 4]. Biomass can be used for various applications, such as heat or power generation, chemical synthesis, and producing nanomaterials. It can be converted into liquid, gaseous, and solid fuels through various chemical, physical, and biological processes [5]. In 2019, solid biofuels made up over 80% of bioenergy in Africa, Asia, and Oceania, while in the Americas, Europe, and EU-28, it was around 60%, see Table 1.1. In Sweden, around 70% of renewable energy is biomass energy, with 80% being solid biomass. The country is rich in biomass resources, with around 70% of Sweden's land area being forest land and providing ample reserves.

In Sweden's Integrated National Energy and Climate Plan submitted in 2020, the government set a goal of becoming the first fossil fuel-free country in the world and taking the lead on environmental and climate issues. The overall plan includes reducing GHG reduction by 63% by 2030, 75% by 2040, and achieving net-zero GHG emissions by 2045, compared to 1990 levels [6]. As an alternative to fossil fuels, biomass can play a significant role in reducing GHG emissions and achieving the objectives outlined in the UN's Paris Agreement. Research on biomass energy, particularly solid biomass fuel, is of great significance for
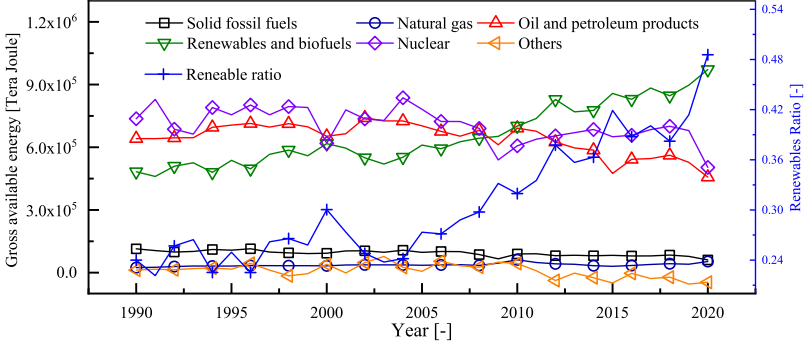
Figure 1.2: Gross available energy from different sources in Sweden [7]. Note: Renewable ratio in this figure is the ratio of renewables and biofuels to the total gross available energy.

replacing fossil fuels, fulfilling Sweden's goals, and mitigating global warming.

Biomass combustion is an important energy conversion technology for generating heat and power, supplying the daily needs of society. In 2019, 1.17 EJ of global heat was produced from biomass energy, with 53% coming from solid biomass sources and 25% from municipal solid waste [6]. In Sweden, biomass accounted for around 70% of the fuel/heat supply, excluding heat pumps and electric heating. Despite humans having used biomass for heating for thousands of years and extensive research being conducted on biomass combustion in recent decades, the underlying physical and chemical processes are not fully yet understood. Gasification, a thermochemical conversion process, is an alternative to combustion. In gasification, biomass is converted into a gaseous energy carrier composed of permanent and non-condensable gases through reactions with a gasification agent (air, oxygen, or steam water) at high temperatures (600–1100 °C) [8–11]. Gasification has several advantages over combustion, including lower corrosion, higher fuel throughput per unit area, and lower sensible heat [8]. It can convert biomass fuel into higher-value gaseous, e.g., H_2, CH_4, and CO, with 85%–90% thermal efficiency. Improving gasification technology is of great significance for expanding the use of biomass energy.

A comprehensive understanding of the physical and chemical mechanisms involved in biomass combustion and gasification is vital for efficiently utilizing biomass fuel and mitigating global warming.

1.2   Biomass combustion/gasification in FB furnaces

In industrial production, there are different ways to mix solids and gas streams, such as fixed beds, moving beds, entrained flow beds, and fluidized beds. Proper contact between the solid and gas phases is essential to designing the gas-solid system. Since the 17th century, fluidized bed (FB) technology has been developed to address the energy crisis. In recent decades, hydrodynamic, chemical, and physical processes in fluidized beds have been extensively investigated. The solid fuels in FB furnaces undergo thermo-conversion with a high temperature of inert material, such as sand, ash, and limestone, which is fluidized by upward fluid flow. The inert material in the furnace does not participate in chemical reactions but provides heat transfer to fuels.

Table 1.2: Comparison of gas-solid reaction systems [12, 13].

Characteristics	Fixed bed	Moving bed	Entrained flow	Fluidized bed	Circulating fluidized bed
Heterogenous catalytic gas-phase reactions	Only for slow deactivation catalysis; Catalysis attrition negligible; Plug flow of gas ensures high gas conversion.	For large granular rapid deactivation catalysis;	Gas in virtually plug flow; high conversion possible; catalysis.	For small granular or powder non-friable catalyst; Can handle rapid deactivation of solid.	Suitable for rapid reactions; Attrition of catalyst is serious.
Gas-solid reactions	Unsuitable for continuous operations, while batch operations yield nonuniform products	For fairly uniform size feed with little or no fines.	Possible for fast reactions; Recycle of unreacted fines often difficult.	Flexible fuel and wide range of fuel size; Continuous operations.	Suitable for rapid reactions; Recirculation of fines is crucial
Heat transfer	Serious temperature control problem; Large temperature gradient; Danger of hot spots; Poor heat exchange.	Temperature gradient can be controlled with proper gas flow; Poor heat exchange;	Axial temperature gradients can be held within limits by high solid circulations; Properties intermediate between fluidized bed and moving bed.	Excellent temperature control ability; Uniform temperature distribution; Efficient heat exchange.	Temperature gradients in direction of solid flow can be minimized by sufficient circulation of solid.
Particle size	Large particles (6 – 20 mm)	Medium size (2 – 6 mm)	fine particle (0.02 – 0.5 mm) with narrow size distribution	Broad particle size distribution (0.02 – 6 mm)	Broad particle size distribution (0.02 – 6 mm)

Compared to other reactors, fluidized bed furnaces have desirable and undesirable characteristics in the industrial application, as shown in Table 1.2. Fluidized bed furnaces have several advantages [13–15]:

- Operating conditions of fluidized bed furnaces can be controlled continuously and stably with easy handling due to the fluid-like flow of particles.

- A wide range of solid fuel particle sizes can be applied in fluidized bed furnaces resulting in high fuel flexibility.

- The mixture of fuel particles and inert materials is rapid and uniform, resulting in nearly isothermal conditions for fuel particles throughout the reactor.

- It can be operated on a large-scale furnace.

- Heat transfer efficiency between gas and solid phases is high due to high contact areas.

- The circulating system makes it possible to remove the products and add solid materials.

Against those advantages are several disadvantages [13–15]:

- Erosion of pipes and vessels from abrasion by solid particles may be severe.

- Non-fluidization due to the agglomeration of solids may occur during fluidized bed operations.

- The formation and collapse of gaseous bubbles lead to inefficient contact and nonuniform residence time for solid particles in the reactors.

- The separation of solid particles requires more complex equipment and controlling systems resulting in expensive costs.

Fluidized bed furnaces have wide applications in the following fields [13–15]:

- Combustion of solid (e.g., coal, biomass, waste fuels, domestic waste, and plastics), liquid, and gas fuels;

- Cooling of flue gases, steam, and hot fluids by heat exchange with the fluidized bed;

- Combustion takes place in one furnace, and heat transfer in another place;

- Production of steam to generate electricity;

- Application of fluidized bed boilers in locomotives and ships;

- Generation of the high-temperature gas/hot fluid.

1.2.1 Classification of FB furnaces

Fluidization in FB furnaces is a process where solid particles are suspended in a gas or liquid in an upward direction [16], creating a fluid-like state of the particles [17]. The fluidization phenomenon is dependent on various factors, e.g., the properties of particles (such as their density difference, and particle size),
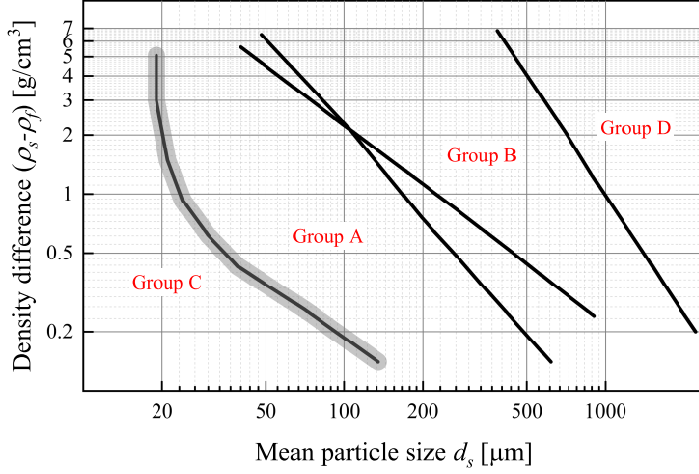
Figure 1.3: Geldart's particle classification diagram for fluidization by air [19]. Note: The scale of the coordinates is log2.

and the superficial gas velocity [18]. The types of particles in the fluidization can be classified according to their properties.

Fig. 1.3 shows the particles with various fluidization behaviors fall into four clearly recognizable groups (Groups A, B, C, and D) [19]. The classification is characterized by mean particle size d_s and density difference (ρ_s-ρ_g) relative to the fluid, where ρ_s and ρ_g denote the density of the particle and fluid, respectively. Group A particles are small or have a low material density and fluidized well, showing bed expansion before bubbling formation. Group B particles have a mean size of $40 < d_s < 500$ µm and a density difference of $1.4 < \rho_s\text{-}\rho_g < 4$ g/m^3. Bubbles form at or slightly above the minimum fluidization velocity and collapse quickly if the gas supply is cut off. Most bubbles rise faster than the interstitial gas velocity and the bubble size is linear with the bed height and excess gas velocity (U_g-U_{mf}), where the U_g and U_{mf} denote the gas superficial velocity and minimum fluidization velocity, respectively. Group C particles are extremely difficult to fluidize due to high interparticle forces, resulting in poor particle mixing and heat transfer. Group D particles are large or very dense and the bubbles rise more slowly than the interstitial fluidizing gas, causing turbulence but poor solids mixing.

The flow patterns of fluidization are very complex, and one or more patterns may occur during an operating condition, increasing the difficulty of the fluidization mechanism analysis. Figure 1.4 shows the internal relationship between various fluidization modes and superficial gas velocities. With increasing gas velocity U_g, fluidization goes through processes of a fixed bed, bubbling (slugging), turbulent, fast fluidization, and dilute/dense pneumatic conveying. The
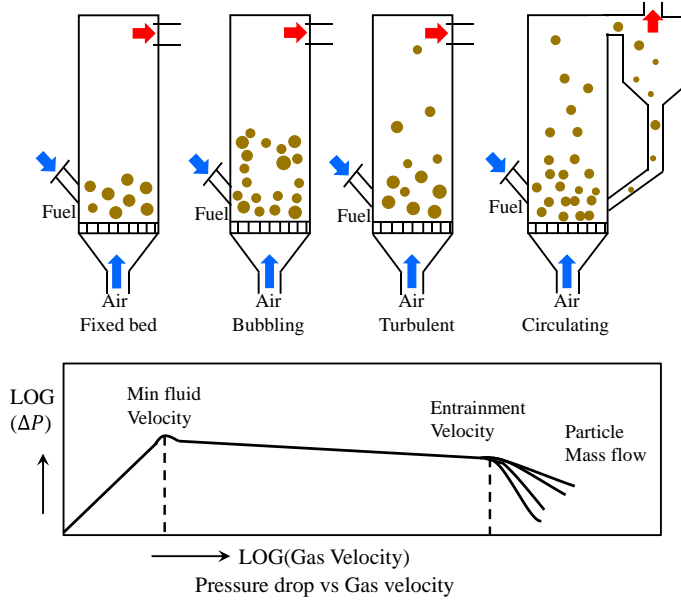
Figure 1.4: Type of fluidized bed [20]. The figure is reproduced with permission from the publisher.

minimum fluidization velocity U_{mf} is the gas velocity at which the interaction between the fluid and particles is balanced by the weight of the particles. The fixed bed is the state of $U_g < U_{mf}$. With the increase in gas velocity, i.e., $U_g \geqslant U_{mf}$, bubbles start to form and rise in the bed with small particles. Bed expands significantly before the formation of bubbles while for a bed with a larger particle diameter (Geldart B particle), the bubbles start to form as soon as the bed is fluidized. With further increase in the gas velocity, rising velocity and size of bubbles increase. When the bubble diameter is $(0.3 - 0.6)D$, the bed slugs, in which D is the column diameter of the reactor. The slug can be divided into axisymmetric, squared-nose, and wall slug. The type of slug flow in a fluidized bed depends on particle type, particle size, bed diameter, and the wall of the column. The slug flow turns into turbulence with a further increase in gas velocity followed by the random fluctuation of pressure drop. The turbulent regime is marked by the absence of bubbles and slugs in the bed. It is followed by violent movement of elongated and distorted voids and particles. In this case, i.e., U_g is larger than the minimum velocity of the dilute phase pneumatic conveying, the regime at which pressure fluctuation is relatively constant and is marked as pneumatic conveying.

Based on the fluidized state, fluidized bed furnaces can be divided into fixed beds, bubbling beds, turbulent beds, and circulating fluidized beds. In recent

years, spout fluidized beds and dual circulating fluidized beds have been developed and widely used as well. Bubbling fluidized beds are first-generation fluidized beds while circulating fluidized beds in fast fluidization regimes, see Figure 1.5, are second-generation fluidized beds. The bubbling fluidized bed reactor is comprised of the following basic components [14]:

- A fuel supply system involving fuel preparation and transport, controlling of mass flow rate;

- An inert material supply system involving inert material transport and controlling of mass flow rate;

- A cold startup system and an air distribution system;

- A fluidized bed furnace and a system for re-circulation of unburned fuel particles;

- A water cooling system and a flue gas cleaning system;

- An inert material removal system used for removing ash/large-size inert material from the furnace.

Figure 1.5: Illustration of the loop in circulating fluidized bed furnace [21]. The figure is reproduced with permission from the publisher.

The basic components and systems of a circulating fluidized bed furnace are as follows:

- A fuel supply system used for fuel handling and preparation;

- A furnace and an air distribution system for the primary, and secondary/tertiary air supply;

- A cold start-up system and cyclones used for separating and re-circulating solid materials;

- Pneumatic valves, and external heat exchange with the fluidized bed;

- Convective heat-transfer surface, a flue gas cleaning system, and a water-cooling system.

Fluidized bed furnaces are widely employed in coal/biomass combustion and gasification due to their advantages, including stable low-temperature combustion operation, high combustion efficiency, fuel flexibility, and low environmental impact [22, 23]. Multi-scale and multi-physiochemical processes occur simultaneously in FB furnaces, such as hydrodynamics of dense gas-solid flow, particle collision, heat and mass transfer, radiation, homogeneous and heterogeneous chemical reactions, and turbulent combustion. These physicochemical processes are highly influenced by the properties of the fluidized bed, the bed material, and the biomass fuel. Understanding the fluidization mechanism in depth is essential to the efficient utilization of fluidized bed technology.

1.2.2 Biomass thermo-chemical conversion

Biomass particles are complex in both chemical compositions and physical structures. They are made up of 38–50% of cellulose, 23–32% of hemicellulose, 15–25% of lignin, and 5–13% of other components (i.e., inorganic species and extractives) [24, 25]. According to the proximate analysis, biomass includes moisture, volatile matter, tar, fixed carbon, and ash. In decreasing order of mass contents, the elements in biomass are commonly C, O, H, N, Ca, K, Si, Mg, Al, S, Fe, P, Cl, Na, Mn, and Ti [26]. In addition, the porous structure of biomass gives it anisotropic properties, with thermal conductivity across the grain direction being approximately one-third that of along the grain direction. In contrast, the diffusion to gas flow across the wood grain is much higher than that in the other two directions [27]. In a combustor/gasifier, a biomass particle undergoes a series of conversion processes, including initially drying and pyrolysis (devolatilization), subsequently partial oxidation of char and volatile, and finally, char combustion/gasification through reaction with an agent. Drying is an important step in the pretreatment of biomass for second-generation thermo-chemical conversion, as fresh biomass typically contains 30-60 wt% moisture

content that needs to be dried to about 10–15 wt% [28]. The following process is the thermal decomposition of dried biomass in the absence of air/oxygen, producing gaseous products, liquid (tar and other organics), and solid (charcoal and ash). Finally, char particles are converted to gaseous products and ash through reactions with surrounding agents at the surface. The chemical composition and physical structure of biomass, turbulence, and operating conditions interact with each other, posing great challenges to uncovering underlying mechanisms of biomass combustion/gasification in FB furnaces.

1.3 Recent research on biomass combustion and gasification in FB furnaces

Research on physical and chemical processes in FB furnaces has been extensively conducted in recent decades. Two main methods, experimental and numerical methods, are employed to investigate the mechanisms of biomass combustion and gasification in FB furnaces.

1.3.1 Experimental research

The experimental study plays a crucial role in revealing the mechanisms of multi-scale fluidized bed furnaces, e.g., hydrodynamic, chemical conversion, and formation and emission of pollutants [29–32]. Leckner et al. [33–35] investigated the characterization of fluidization regimes using time-series analysis of pressure fluctuations and found this method effectively revealed the structure of cold particle-fluid flow at the macro level. Larsson et al. [36] investigated the thermochemical conversion of solid fuels through steam gasification in different dual fluidized beds (DFBs) and found a strong correlation between the availability of intermediate products in the reaction environment and the quality of the product gas. Hermann et al. [37] compared the H_2, CO, and CH_4 conversion processes in two different oxygen carriers in a 120 kW dual circulating fluidized bed (DCFB) reactor. A natural oxygen carrier, i.e., ilmenite, was shown to improve the conversion efficiency compared to a fabricated Ni-based oxygen carrier. Konttinen et al. [38] studied the conversion of fuel nitrogen to NO for a wide range of fuels in a lab-scale fluidized bed, ranging from coal-type fuels to peat, biomass, and wastes. A NO formation tendency database is formed by analyzing the combustion flue gases. It showed that nearly all reactive nitrogen (forming NO) in the biomass is released from the fuel during pyrolysis. Zhou et al. [39] studied the mechanisms of nitric oxide (NO) formation and reduction,

in which the volatile nitrogen was assumed to be NO, NH_3, HCN, and HNCO, and char nitrogen is converted to NO during char oxidation. Mahmoudi et al. [40] investigated NO_x formation and selective non-catalytic reduction (SNCR) in a lab-scale fluidized bed combustor of biomass. The SNCR reaction kinetics mechanisms using ammonia or urea predicted the overall $deNO_x$ yield very well at various operating temperatures and NH_3/NO_x ratios. In particular, Vainio et al. [41] conducted an experiment on the fate of fuel nitrogen in a full-scale bubbling fluidized bed (BFB) boiler. The main components of nitrogen species at various heights were measured and analyzed in detail. In those studies, most of the research on the analysis of the gas composition was based on the experimental data at the reactor outlet in lab-scale/semi-industrial scale FB furnaces [42–45]. The small-scale fluidized beds are difficult to reflect the complexity of industrial fluidized beds. The gas analysis at the outlet fails to fully reveal the formation mechanism of pollutants, e.g., biomass combustion in fluidization regimes, and the effect of the secondary and tertiary air on the emissions. Hence, larger-scale experimental studies, like the research of Vainio et al. [41], will help uncover the formation and reduction mechanisms of the pollutant in industrial-scale fluidized bed boilers.

Table 1.3: The ultimate analyses of the biomass fuels in gasifiers. Data points from [46–53].

Items	C [wt%]	H [wt%]	O [wt%]	N [wt%]	Exp. [-]
1	49.33	6.06	44.57	0.04	Erkiaga et al. [46]
2	51.34	5.98	42.5	-	Hofbauer et al. [47]
3	47.16	5.67	40.73	0.05	Koppatz et al. [48]
4	54.46	5.99	39.31	0.24	Nguyen et al. [49]
5	46.65	5.55	38.74	-	Rapagna et al. [50]
6	53.6	6.10	40.2	0.1	Sampron et al. [51]
7	40.06	5.61	39.88	0.9	Song et al. [52]
8	51.30	5.81	42.6	< 0.2	Zhang et al. [53]

Experimental research on the gasification of biomass has been also extensively conducted in recent decades. Shahbeik et al. [54], Cortazar et al. [55] and Oliveira et al. [56] have reviewed a vast literature on the recent progress of biomass gasification. The effect of various operating parameters on biomass gasification, the strategies for removing tar, and the chemical synthesis of biomass gasification are discussed in the literature. However, the gasification mechanisms have not fully been understood. As shown in Figure 1.6, the mole fractions of main gasification products based on various experiments are compared. Experiments have the same biomass material and approximate operating conditions. The biomass is pine wood, the operating temperature is 700 $\sim$ 1000 °C, and the ratio
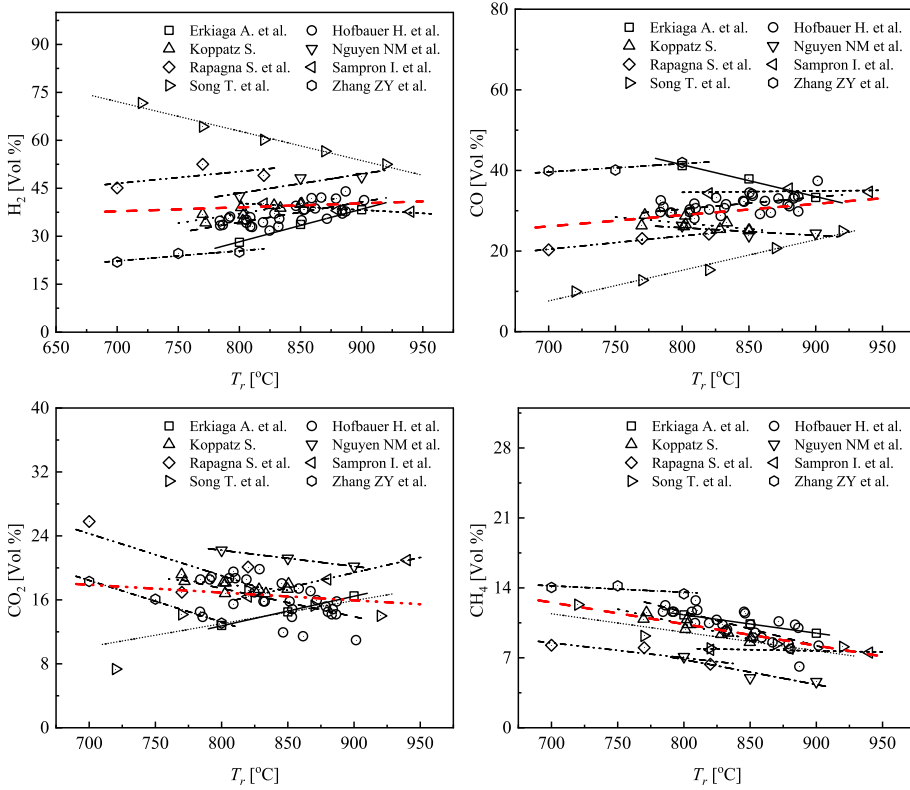
Figure 1.6: Mole fraction of H_2, CO, CO_2 and CH_4 based on the experiments of Erkiaga et al. [46], Hofbauer et al. [47], Koppatz et al. [48], Nguyen et al. [49], Rapagna et al. [50], Sampron et al. [51], Song et al. [52] and Zhang et al. [53] under different reactor varying the operating temperature T_r with SR = 0.9 ± 0.3.

of steam to biomass is $0.6 \sim 1.2$. The ultimate analyzes of the biomass fuel are presented in Table 1.3. An interesting finding is that the trends of product yield across the range of reactor operating temperatures are contradictory in different literature. For H_2, the mole fraction in the experiment of Song et al. [52] and Sampron et al. [51] decrease while those in the remaining literature increase with increasing temperature. The trends of CO and CO_2 are similar to that of H_2, in which the values have various trends across the operating temperatures, while the values of CH_4 in all experiments have the same trends. The reasons for the contradictory results could be the difference in biomass fuel properties, e.g., size, moisture, and the treatment of the particles. A clear conclusion is that the chemical mechanisms of gasification need to be further investigated.

Based on the experimental research on the large/lab-scale FB, it can be found that the experimental research focuses more on the phenomena and mechanism of the granule-fluid flow at the furnace level. However, details about thermo-

chemical conversion physics inside FB need to be studied. The experimental methods have the disadvantage of high cost and long research cycles. Thus, further research on developing efficient methods is required to reveal the complex physical and chemical processes in FB furnaces.

1.3.2 Numerical simulation of biomass combustion and gasification in FB furnaces

Compared to the experimental approach, the computational fluid dynamics (CFD) approach is considered an efficient, economical, and powerful method to investigate the physical and chemical mechanisms in multi-scale FB furnaces [21, 57–59]. In the past decades, the CFD simulations of biomass combustion and gasification in FB furnaces, especially industrial-scale FB furnaces, are still lacking.

Table 1.4: CFD simulations of FB. D represent dimensional, H - Hydrodynamic, T - thermal, R -gasification/combustion

Refs	Scale	D	Model	subModel	H	T	R
J. Gu et al. [60]	12 MWth	3D	E-L	MP-PIC	✓	✓	✓
D.L. Kong et al. [61]	lab-scale	3D	E-L	MP-PIC	✓	✓	✓
J.J. Lin et al. [62]	1 MWth	3D	E-L	MP-PIC	✓	✓	✓
S.L. Yang et al. [63]	0.3 MWth	3D	E-L	MP-PIC	✓	✓	✓
S.Y. Li et al. [64]	lab-scale	3D	E-E	TFM	✓	✓	✓
L. Cai et al. [65]	lab-scale	3D	E-E	TFM	✓	✓	✓
E. Ghadirian et al. [66]	lab-scale	3D	E-E	TFM	✓	✓	✓
S. Wang et al. [67]	lab-scale	3D	E-L	MP-PIC	✓	✓	✓
S. Wang et al. [59]	600 MWth	3D	E-L	DEM	✓	✗	✗
K. Luo et al. [68]	lab-scale	3D	E-L	DEM	✓	✗	✗
B.H. Lee et al. [69]	550 MWth	3D	E-L	MP-PIC	✓	✗	✗
Q.Y. Tu et al. [70]	lab-scale	3D	E-L	MP-PIC	✓	✗	✗
T. Kadyrov et al. [71]	lab-scale	3D	E-L	MP-PIC	✓	✗	✗
S.L. Yang et al. [72]	lab-scale	3D	E-L	MP-PIC	✓	✗	✗
A. Muhammad et al. [73]	lab-scale	3D	E-L	MP-PIC	✓	✗	✗
Q. Ma et al. [74]	lab-scale	3D	E-L	MP-PIC	✓	✗	✗
J.S. Li et al. [75]	lab-scale	3D	E-L	MP-PIC	✓	✗	✗
Y. Liu et al. [76]	lab-scale	3D	E-E	TFM	✓	✗	✗
A. Nikolopoulos et al. [77]	lab-scale	3D	E-E	TFM	✓	✗	✗
B.Y. Lu et al. [78]	lab-scale	2D	E-E	TFM	✓	✗	✗
C.B. Dinh et al. [79]	lab-scale	2D	E-E	TFM	✓	✗	✗
B.Y. Deng et al. [80]	350 Mw	1D	✗	✗	✓	✓	✓

Table 1.4 summarizes the recent literature on simulations in FB furnaces. The focus has been on simulating biomass combustion/gasification in lab-scale FBs or the cold flow in large-scale FBs. In these studies, one-dimensional (1-D) and

two-dimensional (2-D) simulations, which take into account simplified physical and chemical processes of the gas phase and particle phase, are frequently reported [78–82]. 1-D and 2-D models have the advantages of high computational efficiency, easy implementation, and flexible application. They, however, only consider the variation of the physical parameters in the vertical direction of furnaces and assume a uniform distribution of the physical parameters on the horizontal cross-section [80]. Three-dimensional (3-D) simulations of lab/industrial-scale FB furnaces, which take into account the detailed granular motion and thermochemical processes of the particle and gas phases, are desirable but rarely performed. There are several challenges in modeling the solid fuel combustion process in FB furnaces, particularly industrial-scale CFB furnaces, such as a huge number of particles resulting in expensive computational cost, large particles in small-size grids resulting in numerical instability, and complex chemical kinetic mechanisms involved in the devolatilization, heterogeneous char reactions and homogeneous gas-phase reactions. To overcome these challenges, the development of an efficient, high-accuracy, and robust 3D CFD model is essential.

The CFD approach is primarily based on several sub-models employed to describe the system. As shown in Figure 1.7, there are several sub-models commonly used in numerical simulations of the gas-solid flow, involving the conservation equations of gas and solid phases, collision models, and coupling models between gas and solid phases. The Euler-Euler approach and the Euler-Lagrange approach are the two main CFD categories to simulate the physical and chemical processes in FB furnaces.
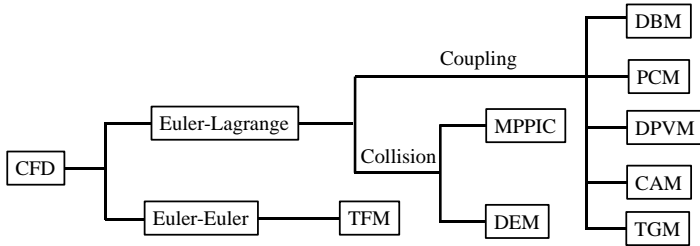
Figure 1.7: Models for numerical simulation of gas-solid two-phase flow.

In the Euler-Euler approach, both gas and solid phases are considered macroscopic continuous phases. The particle-fluid behavior is modeled using mass, momentum, and energy balance equations that are closed with constitutive relations and initial and boundary conditions [83–85]. To model fluid-solid interaction, the two-fluid model (TFM), which is developed based on the Euler-Euler framework [83], has been extensively employed due to its low computational cost

[86–97]. However, the model fails to describe the properties of the solid phase at the individual particle level, making it challenging to consider the particle type and size distribution. The use of volume averaging and interpolation methods for both gas and solid phases may lead to accumulated numerical error, as well as a mesh-dependent solution. In a study by Wang et al. [98], the TFM model was used to predict the bed expansion of Geldart B and D particles in a fluidized bed; however, it failed to accurately describe the hydrodynamics of Geldart A particles due to its limited resolution at that scale.

In the Euler-Lagrange approach, the gas phase is treated as a continuous phase, while the solid phase is considered as a discrete phase at the microscopic level [99]. This approach includes two models: discrete element method (DEM) [100] and multi-phase particle-in-cell (MP-PIC) method [84]. Unlike the Euler-Euler framework, the Euler-Lagrange approach can track each particle individually and take into account the properties of the particles, such as diameter, density, velocity, temperature, and chemical composition, with high accuracy [101]. This, however, leads to a sharp increase in computational cost, especially when considering particle collisions. In the DEM model, the collision force for each individual particle is calculated based on the interaction between all the individual particles in the system, providing high accuracy. However, this model becomes computationally infeasible for FB furnaces that involve quadrillion or more particles. To reduce the computational cost, efforts have been made to develop high-efficiency simulations of dense gas-solid reacting flow systems, such as the linear spring-dashpot (LSD) contact model combined with CFD-DEM [102–104]. While this improves the efficiency of the traditional DEM model, its application to industrial-scale FB furnaces remains limited due to the high computational cost. As a result, CFD-DEM simulations of dense reactive gas-solid flow are mainly limited to two-dimensional or quasi-three-dimensional geometries with a small number of particles, and their applications in industrial-scale fluidized beds are still rare.

The MP-PIC model addresses the computational difficulties associated with calculating interparticle interaction in the Euler-Lagrange approach. It does so by mapping particle properties to an Euler grid and then mapping the computed stress tensors back to particle positions [105]. The MP-PIC method was first introduced by Andrews and O'Rourke [106] and is much more computationally efficient than the classical DEM method due to the use of more efficient collision models and the ability to use a larger time step [99]. Recently, a new general model has been developed for the numerical calculation of mass, momentum, and energy exchange between particles during collisions [107]. The model uses a Bhatnagar, Gross, and Krook (BGK) model [108] to approximate the rate at

which collisions bring about the local equilibrium of particle properties. The BGK model considers the effect of collisions as a simple relaxation term on the right-hand side of the Boltzmann equation. Studies have reported improved BGK-model collision damping time for particle velocity fluctuations [109] and the driving force toward isotropy particle velocity distribution [110].

To further reduce the computational cost, in addition to optimizing the collision model, the coarse grain method (CGM) can be employed to reduce the calculated number of particles. In the CGM, virtual particles (known as parcels) are used to represent real particles and are widely employed in the Euler-Lagrange framework [111]. Qi et al. [103] discussed the use of CGM in detail for simulating lab-scale fluidized beds. One characteristic of the CGM method is the high local solid load in certain computational cells, as fuel and sand particles are clustered into parcels. This may pose problems when simulating industrial FB furnaces with a wide range of particle size distribution (PSD). These FB furnaces typically have complex geometries that lead to the presence of small computational cells. Large particles contribute to large source terms in the gas-phase governing equations, causing convergence problems or numerical artifacts [112]. This is especially significant in the widely used and low-cost particle centroid method (PCM), in which the entire particle is assumed to be in the local cell where the particle centroid is located. At high particle load conditions, the solid volume fraction in the small local cell can exceed what the cell can physically accommodate, resulting in nonphysical and unstable solutions. This issue needs to be addressed.

Different methods have been proposed to address the issue of the small ratio of the mesh size to the particle size. These methods include the divided particle volume method (DPVM), the cube averaging method (CAM), the two-grid method (TGM), and the diffusion-based method (DBM) [112, 113]. Zhang et al. [114] investigated three of these methods, i.e., CAM, TGM, and DBM, and evaluated their impact on the distribution of source terms in a single-particle combustion case. In the DBM, the source terms of a Lagrangian particle are distributed into an Eulerian field using a statistical kernel function. The source terms are first calculated using the PCM model before being distributed, as the gas properties required by the particle sub-models are sampled from the local cell of the particles. Although the DBM is more robust compared to the other methods studied, its computational efficiency decreases rapidly with the increase in mesh resolution. In the TGM, a virtual coarse grid is created based on the fine grid to solve for the particle properties, and the source terms are then mapped to the fine grid [115]. The TGM, which treats the particles in a local grid, may cause significant errors in the simulations of particle-laden

flows due to the coarse mesh employed to resolve the fluid flow. In the CAM, a virtual cubic region is created as an interactive medium between the particle and the gas phase. Compared with the TGM and the DBM, the CAM is more efficient for dense multiphase flow simulations with unstructured meshes. However, it requires the construction of two independent meshes, which increases the complexity of the implementation and parallel computation.

Modeling the chemical reactions of biomass conversion during numerical simulations of FB furnaces is another significant challenge. Biomass pyrolysis produces many species, posing great challenges to simulating biomass gasification. Experiments have shown that several factors, such as particle size, operating temperature, gasifying agent, and residence time, govern the fuel composition [22, 116, 117]. In particular, the operating temperature plays a crucial role in the yield of gasification products. For instance, during the fast pyrolysis of woody biomass at $600 \sim 1000$ K, the CO yield increases drastically from around 5 wt% to 30 wt%, the CO_2 yield increases from around 1 wt% to 7 wt%, and the char yield decreases from around 30 wt% to 15 wt% [117]. To predict the gasification products, comprehensive models for the pyrolysis process, the char reactions with gasification agents, and the subsequent volatile reactions are required. In a recent review by Fatehi et al. [5], four classes of pyrolysis models were identified: (a) single-step model, (b) three parallel-step model with secondary tar cracking reactions, (c) FG-DVC model (which combines a functional group (FG) model for gas evolution and statistical depolymerization, vaporization, and crosslinking (DVC) model for tar formation), and (d) multicomponent pyrolysis model, e.g., developed at Politecnico di Milano [118, 119]. Multi-component pyrolysis models [118, 119] have been used to model single particle pyrolysis (e.g., [120, 121]), but they are seldom used in multiple-particle systems [122], as they require tremendously long computational time to carry out numerical simulations of a 3D fluidized bed furnace. Hence, simple one-step models have been employed in biomass combustion and gasification simulations in FB furnaces [58, 67, 86–88, 103, 123–126]. However, these one-step pyrolysis models may not accurately capture the general trend of gasification products at varying operating temperatures. It is therefore desirable to develop a more predictive one-step pyrolysis model for biomass. The main weakness of the current one-step pyrolysis model lurks in the use of constant stoichiometric coefficients of pyrolysis products, resulting in low sensitivity of gasification products to the operating temperature of the gasifier.

1.4 Knowledge gap in CFD modeling of biomass combustion and gasification in FB furnaces

Despite significant research efforts on modeling dense gas-solid flow in recent decades, there are still several bottlenecks that persist in using the Eulerian-Lagrangian approach to model dense particle-fluid systems.

First, particle overloading is one of the significant challenges in the CFD simulation of dense particle/gas flows. The Eulerian-Lagrangian method is highly grid-dependent, so it is essential to ensure that the cell size is sufficiently small compared to the macroscopic characteristic length of the system. The cell size, however, should be larger than the particle size to be consistent with the governing equations in the Eulerian-Lagrangian framework, e.g., the volume fraction of the gas in a physical space cell should be greater than zero. A cell-to-particle size ratio of $3 \sim 5$ is a compromise that balances solving the fluid flow with reasonable accuracy while adhering to the assumption of the Eulerian-Lagrangian approach. However, this approach significantly limits the application of the method in complex geometry and situations where higher solution accuracy is required for fluids. These limitations are particularly pronounced in large-scale dense particle-fluid systems due to complex spatial structure and the presence of quadrillion or more particles in the systems. The large-scale structure leads to the presence of small computational cells and a large number of particles in the cells, causing a problem referred to as the "local overloading" of particles. Numerical instability and nonphysical overloading can occur when large particles pass through small size cells.

Second, it is essential to develop a cost-effective chemical kinetic model that can accurately describe the thermochemical conversion of biomass during combustion and gasification. This model should consider various conversion processes, e.g., drying, pyrolysis, heterogeneous char reaction, and volatile gas homogeneous reactions. However, CFD simulations of large-scale FB furnaces are computationally demanding, making it desirable to develop global models that can accurately capture the thermochemical conversion processes while minimizing the computational cost.

Third, the four-way coupling of gas/solid dense particle reactive flow system is a complex process that lacks understanding, particularly in large-scale FB furnaces. In order to operate the furnace properly and optimize its performance, a deep understanding of the various processes involved in FB furnaces is required. These processes include the formation and evolution of gas bubbles in the dense particle granular flow, the gasification product yields under different

gasifier operation conditions, and the impact of primary, secondary, and tertiary air supply on the performance of FB furnaces.

1.5   Thesis objectives

The thesis is focused on biomass gasification/combustion in lab/industrial-scale fluidized beds. The project aims to predict the physical and chemical processes of biomass gasification/combustion in the dense particle-fluid systems at the individual particle level by developing a 3-dimensional reactive CFD model with efficient, robust, and high accuracy. A broad aim is to improve the understanding of the gas-solid interaction, the evolution of biomass conversion, and homogeneous and heterogeneous reactions in FB furnaces, providing theoretical support for the design and optimization of the FB. The main objectives of the thesis are described as follows:

- Development of a comprehensive Eulerian-Lagrangian method, considering gas-solid interactions, particle collision, heat and mass transfer, radiation, and homogeneous and heterogeneous chemical reactions. The model can be employed to investigate the physical and chemical mechanisms of dense gas-solid FB reactors.

- Development of a robust method addressing the challenging issue of local overloading, where the simulation will give a nonphysical and unstable solution due to large particle passing through small-size cells.

- Development of an empirical pyrolysis model improving the prediction of pyrolysis products at varying operating reactor temperatures. The model should predict the stoichiometric coefficients of the one-step global pyrolysis model.

- Application of the extended model to investigate the fluidization, heat transfer, combustion, and emission characteristics in the lab/industrial-scale fluidized bed furnaces. These complex processes can be visualized using the 3-D dimensional CFD model, contributing to the research and design of the FB furnaces.

1.6   Thesis content

Following the introduction, the modeling of reactive dense particle/gas flow is presented in Chapter 2. The governing equations employed in this thesis, i.e., gas phase, solid phase, gas-solid interaction, and the numerical approaches for the gas and solid phases, are presented in Chapter 3. The proposed distribution kernel method (DKM), the new pyrolysis model, the performance of the DKM in the lab/industrial-scale fluidized bed furnace, the effect of the new pyrolysis model on the product yield in the gasifier, and the simulation results of the fluidization, the heat transfer, and combustion processes are presented in Chapters 4-6. The main conclusions and future work are presented in Chapter 7. Part of the results have been published in papers [127–129].

Chapter 2

Modeling of reactive dense particle-gas flow

The continuum concept is crucial to model the gas-solid/fluid flow. A fluid is assumed as a continuous matter when its properties, such as density, pressure, velocity, and temperature, vary continuously from one point to another [130]. The assumption is significant to the differential forms of the conservation equations in which their derivations depend on taking limits as the length, area or volume approaches zero [131]. As shown in Figure 2.1, the gas consists of a larger number of individual molecules. The gas density can be defined as the mass per unit volume. The sampling volume ΔV contains molecules with a total mass of ΔM and the density of the gas is

$$\rho \cong \frac{\Delta M}{\Delta V}. \tag{2.1}$$

 A very small sampling space will contain very few molecules leading to a large density fluctuation. For an extreme example, i.e., the sampling space contains only one molecule, and another has two molecules, the fluctuations will be 100%. As the sampling volume increases, i.e., the sample volume ΔV is larger than the volume of the threshold ΔV_0, the space will contain a large number of molecules, and the fluctuation becomes negligible. According to the probability theory of Poisson distribution, the fluctuations will be less than 1% for a sampling volume containing 10^5 molecules. As the sampling volume increases further, the gas density will be changed by macroscopic variables, e.g., temperature, pressure, and shock waves. That is to say, if $\Delta V \gg \Delta V_0$, the continuum assumption in the modeling of the flow system is justified.

To predict the gas-solid two-phase flow, the continuum assumption is typically
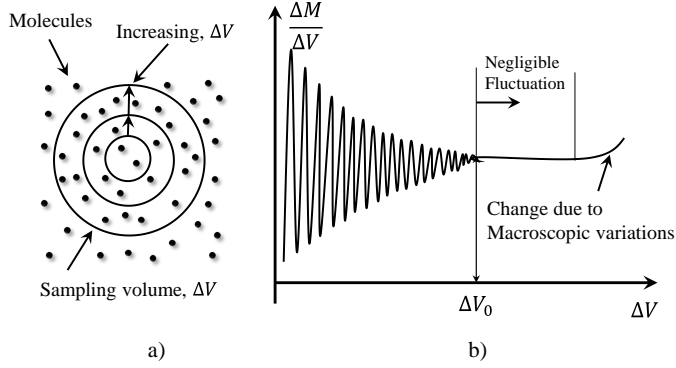
**Figure 2.1:** The variation of molecular mass per unit volume of mixture with the size of sampling volume [131]. Note: The figure is reproduced with permission from the publisher.

employed in the gas phase when the computational domain is much larger than ΔV_0. However, in the solid phase, the continuum assumption in several models is employed to reduce the computational cost, despite being nonphysical due to the significant fluctuations of solid phase properties in the continuous phase. An alternative, a more physically accurate assumption for the solid phase would be to track individual solid particles, but this greatly increases computational cost. A widely used alternative is the hybrid assumption, which combines the use of both continuum and discrete assumptions for different properties of the solid flow.

The interaction between gas and solid phases can be described using mass, momentum, and energy conservation. The coupling methods of the interaction between the gas and solid phases can be classified into one-way (gas $\rightarrow$ particle), two-way (gas $\leftrightarrow$ particle), and four-way couplings (gas $\leftrightarrow$ particle/wall $\leftrightarrow$ particle) [21, 132]. The very dilute gas-solid flow, i.e., solid volume fraction $\theta_s < 10^{-6}$, can be modeled using the one-way coupling in which the interaction from the particle to the gas phase can be negligible. In this very dilute flow, the particles have very small sizes and can be typically assumed to follow the instantaneous flow. As the θ_s increases, i.e., $10^{-6} \leq \theta_s \leq 10^{-3}$, the two-way coupling should be employed due to the strong interaction between gas and solid phase. If the $\theta_s > 10^{-3}$ [21, 131], the flow is considered as dense particle-fluid flow, and the interaction between gas and solid phase, the collisions between particle and particle/wall should be considered.

2.1 Model classification

The flow in fluidized beds is a dense gas-solid flow due to the large volume fraction of the solid phase in the boilers, i.e., $\theta_s \gg 10^{-3}$. The gas-solid flow involves a wide range of space and time scales. Several numerical models with continuous/discrete assumptions are proposed to describe the gas-solid flow at various scales. Myöhänen et al. [133] classified the numerical models based on time and space scales, see Fig. 2.2. The boundary of time and space scales may not be exact, but the classification provides ideas when modeling the multi-scale gas-solid flow. For the flow at the micro-scale level, the continuum assumption is non-physical and the gas and solid phases should be described as discrete phases. The flow at Meso/Macro-scale level can be assumed as a continuum/discrete matter in which the 2D/3D CFD models are widely employed. The 0D correlation model can be used to describe lumped-scale flows while it only provides limited information. The behaviors in fluidized beds typically involve scales
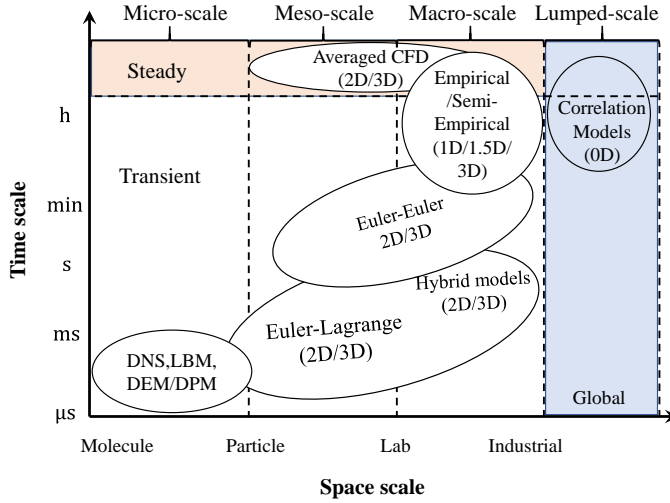
Figure 2.2: Scale-based classification of numerical approaches for fluidized beds flows [21, 133, 134]. Note: The figure is reproduced with permission from the author.

from particle scale to the industrial boiler scale and the time scale from seconds to hour scales. Alobaid et al. [21], Singh et al. [134] and Loha et al. [135] reviewed the recent progress in CFD simulations of fluidized beds. These models can be roughly divided into the following categories, as shown in Table 2.1: the mixture approach, the Euler-Euler approach, the Euler-Lagrange approach, and the Hybrid approach. In the framework of the mixture approach, the gas and solid phases are assumed as a single-phase mixture flow; in another word,

the gas and solid phases are not modeled individually. In the remaining approaches, the gas and solid phases are modeled individually and the interaction between the gas and solid phases is modeled using coupling methods. In those approaches, the solid phase is modeled as a continuum/discrete phase, while the gas phase is assumed as a continuum. In the Hybrid approach, the part of physical properties is modeled using the Euler method while the other parts of properties are modeled using the Lagrangian method.

Table 2.1: The physical assumptions in various CFD approaches for the fluidized bed.

Model	Gas phase	Solid phase
Mixture approach	continuum	continuum
Euler-Euler approach	continuum	continuum
Euler-Lagrange approach	continuum	discrete
Hybrid approach	continuum	discrete & continuum

2.2   Mixture model

In the framework of the mixture model (MM), the solid phase is assumed to be distributed uniformly into the gas phase and has a small velocity and temperature difference from the gas phase. The conservation equations of mass, momentum, and energy for the single-phase flow can be employed in MM. The continuity equation for the mixture phase is

$$\frac{\partial(\rho_e)}{\partial t} + \nabla \cdot (\rho_e \mathbf{u}_e) = S_{m,e},\qquad(2.2)$$

where ρ_e, $\mathbf{u}_e$ denote respectively the effective density and velocity of the mixture phase. $S_{m,e}$ represents the injection or the leakage of the mixture.

The momentum equations are

$$\frac{\partial(\rho_e \mathbf{u}_e)}{\partial t} + \nabla \cdot (\rho_e \mathbf{u}_e \mathbf{u}_e) = \nabla \cdot (\tau_e) - \nabla p_e + \rho_e \mathbf{g} + S_{\mathbf{u},e},\qquad(2.3)$$

where τ_e, p_e, and $\mathbf{g}$ denote respectively the sum of viscous stress and Reynolds stress, pressure, and gravitational acceleration of mixture phase. $S_{\mathbf{u},e}$ is the moment source term.

The energy equation is

$$\frac{\partial(\rho_e h_e)}{\partial t} + \nabla \cdot (\rho_e \mathbf{u}_e h_e) = \nabla \cdot (\Gamma_e \nabla h_e) + S_{h,e},\qquad(2.4)$$

where h_e, Γ_e, and $S_{h,e}$ denote respectively the specific energy, the sum of molecular and turbulent heat diffusion coefficients, and heat source terms.

The species equation is

$$\frac{\partial(\rho_e Y_{e,k})}{\partial t} + \nabla \cdot (\rho_e \mathbf{u}_e Y_{e,k}) = \nabla \cdot (D_e \nabla Y_{e,k}) + S_{Y_{c,k}}, \tag{2.5}$$

where $Y_{e,k}$, D_e, and $S_{Y_{c,k}}$ denote respectively concentration of species k in the mixture phase, diffusion coefficients taking account both the viscous and turbulent contribution and species source due to chemical reactions.

In these governing equations, the density of the mixture phase can be expressed as

$$\rho_e = \alpha_g \rho_g + \theta_s \rho_s, \quad \alpha_g + \theta_s = 1, \tag{2.6}$$

where α_g, ρ_g, and ρ_s denote respectively the gas volume fraction, gas density, and solid density.

The mixture model has the advantage of high computing stability and low computational time. However, the MM shows the numerical instabilities when it is extended into the dense gas-solid systems [21]. The numerical results have a low accuracy due to the large density difference in gas and solid phases.

2.3   Euler-Euler approach

In the Euler-Euler approach, both solid and gas phases are assumed as the continuum phase, in which the gas and solid phases are modeled with the balance equation of the Euler governing equations. The CFD model of the Euler-Euler approach widely employed is the two-fluid model (TFM). The governing equations of TFM are derived based on the kinetic theory of granular flows (KTGF), which uses a virtual point value to model all physical gas [84]. The KTGF is derived from the kinetic theory of dense gases (KTDG) [136]. The continuity equations of the TFM [98, 137] for the gas and solid phases are,

$$\frac{\partial(\alpha_g \rho_g)}{\partial t} + \nabla \cdot (\alpha_g \rho_g \mathbf{u}_g) = S_{m,g}, \tag{2.7}$$

and

$$\frac{\partial(\alpha_s \rho_s)}{\partial t} + \nabla \cdot (\alpha_s \rho_s \mathbf{u}_s) = S_{m,s}, \tag{2.8}$$

where $\mathbf{u}_g$ and $\mathbf{u}_s$ denote respectively the velocity of the gas and solid phases. $S_{m,g}$ represents the mass source terms transferring from the solid phase to the

gas phase. While $S_{m,s}$ represents the mass source terms transferring from the gas phase to the solid phase.

The momentum equations for the gas and solid phases are

$$\frac{\partial(\alpha_g\rho_g\mathbf{u}_g)}{\partial t} + \nabla\cdot(\alpha_g\rho_g\mathbf{u}_g\mathbf{u}_g) = \nabla\cdot(\tau_g) - \alpha_g\nabla p + \alpha_g\rho_g\mathbf{g} + \mathbf{S}_{u,g}, \qquad (2.9)$$

and

$$\frac{\partial(\theta_s\rho_s\mathbf{u}_s)}{\partial t} + \nabla\cdot(\theta_s\rho_s\mathbf{u}_s\mathbf{u}_s) = \nabla\cdot(\tau_s) - \theta_s\nabla p + \theta_s\rho_s\mathbf{g} + \mathbf{S}_{u,s}, \qquad (2.10)$$

where τ_g, τ_s, and p denote respectively the stress of gas and solid phases and pressure. $\mathbf{S}_{u,g}$ is the momentum source terms transferring from the solid phase to the gas phase, and $\mathbf{S}_{u,s}$ is the momentum source terms transferring from gas phase to solid phase.

The energy equations for the gas and solid phases are

$$\frac{\partial(\alpha_g\rho_g h_g)}{\partial t} + \nabla\cdot(\alpha_g\rho_g\mathbf{u}_g h_g) = \alpha_g\frac{\partial p}{\partial t} + \nabla\cdot(\alpha_g\Gamma_g\nabla h_g) + S_{h,g}, \qquad (2.11)$$

and

$$\frac{\partial(\theta_s\rho_s h_s)}{\partial t} + \nabla\cdot(\theta_s\rho_s\mathbf{u}_s h_s) = \theta_s\frac{\partial p}{\partial t} + \nabla\cdot(\theta_s\Gamma_s\nabla h_s) + S_{h,s}, \qquad (2.12)$$

where h_g, h_s, Γ_g and Γ_s denote respectively gas-specific energy and solid-specific energy, and the heat diffusion coefficients of gas and solid phases. $\mathbf{S}_{h,g}$ and $\mathbf{S}_{h,s}$ are the energy source terms of gas and solid phases due to chemical reactions, the radiation, and heat and mass transfer from the other phase.

The species equations for the gas and solid phases are

$$\frac{\partial(\alpha_g\rho_g Y_{g,k})}{\partial t} + \nabla\cdot(\alpha_g\rho_g\mathbf{u}_g Y_{g,k}) = \nabla\cdot(\alpha_g D_g\nabla Y_{g,k}) + S_{Y_{g,k}}, \qquad (2.13)$$

and

$$\frac{\partial(\theta_s\rho_s Y_{s,k})}{\partial t} + \nabla\cdot(\theta_s\rho_s\mathbf{u}_s Y_{s,k}) = \nabla\cdot(\theta_s D_s\nabla Y_{s,k}) + S_{Y_{s,k}}, \qquad (2.14)$$

where $Y_{g,k}$, $Y_{s,k}$, D_g, and D_s denote respectively concentration of species k in the gas and solid phases, gas diffusion coefficients and solid diffusion coefficients. $S_{Y_{g,k}}$ and $S_{Y_{s,k}}$ are the species source terms of gas and solid phases due to chemical reactions.

The stress tensor τ_g and τ_s can be expressed as

$$\tau_g = \mu_g(\nabla \mathbf{u}_g + \nabla \mathbf{u}_g^{\mathrm{T}}) - \frac{2}{3}\mu_g(\nabla \cdot \mathbf{u}_g)\mathbf{I}, \tag{2.15}$$

and

$$\tau_s = \mu_s(\nabla \mathbf{u}_s + \nabla \mathbf{u}_s^{\mathrm{T}}) - \frac{2}{3}\mu_s(\nabla \cdot \mathbf{u}_s)\mathbf{I}, \tag{2.16}$$

where μ_g, μ_s, and $\mathbf{I}$ denote respectively the gas phase dynamic viscosity, the solid phase dynamic viscosity, and the unit matrix.

In governing equations of the solid phase, the concepts of granular viscosity, pressure, and stress are introduced. The mathematical form of governing equations for the solid phase is similar to those of the gas phase; however, the closed method of those equations is very different from those of gas phase equations. Those properties of the solid phase are a function of the granular temperature. An additional balance equation is employed to model the granular temperature which is based on the particle velocity fluctuation and variation in time and position. The granular temperature Θ_s is one-third of the mean square particle's velocities as a measure of fluctuations and can be given by

$$\Theta_s = \frac{1}{3}\left\langle \mathbf{C}^2 \right\rangle, \tag{2.17}$$

where $\mathbf{C}$ is the particle fluctuating velocity and $\langle\rangle$ is the averaging operator.

The variation of Θ_s in time and space scales is modeled by a separate conservation equation given by

$$\frac{2}{3}\left(\frac{\partial}{\partial t}(\theta_s\rho_s\Theta_s) + \nabla \cdot (\theta_s\rho_s\Theta_s\mathbf{u}_s)\right) = \underbrace{(-p_s\mathbf{I} + \tau_s):\nabla\mathbf{u}_s}_{\text{Term1}} +$$
$$\underbrace{\nabla \cdot (\Gamma_{\Theta_s}\nabla\Theta_s)}_{\text{Term2}} - \underbrace{D_{\Theta_s}}_{\text{Term3}} + \underbrace{\Phi_{Is}}_{\text{Term4}}, \tag{2.18}$$

where Γ_{Θ_s} denotes the diffusion coefficient of granular energy. D_{Θ_s} and Φ_{Is} are respectively the energy dissipation rate of the solid phase and energy exchange between gas and solid phases.

In the granular temperature equation, Term1 is the energy generated by the solid stress tensor, Term2 denotes the diffusion of energy, Term3 represents the rate of energy dissipation within the solid phase due to inelastic collisions and Term4 is the energy exchange between the current solid phase with the fluid phase or other solid phases. The diffusion coefficient of granular energy is derived by Gidaspow et al. [84] and Syamla, Rogers, and O'Brien [138]. The

rate of energy dissipation and the energy exchange are derived by Lun et al [139]. To model the particle phase stresses and the solid pressure, the solid phase is assumed as homogeneous. The assumption is nonphysical for the dense particle-fluid systems due to the unstable and discrete particle flow in the fluidized bed. Zhang and van der Heyden [140] introduced a filter function to overcome the issue as well as the overestimation of drag force. The mesh-dependent solution of the two-fluid flow is a challenge as well in modeling the gas-solid flow. To improve the mesh dependence, Andrews et al. [141] and van der Hoef et al. [142] suggested that the grid size is of the order of ten particle diameters. However, it will result in low accuracy due to coarse meshes employed to resolve the fluid flow. Moreover, in the dense particle-fluid system, such as the fluidized bed, fuel, and inert particles exist in the systems. The governing equations of both solid phases, as well as the interaction among solid phases, have to be modeled.

2.4   Euler-Lagrange approach

Compared to the Euler-Euler approach, the Euler-Lagrange approach is an efficient method to model granular flow with a wide range of particle size distribution (PSD). Two main methods, the discrete element model (DEM)/ discrete particle model (DPM) and multi-phase particle-in-cell (MP-PIC), are widely employed in the Euler-Lagrange approach. In the DEM/DPM, the gas phase is assumed as a continuum, and the solid phase is treated as a discrete phase. The continuity equation of the gas phase is

$$\frac{\partial(\alpha_g \rho_g)}{\partial t} + \nabla \cdot (\alpha_g \rho_g \mathbf{u}_g) = S_{m,g}. \tag{2.19}$$

The momentum equations for the gas phase have two types of models,

$$\frac{\partial(\alpha_g \rho_g \mathbf{u}_g)}{\partial t} + \nabla \cdot (\alpha_g \rho_g \mathbf{u}_g \mathbf{u}_g) = \begin{cases} \underbrace{\nabla \cdot (\alpha \tau_g) - \alpha_g \nabla p + \alpha_g \rho_g \mathbf{g} + \mathbf{S}_{u,g}}_{\text{Model A}} \\ \underbrace{\nabla \cdot (\alpha \tau_g) - \nabla p + \alpha_g \rho_g \mathbf{g} + \mathbf{S}_{u,g}}_{\text{Model B}} \end{cases} . \tag{2.20}$$

The momentum equations were derived in two formats by Gidaspow [84]. The difference between Model A and Model B is the treatment of the pressure source terms. In Model A, the pressure is shared by both gas and solid phases while the pressure is only attributed to the gas phase in Model B. Zhou et al. [143] investigated the effect of Model A and Model B on the performance in conveying and fluidization processes. It demonstrated that the difference between the

models is negligible due to the very small contribution of pressure. In the models of dense fluid-particle systems, Model A is widely employed.

The energy equation of the gas phase is

$$\frac{\partial(\alpha_g \rho_g h_g)}{\partial t} + \nabla \cdot (\alpha_g \rho_g \mathbf{u}_g h_g) = \alpha_g \frac{\partial p}{\partial t} + \nabla \cdot (\alpha_g \Gamma_g \nabla h_g) + S_{h,g}. \tag{2.21}$$

The species equation of the gas phase is

$$\frac{\partial(\alpha_g \rho_g Y_{g,k})}{\partial t} + \nabla \cdot (\alpha_g \rho_g \mathbf{u}_g Y_{g,k}) = \nabla \cdot (\alpha_g D_g \nabla Y_{g,k}) + S_{Y_{g,k}}. \tag{2.22}$$

In general, the governing equations of the gas phase in the Euler-Lagrange framework are very similar to those of the Euler-Euler framework. However, the governing equations of the solid phase are modeled at the individual particle level using ordinary differential equations. The mass conservation equation of the ith fuel particle is

$$\frac{dm_i}{dt} = \dot{m}_{vapor,i} + \dot{m}_{devol,i} + \dot{m}_{char,i}, \tag{2.23}$$

where m_i, $\dot{m}_{vapor,i}$, $\dot{m}_{devol,i}$ and $\dot{m}_{char,i}$ denote the particle mass, the evaporation rate, the devolatilization rate, and the char conversion rate, respectively. These conversion processes involve the evaporation of moisture, the volatile release during the pyrolysis, and the chemical reactions occurring at the surface of the particle.

The translational and rotational motion equations of the ith particle are

$$m_i \frac{d\mathbf{u}_i}{dt} = \underbrace{\mathbf{f}_{g,i}}_{Interaction} + \underbrace{\sum_{j=1}^{N}(\mathbf{f}_{c,ij} + \mathbf{f}_{d,ij})}_{Collison} + \underbrace{m_i \mathbf{g}}_{Gravity}, \tag{2.24}$$

and

$$I_i \frac{d\omega_i}{dt} = \sum_{j=1}^{N}(\mathbf{M}_{t,ij} + \mathbf{M}_{r,ij}), \tag{2.25}$$

where $\mathbf{u}_i$ denotes the velocity of ith particle. $\mathbf{f}_{g,i}$, $\mathbf{f}_{c,ij}$ and $\mathbf{f}_{d,ij}$ denote respectively the particle-fluid interaction, the elastic and viscous damping forces between two adjacent particles. N is the number of particles interacting with the ith particle. I_i, $\mathbf{M}_{t,ij}$, and $\mathbf{M}_{r,ij}$ are the moment of inertia, the torque generated by the tangential force and the rolling fraction torque, respectively. The particle-fluid interaction force $\mathbf{f}_{g,i}$ is the sum of all types of particle-fluid interaction forces acting on individual particles by fluid. The conservation equations of $\mathbf{f}_{g,i}$ can be written as

$$\mathbf{f}_{g,i} = \mathbf{f}_{d,i} + \mathbf{f}_{\nabla p,i} + \mathbf{f}_{\nabla \cdot \tau,i} + \mathbf{f}_{vm,i} + \mathbf{f}_{B,i} + \mathbf{f}_{Saff,i} + \mathbf{f}_{Mag,i}, \tag{2.26}$$

where $\mathbf{f}_{d,i}$ and $\mathbf{f}_{\nabla p,i}$ denote the drag force and pressure gradient force, respectively. $\mathbf{f}_{\nabla\cdot\tau,i}$ is the viscous force due to the fluid shear stress, $\mathbf{f}_{vm,i}$ is the virtual mass force, and $\mathbf{f}_{B,i}$ is the Basset force. $\mathbf{f}_{Saff,i}$ and $\mathbf{f}_{Mag,i}$ are the Staffman force and Magnus force respectively and both of them belong to the lift forces [131]. In addition to these forces, there may be a so-called "rocket force" introduced in the non-isotropic release of moisture vapor and volatile during pyrolysis [144, 145]. This is force is neglected here for simplicity.

The energy conservation equation of the ith particle is

$$m_i C_{p,i} \frac{dT_i}{dt} = q_{c,i} + q_{r,i} - q_{vapor,i} + q_{devol,i} + q_{char,ij}, \qquad (2.27)$$

where T_i, $C_{p,i}$, $q_{c,i}$ and $q_{r,i}$ denote respectively the temperature, the heat capacity, convective and radiative heat transfer of ith particle. $q_{vapor,i}$, $q_{devol,i}$ and $q_{char,ij}$ represent the heat transfer of latent, pyrolysis, and char reactions.

2.4.1 Drag model

The coupling of fluid and solid phases for momentum conservation are mainly achieved through solid-fluid interaction in the fluidized bed, particularly drag force. The drag force model widely used for the i-th individual particle is given by [58, 84, 146]

$$\mathbf{f}_{d,i} = V_\Omega \beta (\mathbf{u}_g - \mathbf{u}_i), \qquad (2.28)$$

where V_Ω is the volume of the computational cell, and β is the drag force parameter.

Many empirical correlations of drag coefficients have been proposed, e.g., the Ergun drag model [147], Wen & Yu drag model [148], and Di Felice [149]. More correlations of drag coefficients were reviewed by Alobaid et al. [21] and Pan et al. [150]. This thesis presents the widely used empirical correlations of drag coefficients.

Ergun drag: In Eq. (2.28), the β of Ergun equation [84, 147] is modeled as

$$\beta = \frac{3}{4} C_d \frac{(1 - \alpha_g)\rho_g}{d_i} |\mathbf{u}_g - \mathbf{u}_i| \alpha_g^{-1.65}, \qquad (2.29)$$

where d_i is the particle diameter. C_d is the drag coefficient and can be modeled as [84]

$$C_d = \begin{cases} \frac{24}{Re_i}(1 + 0.15 Re_i^{0.687}) & Re_i < 1000 \\ 0.44 & Re_i \geq 1000 \end{cases}, \qquad (2.30)$$

and the particle Reynolds number Re_i is defined as

$$Re_i = \alpha_g \rho_g d_i |\mathbf{u}_g - \mathbf{u}_i| / \mu_g. \tag{2.31}$$

Wen & Yu drag: The β of Wen & Yu drag model [148] is,

$$\beta = \begin{cases} 150 \frac{(1-\alpha_g)^2 \mu_g}{\alpha_g^2 d_i^2} + 1.75 \frac{(1-\alpha_g)\rho_g}{\alpha_g d_i} |\mathbf{u}_g - \mathbf{u}_i| & \alpha_g < 0.8 \\ \frac{3}{4} C_d \frac{(1-\alpha_g)\rho_g}{d_i} |\mathbf{u}_g - \mathbf{u}_i| \alpha_g^{-2.65} & \alpha_g \geq 0.8 \end{cases}, \tag{2.32}$$

where C_d is modeled as [84]

$$C_d = \begin{cases} \frac{24}{Re_i}(1 + 0.15 Re_i^{0.687}) & Re_i < 1000 \\ 0.44 & Re_i \geq 1000 \end{cases}, \tag{2.33}$$

Di Felice drag: The β of Di Felice [149] is,

$$\beta = \frac{3}{4} C_d \frac{\rho_g (1-\alpha_g)|(\mathbf{u}_i - \mathbf{u}_g)| \alpha_g^{\chi}}{d_i}, \tag{2.34}$$

where C_d is modeled as [84]

$$C_d = (0.63 + \frac{4.8}{\sqrt{Re_i}})^2, \tag{2.35}$$

and the coefficient χ is modeled as

$$\chi = 3.7 - 0.65 exp(-\frac{(1.5 - log_{10}(Re_i))^2}{2}). \tag{2.36}$$

2.4.2 Coarse grain method

A fluidized bed furnace usually contains billions or quadrillions of particles resulting in very high computational costs. Tracking every individual particle goes beyond the computing feasibility of the practical high-performance cluster. To reduce the computational cost, a so-called "parcel" method, i.e., coarse grain method (CGM), in which a virtual parcel represents the number of real particles, is widely employed in the Euler-Lagrange approach. As shown in Fig. 2.3, the particles in the parcel have the same properties, e.g., velocity, angular velocity, and temperature. The number of particles N_p in a parcel can be expressed by

$$N_p = l^3 = \frac{V_p}{V_i} = (\frac{d_p}{d_i})^{\frac{1}{3}}, \tag{2.37}$$

Note: $S_{\emptyset} = \{S_m,\, \mathbf{S_u},\, S_q,\, S_{Y_k}\}$
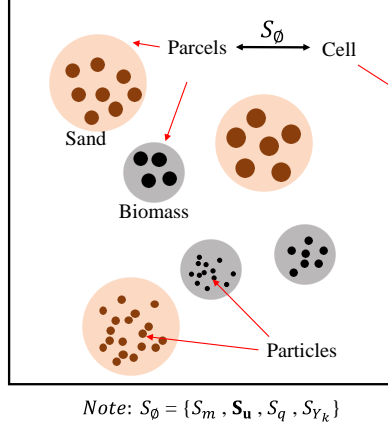
Figure 2.3: Schematic diagram of the parcel and real particles in a cell.

where l, V_i, V_p, and d_p represent the coarse grain ratio, particle volume, parcel equivalent volume, and parcel equivalent diameter, respectively. In the CGM, the conservation equations of the ith parcel can be expressed as

$$\frac{dm_p}{dt} = N_p \frac{dm_i}{dt}, \quad m_p \frac{d\mathbf{u}_p}{dt} = N_p m_i \frac{d\mathbf{u}_i}{dt}, \quad m_p C_{p,p} \frac{dT_p}{dt} = N_p m_i C_{p,i} \frac{dT_i}{dt} \quad (2.38)$$

where the m_p, $\mathbf{u}_p$, and T_p represent the equivalent parcel mass, the velocity of the parcel, and the parcel temperature respectively.

The coarse grain method reduces the computational cost by tracking fewer particles. The number of particles with the same diameter and density is grouped into a parcel. Two main approaches, i.e., the same size parcel (SSP) method and the same statistic weight (SSW) method, are employed in the CGM [151]. In the SSP method, all parcels in the domain have the same number of real particles but various masses. While in the SSW method, all parcels in the domain have the same mass but various numbers of particles. The appropriate method employed in CFD models depends on the various investigations. There is no difference between the SSP and SSW methods when a constant particle diameter is employed. Lu et al. [151] showed that the SSW method has the advantage of studying fixed bed systems while the SSP method is suitable for fluidized bed systems.

Despite the advantage of computational cost, the coarse grain method might give rise to an inaccurate distribution of particles in the fluidized bed. The collision probability in the simulation using the coarse grain method is lower than in the original system with a real number of particles. A large number of particles are grouped into a parcel leading to an overloading issue that gives a

nonphysical and unstable solution. Albeit those challenges, the Euler-Lagrange coupling coarse grain method is a good choice to balance the computational cost and simulation accuracy in CFD simulations.

2.4.3 Collision model

In the DPM, the collision of particle-particle and particle-wall is critical to computational cost and accuracy. Two main collision models are widely employed in DPM, i.e., the soft-sphere and the hard-sphere models.

Soft-sphere model: In the framework of the soft sphere model, the contact force $\mathbf{f}_{c,ij}$ in Eq. (2.24) is divided into normal force $\mathbf{f}_{ij}^n$ and tangential force $\mathbf{f}_{ij}^t$ [100]. The $\mathbf{f}_{ij}^n$ can be modeled by

$$\mathbf{f}_{ij}^n = -k\mathbf{d}_n - \eta\mathbf{u}_{n,ij}, \tag{2.39}$$

and the $\mathbf{f}_{ij}^t$ can be modeled by

$$\mathbf{f}_{ij}^t = \begin{cases} -k\mathbf{d}_t - \eta\mathbf{u}_{t,ij} & |\mathbf{f}_{ij}^t| \leq h_f|\mathbf{f}_{ij}^n| \\ -h_f|\mathbf{f}_{ij}^n|\mathbf{t}_{ij} & |\mathbf{f}_{ij}^t| > H_f|\mathbf{f}_{ij}^n| \end{cases}, \tag{2.40}$$

where k is the stiffness of the spring, η is the coefficient of viscous dissipation, and h_f is the friction coefficient. $\mathbf{d}_n$ and $\mathbf{d}_t$ denote respectively the particle displacement in the normal and tangential directions. $\mathbf{u}_{n,ij}$ and $\mathbf{u}_{t,ij}$ are the components of the relative velocity in the normal and tangential directions and can be modeled by

$$\mathbf{u}_{n,ij} = (\mathbf{u}_{r,ij} \cdot \mathbf{n}_{ij})\mathbf{n}_{ij}, \tag{2.41}$$

and

$$\mathbf{u}_{t,ij} = \mathbf{u}_{r,ij} - \mathbf{u}_{n,ij}, \tag{2.42}$$

where $\mathbf{u}_{r,ij}$ is the relative velocity between ith particle and jth particle. $\mathbf{n}_{ij}$ is the normal unit vector and given by

$$\mathbf{n}_{ij} = \frac{\mathbf{x}_i - \mathbf{x}_j}{|\mathbf{x}_i - \mathbf{x}_j|}. \tag{2.43}$$

$\mathbf{t}_{ij}$ is the unit vector defined by

$$\mathbf{t} = \frac{\mathbf{u}_{t,ij}}{|\mathbf{u}_{t,ij}|}. \tag{2.44}$$

Hard-sphere model: The hard-sphere model was developed by Hoomans et al. [152–155]. The interaction between two particles is assumed as impulsive. The binary collisions can be described by Newton's second and third laws,

$$m_i(\mathbf{u}_i - \mathbf{u}_{i,0}) = -m_j(\mathbf{u}_j - \mathbf{u}_{j,0}) = \mathbf{J}, \tag{2.45}$$

and

$$\frac{I_i}{r_i}(\omega_i - \omega_{i,0}) = \frac{I_j}{r_j}(\omega_j - \omega_{j,0}) = -\mathbf{n}_{ij} \times \mathbf{J}, \qquad (2.46)$$

where r is the radius of the particle. The subscripts i and j denote the ith and jth particle. The subscript 0 denotes the particle properties prior-to-collision. $\mathbf{J}$ represents the impulse vector. The relative velocity $\mathbf{u}_{r,ij}$ at the contact point c can be defined by

$$\mathbf{u}_{r,ij} = \mathbf{u}_{i,c} - \mathbf{u}_{j,c} = \mathbf{u}_i - \mathbf{u}_j - (r_i\omega_i + r_j\omega_j) \times \mathbf{n}_{ij}. \qquad (2.47)$$

Eqs. (2.45) and (2.46) can be rearranged to obtain

$$\mathbf{u}_{r,ij} - \mathbf{u}_{r0,ij} = \frac{7\mathbf{J} - 5\mathbf{n}_{ij}(\mathbf{J} \cdot \mathbf{n}_{ij})}{2m_{ij}}, \qquad (2.48)$$

where m_{ij} denotes the reduced mass given by

$$m_{ij} = (\frac{1}{m_i} + \frac{1}{m_j})^{-1}. \qquad (2.49)$$

To describe the impulse vector $\mathbf{J}$, three parameters are defined, i.e., the coefficient of normal restitution e_n, the coefficient of the dynamic fraction μ_f, and the coefficient of tangential restitution β_0. These three parameters are given by

$$e_n = -\frac{\mathbf{u}_{ij} \cdot \mathbf{n}_{ij}}{\mathbf{n}_{r0,ij} \cdot \mathbf{n}_{ij}}, \qquad (2.50)$$

$$\mu_f = -\frac{|\mathbf{n}_{ij} \times \mathbf{J}|}{\mathbf{n}_{ij} \cdot \mathbf{J}}, \qquad (2.51)$$

and

$$\beta_0 = -\frac{\mathbf{n}_{ij} \times \mathbf{u}_{ij}}{\mathbf{n}_{ij} \times \mathbf{u}_{r0,ij}}. \qquad (2.52)$$

Based on Eqs. (2.48) and (2.50), the normal component of $\mathbf{J}$ can be given by

$$\mathbf{J}_n = -(1 + e_n)m_{ij}(\mathbf{u}_{r0,ij} \cdot \mathbf{n}_{ij}). \qquad (2.53)$$

$\mathbf{J}_t$ can be given by

$$\mathbf{J}_t = \begin{cases} -\frac{2}{7}(1 + \beta_0) \times m_{ij}(\mathbf{u}_{ij} \cdot \mathbf{t}_{ij}) & \text{if Case 1} \\ -\mu_f\mathbf{J}_n & \text{if Case 2} \end{cases}, \qquad (2.54)$$

where $\mathbf{t}_{ij}$ denotes the tangential unit vector and can be given by

$$\mathbf{t}_{ij} = \frac{\mathbf{u}_{r0,ij} - \mathbf{n}_{ij} \cdot \mathbf{u}_{r0,ij}}{|\mathbf{u}_{r0,ij} - \mathbf{n}_{ij} \cdot \mathbf{u}_{r0,ij}|}. \qquad (2.55)$$

The criteria in Eq. (2.54) are

$$\text{Case} = \begin{cases} \text{Case 1} & \mu_f\mathbf{J}_n \geq \frac{2}{7}(1 + \beta_0)m_{ij}(\mathbf{u}_{ij} \cdot \mathbf{t}_{ij}) \\ \text{Case 2} & \mu_f\mathbf{J}_n < \frac{2}{7}(1 + \beta_0)m_{ij}(\mathbf{u}_{ij} \cdot \mathbf{t}_{ij}) \end{cases}. \qquad (2.56)$$

2.5 Hybrid model

The particle-in-cell (PIC) methods have been employed in simulations of multiphase flows since 1960 [156]. O'Rourke et al. [106, 109, 110] extended the PIC method and subsequently proposed the MP-PIC method. The MP-PIC method describes the particle phase simultaneously as a continuum and a discrete phase. Some particle properties are calculated on the grids while the remaining particle properties are calculated at discrete particle locations. The particle-particle collision, i.e., inter-particle stresses/particle-particle stresses, is modeled similarly as in the TFM as a gradient on the Eulerian grid. The governing equations of the gas phase in the MP-PIC method are similar to those in the DPM. The continuity equation of the gas phase is

$$\frac{\partial(\alpha_g \rho_g)}{\partial t} + \nabla \cdot (\alpha_g \rho_g \mathbf{u}_g) = S_{m,g}. \tag{2.57}$$

The momentum equations for the gas phase are

$$\frac{\partial(\alpha_g \rho_g \mathbf{u}_g)}{\partial t} + \nabla \cdot (\alpha_g \rho_g \mathbf{u}_g \mathbf{u}_g) = \nabla \cdot (\alpha \tau_g) - \alpha_g \nabla p + \alpha_g \rho_g \mathbf{g} + \mathbf{S}_{u,g}. \tag{2.58}$$

The energy equation of the gas phase is

$$\frac{\partial(\alpha_g \rho_g h_g)}{\partial t} + \nabla \cdot (\alpha_g \rho_g \mathbf{u}_g h_g) = \alpha_g \frac{\partial p}{\partial t} + \nabla \cdot (\alpha_g \Gamma_g \nabla h_g) + S_{h,g}. \tag{2.59}$$

The species equation of the gas phase is

$$\frac{\partial(\alpha_g \rho_g Y_{g,k})}{\partial t} + \nabla \cdot (\alpha_g \rho_g \mathbf{u}_g Y_{g,k}) = \nabla \cdot (\alpha_g D_g \nabla Y_{g,k}) + S_{Y_{g,k}}. \tag{2.60}$$

2.5.1 MP-PIC approach

The transport equations for the solid phase are based on particle probability distribution function $f(m_s, \mathbf{u}_s, \mathbf{x}_s, t)$, which is a function of particle spatial $\mathbf{x}_s$, particle velocity $\mathbf{u}_s$, particle mass m_s and time t. The transport equation of f is

$$\frac{\partial f}{\partial t} + \nabla \cdot (f \mathbf{u}_s) + \nabla_u \cdot (f \mathbf{A}_s) = 0, \tag{2.61}$$

where $\mathbf{A}_s$ is the acceleration of the solid phase. ∇ and ∇_u are divergence operators with respect to physical space $\mathbf{x}_s$ and velocity $\mathbf{u}_s$. Note that the particle velocity $\mathbf{u}_s$ is in the Eulerian frame, which is different from the velocity of an individual particle in the Lagrangian frame (i.e., $\mathbf{u}_i$ in Eq. 2.24).

The particle collision can be introduced into the transport equation using Boltzmann-Bhatnagar, Gross, and Krook (BGK) approximation [108]. O'Rourke and Snider [107, 109, 110] improved the BGK collision model based on the damping time for particle velocity fluctuations and the additional effect that drives the particle velocity distribution toward isotropy. The transport equation considering the particle collision is

$$\frac{\partial f}{\partial t} + \nabla \cdot (f\mathbf{u}_s) + \nabla_u \cdot (f\mathbf{A}_s) = \frac{f_G - f}{\tau_G} + \frac{f_D - f}{\tau_D}, \tag{2.62}$$

where f_G is the equilibrium-isotropic particle distribution function. f_D is the collision-damping particle distribution function. τ_G and τ_D are relaxation times.

The momentum conservation equations of the ith particle in the MP-PIC framework are

$$m_i \frac{d\mathbf{u}_i}{dt} = \mathbf{f}_{g,i} + \mathbf{f}_{\mathbf{g},i} + \mathbf{f}_{\tau,i}, \tag{2.63}$$

where $\mathbf{f}_{\tau,i}$ is the particle stress. The particle-fluid interaction term $\mathbf{f}_{g,i}$ mainly contains the drag force and pressure gradient force. The momentum equations of ith particle can be expressed as

$$\frac{d\mathbf{u}_i}{dt} = \underbrace{\frac{\beta}{\rho_i(1-\alpha_g)}(\mathbf{u}_g - \mathbf{u}_i) - \frac{1}{\rho_i}\nabla p_g}_{\mathbf{f}_{g,i}} - \underbrace{\mathbf{g}\left(1 - \frac{\rho_g}{\rho_i}\right)}_{\mathbf{f}_{\mathbf{g},i}} + \underbrace{\frac{1}{\rho_s\theta_s}\nabla\tau}_{\mathbf{f}_{\tau,i}}. \tag{2.64}$$

The volume fraction of the solid phase θ_s in a cell is modeled as

$$\theta_s = \iint f\frac{m_s}{\rho_s}dm_s du_s, \quad \alpha_g + \theta_s = 1. \tag{2.65}$$

2.5.2 Interparticle stress

The interparticle stress in Eq. (2.64) is difficult to resolve for each particle in dense gas-solid flows. The particle normal stress in MP-PIC is modeled using a continuum calculation of the particle pressure and the subsequent stress model is applied to discrete particles [105]. The collision model employs the isotropic interparticle stress where the off-diagonal elements of the stress tensor are neglected. The collision model is robust and efficient and is suited for three-dimensional simulations. A widely used interparticle stress model is derived by Harris and Crighton [157],

$$\tau = \frac{P_s\theta_s^{\beta_\tau}}{\max[(\theta_{cp} - \theta_s), \varepsilon_\tau(1 - \theta_s)]}, \tag{2.66}$$

where constant P_s has a unit of pressure. θ_{cp} is the solid phase volume fraction at close packing. β_τ and ε_τ are model constants. Auzerais et al. [158] recommend $2 \leq \beta_\tau \leq 5$ and Snider [105] recommends ε_τ is a small number on the order of 10^{-7}.

The Harris-Crighton model only considers the concentration of the particles while the size and velocity of particles are neglected. Moreover, the model is a nonlinear equation that may cause numerical instability. Lun et al. [139] developed a model based on dense phase kinetic gas theory [84, 139] and the model is employed to describe the contact normal stress τ in Eq. (2.64),

$$\tau = [\theta_s \bar{\rho}_s + \theta_s^2 \bar{\rho}_s (1 + e) g_0] \Theta_s, \tag{2.67}$$

where g_0, $\bar{\rho}_s$, and e represent respectively the radial distribution function, the mean density of particles in a local cell, and the coefficient of restitution. The granular temperature Θ_s is given in Eq. (2.17). Radial distribution function g_0 can be modeled by

$$g_0 = \frac{3}{5}[1 - (\frac{\theta_s}{\theta_{cp}})^{\frac{1}{3}}]^{-1}. \tag{2.68}$$

2.6　Chemical conversion model

The thermo-chemical conversion of biomass particles involves drying, pyrolysis, and heterogeneous reactions of char. These physical and chemical processes have been extensively investigated while the biomass pyrolysis and heterogeneous reactions of char pose more challenges.

2.6.1　Pyrolysis model

The pyrolysis of biomass involves complex physical and chemical processes that have not been fully understood. Biomass pyrolysis produces a large variety of species in the products which depend on several factors, e.g., biomass constitution, heating rates, particle size, residence time, and operating conditions [116]. Figure 2.4 shows the drying and primary and secondary pyrolysis processes. The biomass pyrolysis is usually accompanied by complex physical processes, e.g., heat transfer by conduction, convection, and radiation, pressure gradients interior to degrading particle, surface regression, shrinkage, diffusion, and convection through a hot particle layer, and condensation [159]. According to the operating conditions, the pyrolysis process can be divided into conventional/slow pyrolysis, fast pyrolysis, and flash pyrolysis, see Tabel 2.2. In slow pyrolysis, the
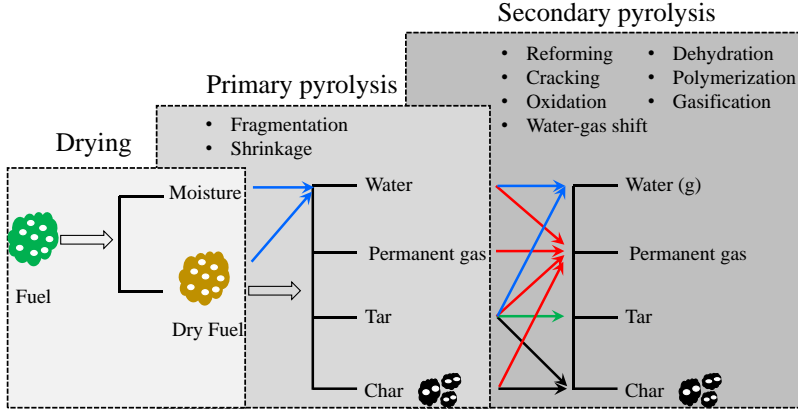
Figure 2.4: Thermochemical conversion route of primary and secondary pyrolysis reactions [116]. Note: The figure is reproduced with permission from the author.

operating temperature is typically 300 - 700 °C with a heating rate less than 1 °C/s. The biomass particle size is typically larger than 5 mm, favoring long vapor residence time. The slow pyrolysis promotes more solid and gas products. For fast pyrolysis, the biomass particle size is typically smaller than 3 mm, the operating temperature is 400 - 800 °C, and the heating rate is 10 - 200 °C/s. The small size particle promotes the quick heat conduction in the particle leading to a fast escape of volatile. Low vapor residence time results in minimizing secondary reactions and gives high yields of liquid products. Flash pyrolysis, which favors more liquid products over fast or slow pyrolysis, has a higher operating temperature, i.e., 800 - 1000 °C, and a more rapid heating rate, i.e., near 1000 °C/s. Fast or flash pyrolysis typically occurs in high-temperature reactors, e.g., fluidized beds, ablative systems, and vacuum pyrolysis systems. The chemical reactions during the pyrolysis process, especially fast and flash pyrolysis, are difficult to reveal because several reactions occur too rapidly to capture. Despite several challenges, various chemical kinetic models have been developed based on various assumptions. In the past few years, biomass pyrolysis models have been reviewed by several researchers, e.g., Hameed et al. [25], Vikram et al. [162], Kaczor et al. [122], Wang et al. [163], Kersten et al. [164] and Fatehi et al. [5]. Four different types of biomass pyrolysis models can be identified based above literature: (a) single-step model, (b) three-parallel-step model with secondary tar cracking reactions, (c) FG-DVC model, and (d) multicomponent pyrolysis model.
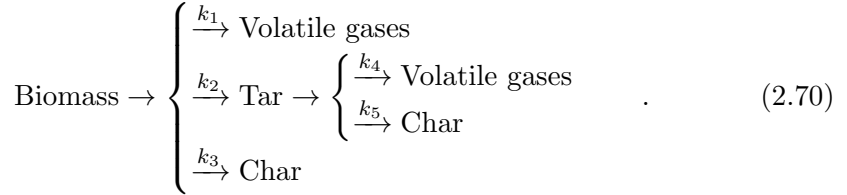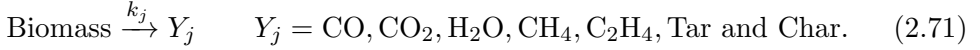
Single-step kinetic model:

$$\text{Biomass} \xrightarrow{k} \text{Volatile gases} + \text{Char}. \tag{2.69}$$

Table 2.2: Pyrolysis products under different operating conditions [160–162].

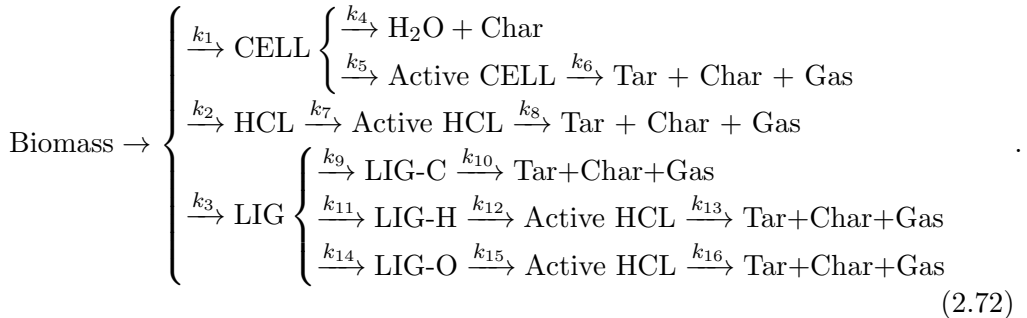| Pyrolysis	Operating conditions	Results
Slow pyrolysis	Fuel size: 5 - 50 mm	Gases: $\sim$ 35 wt %
	Temperature: 300 - 700 °C	Biochar: $\sim$ 35 wt %
	Heating rate: 0.1 - 1 °C/s	Bio-oil: $\sim$ 30 wt %
	Vapor residence time: 10 - 100 min	
Fast pyrolysis	Fuel size: $\sim$3 mm	Gases: $\sim$ 30 wt %
	Temperature: 400 - 800 °C	Biochar: $\sim$ 20 wt %
	Heating rate: 10 - 200 °C/s	Bio-oil: $\sim$ 50 wt %
	Vapor residence time: 0.5 - 5 min	
Flash pyrolysis	Fuel size: $\sim$0.2 mm	Gases: $\sim$ 13 wt %
	Temperature: 800 - 1000 °C	Biochar: $\sim$ 12 wt %
	Heating rate: $\sim$1000 °C/s	Bio-oil: $\sim$ 75 wt %
	Vapor residence time: $\sim$ 0.5 s	

Three-parallel-step model:

$$
\text{Biomass} \rightarrow
\begin{cases}
\xrightarrow{k_1} \text{Volatile gases} & \\
\xrightarrow{k_2} \text{Tar} \rightarrow
\begin{cases}
\xrightarrow{k_4} \text{Volatile gases} \\
\xrightarrow{k_5} \text{Char}
\end{cases} \\
\xrightarrow{k_3} \text{Char}
\end{cases}
. \qquad (2.70)
$$

FG-DVC model:

$$
\text{Biomass} \xrightarrow{k_j} Y_j \qquad Y_j = \text{CO}, \text{CO}_2, \text{H}_2\text{O}, \text{CH}_4, \text{C}_2\text{H}_4, \text{Tar and Char}. \qquad (2.71)
$$

Multicomponent pyrolysis:

$$
\text{Biomass} \rightarrow
\begin{cases}
\xrightarrow{k_1} \text{CELL}
\begin{cases}
\xrightarrow{k_4} \text{H}_2\text{O} + \text{Char} \\
\xrightarrow{k_5} \text{Active CELL} \xrightarrow{k_6} \text{Tar} + \text{Char} + \text{Gas}
\end{cases} \\
\xrightarrow{k_2} \text{HCL} \xrightarrow{k_7} \text{Active HCL} \xrightarrow{k_8} \text{Tar} + \text{Char} + \text{Gas} \\
\xrightarrow{k_3} \text{LIG}
\begin{cases}
\xrightarrow{k_9} \text{LIG-C} \xrightarrow{k_{10}} \text{Tar+Char+Gas} \\
\xrightarrow{k_{11}} \text{LIG-H} \xrightarrow{k_{12}} \text{Active HCL} \xrightarrow{k_{13}} \text{Tar+Char+Gas} \\
\xrightarrow{k_{14}} \text{LIG-O} \xrightarrow{k_{15}} \text{Active HCL} \xrightarrow{k_{16}} \text{Tar+Char+Gas}
\end{cases}
\end{cases}
.
$$
$$(2.72)$$

In Eqs (2.69 - 2.72), k denotes the Arrhenius rate constant, and the subscripts of k denote various chemical reactions. The single-step kinetic pyrolysis model is an empirical model which converts biomass particles to volatile and char using a first-order single-step reaction, as shown in Eq. (2.69). Individual biomass constituents and pyrolysis products are lumped into product classes,

i.e., char and volatile. The appropriate heat transfer and simple shrinkage models can be employed in the global kinetic model. The parameters of the global model can be derived from the experiments using the Kissinger model [165], Kissinger–Akahira–Sunose (KAS) [166], and Flynn–Wall–Ozawa (FWO) approaches [167]. The one-step global pyrolysis model does not consider the detailed chemistry of the pyrolysis process, e.g., the formation and decomposition of tar. Meanwhile, it fails to describe the total mass loss as a function of pyrolysis temperature/resident time and cannot accurately estimate the individual product yields and distribution. Although several drawbacks, the one-step model has the advantage of low computational cost and good prediction of flue gas compositions. Hence, the model is widely employed in 3D CFD simulations [58, 59, 67, 86–88, 102, 103, 126, 127, 168, 169].

The three-parallel-step model is introduced to describe the more detailed pyrolysis process, including primary and secondary pyrolysis processes, see Eq. (2.70). The three-parallel-step model can be divided into two chemical stages. In the first stage, biomass is decomposed to produce chars, tar/bio-oil, and volatile with various kinetic reactions. In the secondary stage, the intermediate tar further cracks into the volatile and char. The three-parallel-step model improves the prediction of biomass pyrolysis; however, it fails to predict the pyrolysis yields at various operating conditions [170]. The kinetic data are typically derived from specific experiments. When operating conditions differ from specific ones, it may cause a significant error. Meanwhile, it is pretty questionable that the chemical products with very different properties are grouped into one category in this model, e.g., the liquid phase contains water and tar. A more detailed pyrolysis model should be further developed to predict the biomass pyrolysis process.

A functional group-depolymerization, vapourization, and cross-linking (FG-DVC) model widely used in coal devolatilization was extended to investigate the biomass pyrolysis process by Chen et al. [171], as shown in Eq. (2.71). The model contains a functional group (FG) model and a depolymerization, vapourization, and cross-linking (DVC) model. The FG model is used to describe the evolution of volatile, and the DVC model is used to predict the formation of the tar and char [170]. The release of volatile and tar is modeled using one or more FG models in which each reaction is given a chemical parameter. The FG-DVC model improves the prediction of the volatile species over time; however, it only can provide a precise prediction for the operating conditions and fuels from which the kinetic parameters are derived. The product yields are the inputs of the FG-DVC model, so the effects of operating conditions on the tar yield can not be predicted.

Ranzi et al. [118, 119, 172] and Corbetta et al. [173] proposed a more detailed pyrolysis model to describe the complex chemical mechanism of biomass pyrolysis, as shown in Eq. (2.72). The detailed pyrolysis model is a multi-component pyrolysis mechanism in which each biomass component, i.e., cellulose, hemicellulose, and lignin, is described by various sub-mechanisms. In this model, the volatile is represented by 20 representative species. Simplified mechanisms for each component are derived from semi-detailed kinetic models, and the sub-mechanism of cellulose pyrolysis is derived from the model of Piskorz et al. [174]. Hemicellulose decomposition is modeled using a two-step pyrolysis model, which is similar to the mechanism of cellulose in the first step. Lignin decomposition is a skeleton mechanism of the detailed chemistry mechanism proposed by Faravelli et al. [175] and is described using several steps. In the multi-component pyrolysis model, the biomass pyrolysis process can be characterized by the sum of the contributions of cellulose, hemicellulose, and lignin. The mass loss evolution over time and operating conditions can be predicted with high accuracy. However, the secondary char heterogeneous reactions and the interaction between various components are not considered in this model, which might affect the evolution of mass loss and product yields. In addition, the multi-component pyrolysis model significantly increases the computational cost when employed in the 3D CFD simulations with many biomass particles. More detailed pyrolysis models are still required for biomass pyrolysis, bringing researchers into what needs further studies of the fundamentals of pyrolysis in depth.

2.6.2 Heterogeneous reaction model

In addition to pyrolysis, the heterogeneous reaction of char is another important process in biomass thermo-chemical conversion. The yields and heterogeneous reactions of char are highly affected by pyrolysis conditions. The low char yields are associated with high yields of volatile and tar. The heterogeneous reaction rates of char conversion are crucial to revealing detailed biomass conversion processes. The overall kinetics of char conversion can be measured via the reactivity $r_{c,i}$ given by

$$r_{c,i} = -\frac{1}{m_{char,i}}\frac{\partial m_{char,i}}{\partial t} = \frac{1}{1-c}\frac{\partial c}{\partial t}, \qquad (2.73)$$

where $m_{char,i}$ is the mass of the organic portion of the char particle, $\partial m_{char,i}/\partial t$ is the conversion rate and c is the degree of conversion given by

$$c = \frac{m_{char,i} - m_{char,i0}}{m_{char,i\infty} - m_{char,i0}}, \qquad (2.74)$$

where $m_{char,i0}$ and $m_{char,i\infty}$ denote the initial and final mass of the ith char paritcle, respectively.
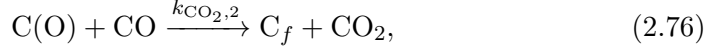
Models for char reactions are typically classified into structural and volumetric models. The structural models consider the internal actual pore structure during char conversion. In the volumetric models, changes in the porous structure are modeled by the empirical correlations in which the porosity properties are considered implicitly. Di Blasi [117] summarized the factors that affect the reactivity of char conversion into the following categories: (1) film diffusion of oxidizing/gasifying agent, (2) diffusion through the ash layer and the particle, (3) adsorption on the reaction surface, (4) chemical reaction, (5) desorption of product gas from the surface, (6) diffusion of product gas through the particle and the ash layer, (7) film diffusion back into the ambient gas. Category (4) addresses the influence of surface chemical reaction, whereas the other categories consider the influence of mass transport of surrounding gas on the char reactivity.

The char conversion process can be divided into three main regimes based on the Thiele modulus and the effectiveness factor [176, 177]. The Thiele modulus is the ratio of the overall reaction rate to the internal diffusion rate. The effectiveness factor is the actual reaction rate to the rate at which all the surfaces throughout the internal pores are exposed to the gaseous reactant. For regime I, the Thiele modulus is small, and the effectiveness factor is ideally unity. The regime is characterized by the low operating temperature and the small particle size, which leads to a faster diffusion rate over the chemical reaction rate. The char particle changes in density with constant particle size, and the diffusion rate is a function of the conversion degree. As the particle size increases, the diffusion rate of the porous char particles in regime II becomes slow, leading to a limited gaseous reactant penetration into the char particle. The Thiele modulus is much greater than unity and the effectiveness factor is much less than unity in regime II. The chemical reactions mainly occur on the exterior surface of the particle leading to a varying particle size with constant density. The reaction rate is proportional to the external surface area of the char particle. For regime III, the char particle shrinks at constant density, and the mass transfer of the gaseous reactant plays a critical role in the char conversion. The reaction rate is proportional to the external surface of the char particle and a mass transfer coefficient.
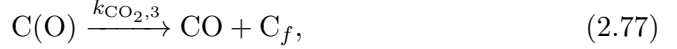
The kinetic models of char conversion developed in recent decades do not consider all the fundamental components because these micro-level reactions are difficult to measure during the conversion process. Therefore, the global reactivity models which take into account the interaction between the char and the gas phase are widely used to investigate the char chemical conversion. The

widely applied mechanisms of char are the reaction of char with CO_2, H_2O, and air.

CO_2 gasification of char: The CO_2 gasification of char involves the chemical reactions [117, 177, 178] given by

$$C_f + CO_2 \xrightarrow{k_{CO_2,1}} C(O) + CO, \tag{2.75}$$

$$C(O) + CO \xrightarrow{k_{CO_2,2}} C_f + CO_2, \tag{2.76}$$

and

$$C(O) \xrightarrow{k_{CO_2,3}} CO + C_f, \tag{2.77}$$

where $k_{CO_2,1}$, $k_{CO_2,2}$ and $k_{CO_2,3}$ are the Arrhenius rate constants. C_f denotes an active carbon site and $C(O)$ is a carbon-oxygen complex. The gasification rate, $k_{CO_2,c}$, based on the steady-state assumption for $C(O)$ complex can be given by

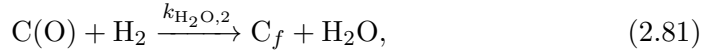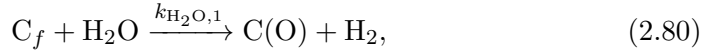$$k_{CO_2,c} = \frac{k_{CO_2,1}P_{CO_2}}{1 + (k_{CO_2,2}/k_{CO_2,3})P_{CO} + (k_{CO_2,1}/k_{CO_2,3})P_{CO_2}}, \tag{2.78}$$

where P_{CO_2} and P_{CO} are the partial pressure of CO_2 and CO. If the CO concentrations are low and the inhibiting effect of gas mass transportation is neglected, the gasification reactions (2.75 $\sim$ 2.77) can be simplified as a global model given by

$$C + CO_2 \xrightarrow{k_{CO_2,c}} 2CO, \qquad k_{CO_2,c} = A exp(-E/RT)P_{CO_2}^n, \tag{2.79}$$
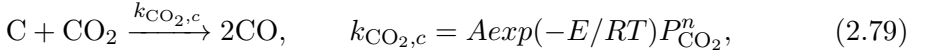
where A denotes the pre-exponential factor. E denotes the activation energy. R is the universal gas constant and n is an empirical parameter.

H_2O gasification of char: The H_2O gasification of char involves several chemical reactions [117, 179, 180] and can be expressed as

$$C_f + H_2O \xrightarrow{k_{H_2O,1}} C(O) + H_2, \tag{2.80}$$

$$C(O) + H_2 \xrightarrow{k_{H_2O,2}} C_f + H_2O, \tag{2.81}$$

$$C(O) \xrightarrow{k_{H_2O,3}} CO, \tag{2.82}$$

$$C_f + H_2 \xrightarrow{k_{H_2O,4}} C(H)_2, \tag{2.83}$$

$$C(H)_2 \xrightarrow{k_{H_2O,5}} C_f + H_2, \tag{2.84}$$

$$C_f + \frac{1}{2}H_2 \xrightarrow{k_{H_2O,6}} C(H), \tag{2.85}$$

and

$$C(H) \xrightarrow{k_{H_2O,7}} C_f + \frac{1}{2}H_2, \tag{2.86}$$
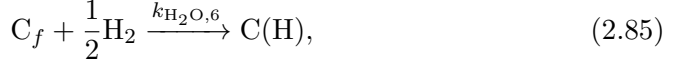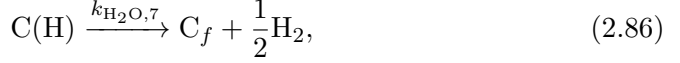
where $k_{H_2O,1\sim7}$ are Arrhenius rate constants. The oxygen reaction mechanism involves reactions (2.80 $\sim$ 2.82) and hydrogen inhibition mechanism may contain reactions (2.80), (2.81), (2.83) and (2.84) or reactions (2.80), (2.81), (2.85) and (2.86). The steam gasification rate based on reactions (2.80 $\sim$ 2.86) can be given by, assuming the C(O), C(H) and C(H)$_2$ in steady-state,

$$k_{H_2O,c} = \frac{k_{H_2O,1}P_{H_2O}}{1 + (k_{H_2O,1}/k_{H_2O,3})P_{H_2O} + f(P_{H_2})}, \tag{2.87}$$

where P_{H_2O} and P_{H_2} are the partial pressure of H$_2$O and H$_2$, respectively. $f(P_{H_2})$ which depends on the selected mechanism. $f(P_{H_2})$ may be given by $k_{H_2O,2}/k_{H_2O,3}P_{H_2}$, $k_{H_2O,4}/k_{H_2O,5}P_{H_2}$, or $k_{H_2O,6}/k_{H_2O,7}P_{H_2}^{0.5}$.

The chemical reactions (2.80 $\sim$ 2.86) of steam gasification can be simplified as a global reaction, similar to CO$_2$ gasification. The global reaction and reaction rate $k_{H_2O,c}$ can be given by

$$C + H_2O \xrightarrow{k_{H_2O,c}} CO + H_2, \qquad k_{H_2O,c} = Aexp(-E/RT)P_{H_2O}^n. \tag{2.88}$$
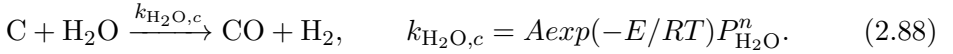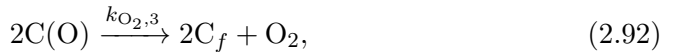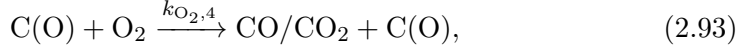
The Arrhenius parameters in global reactions (2.79) and (2.88) have been extensively investigated. Bi Blasi [117] reviewed the parameters of biomass char gasification at 800 $\sim$ 1000 °C of temperature and $\sim$ 101 kPa of pressure. A general form of gasification rate can be given by

$$\frac{dc}{dt} = k_{i,c}P_i \times f(c), \qquad k_{i,c} = A_iexp(-E_i/RT), \quad i = CO_2, H_2O, \tag{2.89}$$

where $f(c)$ is the function of conversion progress c. Simple Arrhenius laws, which take into account the contribution of chemical kinetics and structural terms, were widely used [181, 182]. In particular, the effects of partial pressure can be expressed implicitly by incorporating the pre-exponential factor.

Char combustion: The char combustion reactions [117] are given by

$$2C_f + O_2 \xrightarrow{k_{O_2,1}} 2C(O), \tag{2.90}$$

$$C(O) \xrightarrow{k_{O_2,2}} CO, \tag{2.91}$$

$$2C(O) \xrightarrow{k_{O_2,3}} 2C_f + O_2, \tag{2.92}$$

$$C(O) + O_2 \xrightarrow{k_{O_2,4}} CO/CO_2 + C(O), \qquad (2.93)$$

and

$$C_f + CO_2 \xrightarrow{k_{O_2,5}} CO + C(O), \qquad (2.94)$$
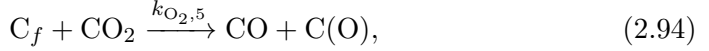
where $k_{O_2,1\sim5}$ are Arrhenius rate constants.

Similar to the reactions of char gasification, a simplified global reaction of char combustion is widely used and can be given by

$$C + O_2 \xrightarrow{k_{O_2,c}} CO/CO_2, \qquad k_{O_2,c} = Aexp(-E/RT)P_{O_2}^n, \qquad (2.95)$$

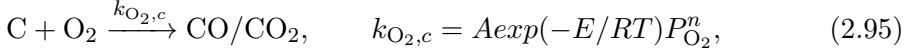where $k_{O_2,c}$ is reaction rate of char. P_{O_2} denotes the partial pressure of O_2. In addition, multi-step models have been proposed to describe the char conversion [183, 184]. The low-temperature oxidation of char is considered in the multi-step model. The reaction mechanisms of char combustion have been extensively studied; however, the mechanisms of char reaction at the micro-level have not been fully understood. Detailed chemical mechanisms of char conversion are still to be developed.

2.7 Existing CFD programs and software

The numerical models of dense particle-fluid systems have been implemented in several commercial software and in-house codes. The commercial and in-house software platforms are listed in Table 2.3, in which the number of papers in the literature reporting on the simulation of fluidized beds based on various commercial and in-house codes is indicated. The statistic is based on the review of Alobaid et al. [21], while it does not mean that the number of literature includes all relevant articles on the modeling of fluidized beds. The commercial CFD software frequently used includes ANSYS-FLUENT, BARRACUDA, COMSOL, and STAR-CCM+, as well as some commercial software that researchers and engineers have been using, e.g., PHOENICS, FLOW-3D, XPS, FIDAP, YALES2, Rocky DEM, PyGran, and Flotracs. In-house codes involve OpenFOAM, MFIX, and CFDEM, as well as the in-house codes developed by several groups, e.g., Prof. Kuipers (Eindhoven University of Technology), Prof. Horio (Tokyo University), Prof. Peters (XDEM, University of Luxembourg), Prof. Sommerfeld (Otto von Guericke University Magdeburg), Prof. Scherer (Ruhr-University Bochum), and Prof. Breuer (LESOCC, Helmut Schmidt University).As shown in Table 2.3, the vast literature on the modeling of dense gas-solid flow is widely conducted using well-established CFD tools, such as ANSYS-FLUENT, BARRACUDA, and OpenFOAM. Fundamental research on

fluidized beds is typically conducted using in-house codes. Most of these studies are based on the Euler-Euler model at the macro level, while few studies are based on Eulerian-Lagrangian models, especially combustion and gasification in industrial-scale fluidized beds.

Table 2.3: Statistics on the number of papers reported in the literature conducted based on various commercial and in-house codes [21].

Software	TFM		HM		DEM-S		DEM-H	
	Non-R.	R.	Non-R.	R.	Non-R.	R.	Non-R.	R.
ANSYS(FLUENT) [185]	14	175	15	16	15	18	2	3
OpenFOAM [186]	4	5	6	11	22	9	✕	✕
MFIX/theK-FIX [187]	6	27	4	✕	12	6	✕	✕
BARRACUDA [188]	✕	✕	8	34	✕	✕	✕	✕
LIGGGHTS&CFDEM [189]	✕	✕	✕	✕	14	2	✕	✕
COMSOL [190]	5	3	✕	✕	3	✕	✕	✕
STAR-CD/CCM+ [191]	4	✕	✕	✕	7	1	✕	✕
EDEM [192]	✕	✕	✕	✕	8	1	✕	✕
Others	5	33	✕	✕	27	10	28	5

Note: DEM-S and DEM-H represent the DEM model coupled with the soft-sphere and hard-sphere models, respectively. R. denotes the reactive flow and Non-R. denotes non-reactive flow processes. HM denotes the hybrid model.

Chapter 3

MP-PIC method for biomass combustion and gasification in FB reactors

The theory and mathematical models for dense fluid-particle flows under FB reactor conditions used in this thesis are described in this chapter. In particular, the MP-PIC method described in Section 2.5 is selected in this thesis, in which the governing equations for the gas phase are made up of the conservation equations of mass, momentum, energy, and species. The interaction between the discrete and continuous phases is modeled using appropriate source terms. In FB reactors, the flow is turbulent. The governing equations described in Chapter 2 can be used to simulate the thermochemical process in biomass combustion and gasification at a single particle level; however, they can not be directly used for FB reactors due to the multiple scales existing in a turbulent flow in a reactor level, which requires too high computational resources to resolve. Instead, turbulence closure models are employed. A description of the turbulence closure models is given below, followed by a summary of the specific sub-models used in this thesis for the particle phase and the interaction between the gas and solid phase. Finally, a brief description of the numerical methods used in this thesis is presented.

3.1 Gas phase governing equations

Reynolds averaged Navier-Stokes (RANS) approach is used to describe the mean gas flow in the FB reactors. The gas phase governing equations consist of the Reynolds-averaged continuity, momentum, energy, and species transport equations [143]. The Reynolds averaged continuity equation is obtained by applying the Reynolds average on Eq. (2.19),

$$\frac{\partial \left(\alpha_g \overline{\rho}_g \right)}{\partial t} + \nabla \cdot \left(\alpha_g \overline{\rho}_g \widetilde{\mathbf{u}}_g \right) = \overline{S}_{m,g}, \tag{3.1}$$

where overbar and tilde denote Reynolds averaged, and Favre averaged, respectively. α_g, ρ_g, and $\mathbf{u}_g$ are the gas volume fraction, the gas density, and the velocity vector of the gas phase, respectively. $S_{m,g}$ represents the gas formation rate due to the thermochemical conversion of the fuel particles.

The Reynolds averaged momentum equations are obtained similarly from Eq. (2.20),

$$\frac{\partial \left(\alpha_g \overline{\rho}_g \widetilde{\mathbf{u}}_g \right)}{\partial t} + \nabla \cdot \left(\alpha_g \overline{\rho}_g \widetilde{\mathbf{u}}_g \widetilde{\mathbf{u}}_g \right) = -\alpha_g \nabla \overline{p}_g + \nabla \cdot \left(\alpha_g \overline{\tau}_g \right) + \overline{\mathbf{S}}_{u,g}, \tag{3.2}$$

where p_g is the gas pressure, τ_g is the sum of viscous stress and Reynolds stress, and $\mathbf{S}_{u,g}$ is the source term of momentum exchange from the solid phase.

The Reynolds averaged energy equation is obtained from Eq. (2.21),

$$\frac{\partial \left(\alpha_g \overline{\rho}_g (\widetilde{h} + \widetilde{K}) \right)}{\partial t} + \nabla \cdot (\alpha_g \overline{\rho}_g \widetilde{\mathbf{u}}_g (\widetilde{h} + \widetilde{K})) = \alpha_g \frac{\partial \overline{p}_g}{\partial t}$$
$$+ \nabla \cdot (\alpha_g \overline{\rho}_g \Gamma_g \nabla \widetilde{h}) + \overline{Q}_r + \overline{Q}_{com} + \overline{S}_{h,g}, \tag{3.3}$$

where h denotes the specific enthalpy of the gas, and K denotes the kinetic energy of the gas flow. $\overline{Q}_r$ denotes the mean source term due to radiative heat transfer, $\overline{Q}_{com}$ denotes the mean source term due to volatile chemical reactions, and $\overline{S}_{h,g}$ denotes the mean source term due to thermochemical conversion of the solid fuel. Heat diffusion coefficient Γ_g is the sum of the molecular and turbulent heat diffusion coefficients given by

$$\Gamma_g = \Gamma_l + \frac{\mu_t}{\overline{\rho}_g Pr_t}, \tag{3.4}$$

where Γ_l is the molecular heat diffusion coefficient, Pr_t is the turbulent Prandtl number and μ_t is the turbulent eddy viscosity.

The Reynolds averaged species transport equation is obtained from Eq. (2.22),

$$\frac{\partial \left(\alpha_g \overline{\rho}_g \widetilde{Y}_{g,k}\right)}{\partial t} + \nabla \cdot \left(\alpha_g \overline{\rho}_g \widetilde{\mathbf{u}}_g \widetilde{Y}_{g,k}\right) = \nabla \cdot \left(\alpha_g \overline{\rho}_g D_g \nabla \widetilde{Y}_{g,k}\right) + \overline{\dot{\omega}}_{g,k} + \overline{S}_{Y_{g,k}}, \quad (3.5)$$

in which $Y_{g,k}$ is the mass fraction of species k in the gas mixture, and $\overline{\dot{\omega}}_{g,k}$ denotes the mean chemical reaction rate of species k. $\overline{S}_{Y_{g,k}}$ denotes the mean formation rate of species k due to thermochemical conversion of the solid fuel particles. The mass diffusion coefficient D_g for species k taking both the viscous and turbulent contributions into account and is given by

$$D_g = D_l + \frac{\mu_t}{\overline{\rho}_g Sc_t}, \quad (3.6)$$

where D_l is the mass diffusion coefficient for species k due to viscous contribution and Sc_t is the turbulent Schmidt number.

A Partially Stirred Reactor (PaSR) model is used to account for turbulence chemistry interaction when computing the mean source terms due to gas phase chemical reactions ($\overline{\dot{\omega}}_{g,k}$, $\overline{\dot{Q}}_{com}$) [193]. In the PaSR model, the mean reaction rates are modeled as

$$\overline{\dot{\omega}}_{g,k} = \kappa \dot{\omega}_{g,k}(\widetilde{Y}, \widetilde{T}, \overline{p}), \quad (3.7)$$

in which κ is the volume fraction of the reactive mixture and given by,

$$\kappa = \frac{\tau_c}{\tau_c + \tau_m}, \quad (3.8)$$

where τ_c and τ_m denote the local chemical reaction time and the local mixing time, respectively. The chemical reaction time τ_c, is determined from the mean reaction rates of the fuel $\dot{\omega}_f(\widetilde{Y}, \widetilde{T}, \overline{p})$ and the oxidizer or the gasification agents $\dot{\omega}_o(\widetilde{Y}, \widetilde{T}, \overline{p})$,

$$\frac{1}{\tau_c} = max\{\frac{-\dot{\omega}_f}{Y_f}, \frac{-\dot{\omega}_o}{Y_o}\}, \quad (3.9)$$

where subscripts f and o denote the fuel and oxidizer or the gasification agents, respectively. The mixing time τ_m is modeled as

$$\tau_m = C_{mix}\sqrt{\frac{\nu}{\varepsilon}}, \quad (3.10)$$

where C_{mix} is a model constant ($C_{mix} = 1.0$ in this thesis). ν and ε denote the kinematic viscosity and the dissipation rate of turbulent kinetic energy, respectively.

The stress tensor $\overline{\tau}_g$ in Eq. (3.2) is the sum of the viscous and Reynolds stresses and can be written as

$$\overline{\tau}_g = \overline{\tau}_l + \overline{\tau}_t. \tag{3.11}$$

The stress tensor for a Newtonian fluid τ_l is expressed as

$$\overline{\tau}_l = \mu_g((\nabla\widetilde{\mathbf{u}}_g) + (\nabla\widetilde{\mathbf{u}}_g)^T - \frac{2}{3}(\nabla\cdot\widetilde{\mathbf{u}}_g)\mathbf{I}), \tag{3.12}$$

and the Reynolds stress τ_t is modeled according to

$$\overline{\tau}_t = \mu_t((\nabla\widetilde{\mathbf{u}}_g) + (\nabla\widetilde{\mathbf{u}}_g)^T - \frac{2}{3}(\nabla\cdot\widetilde{\mathbf{u}}_g)\mathbf{I}) - \frac{2}{3}\overline{\rho}_g k\mathbf{I}, \tag{3.13}$$

Standard $k - \varepsilon$ model is employed to determine the eddy viscosity,

$$\mu_t = \overline{\rho}_g\frac{C_\mu k^2}{\varepsilon}, \tag{3.14}$$

where k is the turbulent kinetic energy. k and ε are modeled using the following transport equations:

$$\frac{\partial\left(\alpha_g\overline{\rho}_g k\right)}{\partial t} + \nabla\cdot\left(\alpha_g\overline{\rho}_g\widetilde{\mathbf{u}}_g k\right) = \nabla\cdot\left(\alpha_g(\mu_g + \frac{\mu_t}{\sigma_k})\nabla k\right) + \alpha_g P_k - \alpha_g\overline{\rho}_g\varepsilon, \tag{3.15}$$

$$\frac{\partial\left(\alpha_g\overline{\rho}_g\varepsilon\right)}{\partial t} + \nabla\cdot\left(\alpha_g\overline{\rho}_g\widetilde{\mathbf{u}}_g\varepsilon\right) = \nabla\cdot\left(\alpha_g(\mu_g + \frac{\mu_t}{\sigma_\varepsilon})\nabla\varepsilon\right) + \alpha_g\frac{\varepsilon}{k}(C_{\varepsilon_1}P_k - C_{\varepsilon_2}\overline{\rho}_g\varepsilon), \tag{3.16}$$

where $P_k = \overline{\tau}_t : \nabla\widetilde{\mathbf{u}}_g$ is the production rate of turbulent kinetic energy. Standard values of model constants are used, $C_\mu = 0.09$, $C_{\varepsilon1} = 1.44$, $C_{\varepsilon2} = 1.92$, $C_{\sigma k} = 1.0$ and $C_{\sigma\varepsilon} = 1.3$ [58, 194]. The mean source terms due to the particle/gas interaction in Eqs. (3.1, 3.2, 3.3 and 3.5), i.e., $\overline{S}_{m,g}$, $\overline{\mathbf{S}}_{u,g}$, $\overline{S}_{h,g}$ and $\overline{S}_{Y_{g,k}}$, require the modeling of particle phase as discussed below.

3.2 Solid phase governing equations

In the MP-PIC approach, biomass and sand particles are tracked using the Lagrangian approach. The interactions between the particles and the surrounding gas are through mass and momentum exchange and heat transfer. The mass, momentum, and energy conservation equations for the solid phase in the Lagrangian framework are presented in the following. For simplicity, the Reynolds/Favre averaged gas properties are indicated without using over-bars or tildes.

3.2.1 Mass conversion of solid phase

As discussed earlier, biomass particles undergo thermochemical conversion reactions, i.e., drying, pyrolysis, and the heterogeneous reaction of char, while sand particles are assumed to be chemically inert. A detailed survey of various sub-models for these processes has been presented in the previous chapter. In this section, the specific sub-models used in the thesis are presented.

The mass conservation equation for the i-th biomass particle is written as

$$\frac{dm_i}{dt} = \dot{m}_{vapor,i} + \dot{m}_{devol,i} + \dot{m}_{char,i}, \qquad (3.17)$$

where m_i, $\dot{m}_{vapor,i}$, $\dot{m}_{devol,i}$ and $\dot{m}_{char,i}$ denote the mass of i-th biomass particle, the evaporation rate, the devolatilization rate, and the char conversion rate, respectively.

3.2.1.1 Drying

The moisture evaporation rate is modeled as [168, 194],

$$\dot{m}_{vapor,i} = -\phi_{vapor,i} As_i M_v, \qquad (3.18)$$

where $\phi_{vapor,i}$, As_i, and M_v represent the molar flux of vapor, the surface area of the particle, and the molar weight of the vapor, respectively. $\phi_{vapor,i}$ is given by

$$\phi_{vapor,i} = k_c(C_{vapor,i} - C_{vapor,g}), \qquad (3.19)$$

where k_c, $C_{vapor,i}$ and $C_{vapor,g}$ denote, respectively, the mass transfer coefficient, vapor concentration at the particle surface, and the vapor concentration in the bulk gas. k_c, $C_{vapor,i}$ and $C_{vapor,g}$ can be described as

$$k_c = \frac{ShD_{diff,va}}{d_i}, \qquad (3.20)$$

$$C_{vapor,i} = \frac{P_{sat,T_i}}{R_u T_i}, \qquad (3.21)$$

and

$$C_{vapor,g} = X_v \frac{p_g}{R_u T_g}, \qquad (3.22)$$

where Sh is the Sherwood number, which is modeled using Ranz-Marshall correlation [195] and is given by,

$$Sh = (2 + 0.6Re_i^{1/2}Sc^{1/3}), \qquad (3.23)$$

where Sc is the Schmidt number of the surrounding gas. $D_{diff,va}$, P_{sat,T_i}, T_g, and X_v represent the vapor diffusion coefficient, the saturation pressure, the gas temperature, and the molar fraction of vapor in the surrounding gas, respectively. R_u is the universal gas constant, T_i is the particle temperature, and d_i is an equivalent spherical particle diameter computed based on the particle real-time mass m_i and a constant particle density ρ_i and is given by,

$$d_i = (6m_i/\pi\rho_i)^{1/3}, \tag{3.24}$$

where ρ_i is the particle density.

3.2.1.2 Pyrolysis

Chemical kinetic models for biomass pyrolysis have been discussed in Section 2.6.1. There are four different types of pyrolysis models. In fluidized bed furnaces, especially large-scale industrial furnaces, the number of biomass particles is enormous. It would require tremendously long computational time to carry out numerical simulations of a 3D fluidized bed furnace if multicomponent pyrolysis models were used. Thus, single-step models have been employed in fluidized bed simulations [58, 67, 103, 123–126].

The rate of devolatilization is computed based on the pyrolysis reaction model,

$$\dot{m}_{devol,i} = -A_d exp\left(-\frac{E_d}{R_u T_i}\right) m_{volat,i}, \tag{3.25}$$

where A_d and E_d are rate constants [58], $m_{volat,i}$ is the mass of the volatile remaining in the particle.

3.2.1.3 Char conversion

Char conversion is a complex process in which chemical reactions occur at the surface of the porous medium structure with complex interior and microstructures. The heterogeneous rates of char conversion are affected by the fundamental components, e.g., surface area, surface accessibility, carbon active sites, added inorganic matter, and the gaseous reactant concentration [117]. The rate of char conversion is computed based on all heterogeneous reactions,

$$\dot{m}_{char,i} = -\sum_{j=1}^{3} \dot{m}_{char,ij}, \tag{3.26}$$

where $\dot{m}_{char,ij}$ represent the char consumption rates by reactions with O_2, H_2O, and CO_2, respectively.

$$\dot{m}_{char,ij} = -As_i p_j R_{d,j} Da'_j, \tag{3.27}$$

where As_i denotes the particle surface, and p_j represents the partial pressure of the gasifying agents or oxidizers in the gas surrounding the particle. A normalized Damköhler number Da'_j, which is the ratio of the kinetic reaction rate to the mass transport rate [196], is defined to take into account the contribution of the kinetic and the diffusion rates,

$$Da'_j = -\frac{R_{kin,j}}{R_{d,j} + R_{kin,j}}, \tag{3.28}$$

where $R_{d,j}$ and $R_{kin,j}$ represent, respectively, the diffusion rate coefficient and kinetic rate coefficient. $R_{d,j}$ and $R_{kin,j}$ are defined as,

$$R_{d,j} = C_j \frac{[0.5(T_g + T_i)]^{0.75}}{d_i}, \tag{3.29}$$

and

$$R_{kin,j} = A_j exp\left(-\frac{E_j}{R_u T_i}\right), \tag{3.30}$$

where A_j and E_j represent the pre-exponential factor and activation energy for the char gasification reactions, respectively. C_j is the mass diffusion rate constant and $C_j = 5 \times 10^{-12}$ (s/$K^{0.75}$) [58].

3.2.2   Momentum equation of solid phase

The velocity of the i-th particle is governed by Newton's second law,

$$m_i \frac{d\mathbf{u}_i}{dt} = \mathbf{f}_{d,i} + \mathbf{f}_{\nabla_p,i} + m_i \mathbf{g} + \mathbf{f}_{\tau,i}. \tag{3.31}$$

The right-hand side terms represent the sum of all forces acting on the i-th particle by the surrounding gas and particles. The forces considered include, from left to right, the drag $\mathbf{f}_{d,i}$, pressure gradient $\mathbf{f}_{\nabla_p,i}$, gravity $m_i\mathbf{g}$, and interparticle stress $\mathbf{f}_{\tau,i}$. With a given $\mathbf{u}_i$, the position vector of the particle $\mathbf{x}_i$ is computed by integration of the equation

$$d\mathbf{x}_i/dt = \mathbf{u}_i. \tag{3.32}$$

3.2.2.1 Drag model

The drag force model widely used for the i-th individual particle $\mathbf{f}_{d,i}$ is given by [58, 84, 146]

$$\mathbf{f}_{d,i} = V_\Omega \beta (\mathbf{u}_g - \mathbf{u}_i), \tag{3.33}$$

where V_Ω is the volume of the computational cell, and β is the drag force parameter, which is modeled using the Wen & Yu drag correlation [84, 148] and is given as

$$\beta = \begin{cases} 150\frac{(1-\alpha_g)^2\mu_g}{\alpha_g^2 d_i^2} + 1.75\frac{(1-\alpha_g)\rho_g}{\alpha_g d_i}|\mathbf{u}_g - \mathbf{u}_i| & \alpha_g < 0.8 \\ \frac{3}{4}C_d\frac{(1-\alpha_g)\rho_g}{d_i}|\mathbf{u}_g - \mathbf{u}_i|\alpha_g^{-2.65} & \alpha_g \geq 0.8 \end{cases}, \tag{3.34}$$

where the drag coefficient C_d is modeled as [84]

$$C_d = \begin{cases} \frac{24}{Re_i}(1 + 0.15Re_i^{0.687}) & Re_i < 1000 \\ 0.44 & Re_i \geq 1000 \end{cases}, \tag{3.35}$$

where the particle Reynolds number Re_i is defined as

$$Re_i = \alpha_g \rho_g d_i |\mathbf{u}_g - \mathbf{u}_i| / \mu_g. \tag{3.36}$$

3.2.2.2 Interparticle stress

The particle stress $\mathbf{f}_{\tau,i}$ is given by

$$\mathbf{f}_{\tau,i} = V_\Omega \nabla \tau, \tag{3.37}$$

where the contact normal stress τ can be given by the model of Lun et al. [139],

$$\tau = [\theta_s \overline{\rho}_s + \theta_s^2 \overline{\rho}_s (1 + e)g_0]\Theta_s, \tag{3.38}$$

where g_0, $\overline{\rho}_s$, and e represent respectively the radial distribution function, the mean density of particles in a local cell, and the coefficient of restitution. The granular temperature Θ_s is given in Eq. (2.17). The radial distribution function g_0 can be modeled using equation (2.68).

The solid volume fraction of the i-th particle θ_s is modeled based on the particle distribution function $f(m_s, \mathbf{u}_s, \mathbf{x}_s, t)$ and can be given by

$$\theta_s = \iint f \frac{m_s}{\rho_s} dm_s du_s. \tag{3.39}$$

As discussed in Chapter 2, the particle velocity $\mathbf{u}_s$ is the particle velocity in the Eulerian frame, which is different from $\mathbf{u}_i$ in Eq. (3.31) that represents the velocity of the i-th particle in the Lagrangian framework.

In the MP-PIC model, f is obtained from the Liouville equation, which is the mathematical expression of the conservation of particle numbers per volume moving along dynamic trajectories in the particle phase space [106],

$$\frac{\partial f}{\partial t} + \nabla \cdot (f\mathbf{u}_s) + \nabla_u \cdot (f\mathbf{A}_s) = \frac{f_G - f}{\tau_G} + \frac{f_D - f}{\tau_D}. \tag{3.40}$$

The first term in the RHS of Eq. (3.40) denotes the collision return-to-isotropy effect and the second term denotes the collision damping effect. Physically, particle collision tends to dampen out the velocity fluctuations. The collision model assumed that within a damping relaxation time, the particle velocity approaches a mean value and the distribution function $f(m_s, \mathbf{u}_s, \mathbf{x}_s, t)$ approaches $f_D(m_s, \mathbf{u}_s, \mathbf{x}_s, t)$. The collision-damping particle distribution function $f_D(m_s, \mathbf{u}_s, \mathbf{x}_s, t)$ is given by [109, 110]

$$f_D(m_s, \mathbf{u}_s, \mathbf{x}_s, t) = \delta(\mathbf{u}_s - \overline{\mathbf{u}}_s) \int f d\mathbf{u}_s, \tag{3.41}$$

where δ is the Dirac function. The mean value of particle velocity can be given by

$$\overline{\mathbf{u}}_s = \frac{\int \int f m_s \mathbf{u}_s dm_s d\mathbf{u}_s}{\int \int f m_s dm_s d\mathbf{u}_s}. \tag{3.42}$$

The particle collision could result in a Gaussian distribution of particle velocity occurring within a relaxation time τ_G. The Gaussian distribution is described by the equilibrium-isotropic particle distribution function $f_G(m_s, \mathbf{u}_s, \mathbf{x}_s, t)$,

$$f_G(m_s, \mathbf{u}_s, \mathbf{x}_s, t) = G(\mathbf{u}_s; \overline{\mathbf{u}}_s, \sigma^2) \int f d\mathbf{u}_s, \tag{3.43}$$

where G is a Gaussian velocity distribution with the mean $\overline{\mathbf{u}}_s$ and variance σ^2, which can be obtained by enforcing that the variance of f_G is equal to that of f.

The relaxation time scale τ_D in the damping collision model is modeled as [109],

$$\frac{1}{\tau_D} = \frac{8\sqrt{2}}{3\pi} \theta_s \overline{\nu} g(\theta_s) \eta(1 - \eta), \tag{3.44}$$

and the relaxation time scale τ_G in the isotropic collision model is [110],

$$\frac{1}{\tau_G} = \frac{8\sqrt{2}}{5\pi} \theta_s \overline{\nu} g(\theta_s) \eta(2 - \eta), \tag{3.45}$$

where $g(\theta_s)$ is a factor given by $\theta_{cp}/(\theta_{cp} - \theta_s)$. η is defined as $(1 + e)/2$. θ_{cp} is the solid phase volume fraction at close packing. $\bar{\nu}$ is given by

$$\bar{\nu} = \frac{1}{r_{32}^3} \frac{\sum_s N_s (r_s + r_{32})^4 (\mathbf{u}_s - \bar{\mathbf{u}}_s)^2}{\sum_s N_s (r_s + r_{32})^2 \sqrt{(\mathbf{u}_s - \bar{\mathbf{u}}_s)^2}}, \tag{3.46}$$

where r_{32} is the Sauter mean radius given by

$$r_{32} = \frac{\int \int f r_s^3 dm_s d\mathbf{u}_s}{\int \int f r_s^2 dm_s d\mathbf{u}_s}, \tag{3.47}$$

and r_s is the effective particle radius given by

$$r_s = (\frac{m_s}{3/4\pi \rho_s})^{\frac{1}{3}}. \tag{3.48}$$

3.2.3 Energy equation of solid phase

The particle temperature is obtained from the energy conservation equation for the i-th particle,

$$q_i = m_i C_{p,i} \frac{dT_i}{dt} = q_{c,i} + q_{r,i} - q_{vapor,i} + q_{devol,i} + q_{char,ij}. \tag{3.49}$$

where $C_{p,i}$, $q_{c,i}$ and $q_{r,i}$ denote respectively the particle heat capacity, convective and radiative heat transfer. $q_{vapor,i}$, $q_{devol,i}$ and $q_{char,ij}$ represent the heat transfer of latent, pyrolysis, and char reactions.

The convection heat $q_{c,i}$ and radiation $q_{r,i}$ are given by

$$q_{c,i} = h_i A s_i (T_g - T_i), \tag{3.50}$$

and

$$q_{r,i} = \frac{\varepsilon_i A s_i}{4}(G - 4\sigma T_i^4), \tag{3.51}$$

where h_i, ε_i, σ, and G represent interphase thermal transfer coefficient, emissivity, Stefan-Boltzmann constant, and incident radiation, respectively. The interphase thermal transfer coefficient h_i can be given

$$h_i = \frac{Nu\lambda_g}{d_i}, \tag{3.52}$$

where λ_g is the thermal conductivity of the surrounding gas. Nu is the Nusselt number computed using the Ranz-Marshall correlation given by

$$Nu = 2 + \frac{3}{5}Re_i^{1/2}Pr^{1/3}, \tag{3.53}$$

where Pr is the Prandtl number of the surrounding gas. The incident radiation G is obtained from the P-1 radiation model.

The heat fluxes due to evaporation, pyrolysis, and char reactions are respectively $q_{vapor,i}$, $q_{devol,i}$ and $q_{char,ij}$, and can be given by

$$q_{vapor,i} = h_{vapor,i}\dot{m}_{vapor,i}, \tag{3.54}$$

$$q_{devol,i} = h_{devol,i}\dot{m}_{devol,i}, \tag{3.55}$$

and

$$q_{char,ij} = \sum_{j=1}^{3} h_{i,j}\dot{m}_{char,ij}, \tag{3.56}$$

where $h_{vapor,i}$, $h_{devol,i}$, and $h_{i,j}$ represent the latent heat, the heat of pyrolysis, and the heat of char reactions, respectively.

3.3 Numerical Method

3.3.1 Solution procedure for gas phase governing equations

The above-described governing equations are solved numerically using an open-source CFD code, OpenFoam v6 [186]. A finite-volume method was employed to solve the gas phase governing equations. Second-order "Gauss Limited-linear" schemes were used for spatial derivatives and the first-order Euler scheme was used for the integration of the time derivatives of the governing equations. The PIMPLE algorithm, which combines the advantage of PISO (Pressure Implicit with Splitting of Operator) and SIMPLE (Semi-Implicit Method for Pressure-Linked Equations) algorithms, was employed for velocity-pressure coupling in the continuity and momentum equations.

In order to obtain a numerical solution of the gas phase governing equations, the gas volume fraction (α_g, which is determined from the solid volume fraction θ_s, i.e., $\alpha_g = 1 - \theta_s$), and the source terms from the solid phase need to be determined. As shown in Eq. (3.39), θ_s is determined from the particle distribution function $f(m_s, \mathbf{u}_s, \mathbf{x}_s, t)$, which is described using the Liouville equation (3.40). This equation is solved using the computational particle method described in Refs. [105, 106, 197]. In this method, individual particle velocity and position along with its mass, temperature, and other physical properties are computed by solving the Lagrangian particle equations described in Section 3.2. Then, θ_s and source terms for the gas phase transport equations, which are quantities of

the Eulerian field, are determined by the ensemble average of the quantities of the individual Lagrangian particles.

3.3.2 Solution procedure for solid-phase governing equations

In order to achieve a converged statistical solution, a sufficiently large number of particles need to be simulated. This is not an issue since in fluidized bed reactors there is a sufficiently large number of particles. In practical simulations, not all these particles could be simulated. A coarse grain method (CGM) is employed in this thesis to reduce the computational cost. In the CGM approach, a finite number of virtual particles (hereafter referred to as parcels) are simulated. Assume that the number of parcels is N_p. The i-th parcel contains multiple real particles; however, all particles have the same properties, i.e., each real particle in the i-th parcel has the same mass m_i, velocity $\mathbf{u}_i$, temperature T_i and diameter d_i.

The governing equations for the individual real particles in the i-th parcel have been presented in Section 3.2. These equations are integrated to compute the particle quantities, i.e., m_i, $\mathbf{u}_i$, T_i, and d_i. Implicit backward Euler scheme is used in the temporal integration of these equations.

As an example, the velocity of the i-th particles is obtained by integrating Eq. (3.31). The discrete form of the velocity equation for the i-th particles can be written as [110],

$$\frac{\mathbf{u}_i^{n+1} - \mathbf{u}_i^n}{\Delta t} = D_i^n(\mathbf{u}_{g,i}^{n+1} - \mathbf{u}_i^{n+1}) + S_i^{n+1} + \frac{\bar{\mathbf{u}}_i^{n+1} - \mathbf{u}_i^n}{2\tau_D} \qquad (3.57)$$

where superscript n denotes the quantities at time t^n and Δt is the time step. The first term on the RHS is the drag term, and the second term S_i^{n+1} is the sum of source terms due to the pressure gradient force, gravity, and interparticle stress. The last term is explicitly added to model the effect of the collision damping term in the Liouville equation (3.40), where $\bar{\mathbf{u}}_i$ is the mass-weighted average of $\mathbf{u}_i$ [110].

In this discrete form of particle velocity equation, $\mathbf{u}_{g,i}^{n+1}$ is the gas velocity at $(\mathbf{x}_i, t^{n+1})$, which is computed from the gas velocity in the Euler grid around the particle position $\mathbf{x}_i$ at time t^{n+1}. A trilinear interpolation scheme is used to interpolate the Eulerian field quantities defined in the Euler cells to the discrete Lagrangian particle location $\mathbf{x}_i$. Fig. 3.1 illustrates the interpolation procedure.

Once the mass, velocity, temperature, and position are computed for all particles, the solid volume fraction (which is an Euler field quantity) can be computed from

the ensemble average of the particles. Assume that the number of real particles per unit volume that pertains to the i-th parcel is n_i. The solid volume fraction at $(\mathbf{x}, t)$ is

$$\theta(\mathbf{x}, t) = \frac{1}{V_\Omega} \sum_{i=1}^{N_p} n_i V_i(\mathbf{x}_i) S(\mathbf{x}, \mathbf{x}_i), \tag{3.58}$$

where V_i is the volume of the i-th particle. $\mathbf{x}_i$ is the location of the i-th particle, whereas $S(\mathbf{x}, \mathbf{x}_i)$ is the trilinear interpolation function that computes the Euler field properties at $\mathbf{x}$ from the Lagrangian quantities at $\mathbf{x}_i$.

The source terms due to the gas/solid interaction for the continuity equation, momentum equations, enthalpy equation, and species transport equations are computed similarly,

$$S_{m,g} = -\frac{1}{V_\Omega} \sum_{i=1}^{N_p} n_i \dot{m}_i S(\mathbf{x}, \mathbf{x}_i), \qquad \mathbf{S}_{u,g} = -\frac{1}{V_\Omega} \sum_{i=1}^{N_p} n_i \mathbf{f}_i S(\mathbf{x}, \mathbf{x}_i),$$

$$S_{h,g} = -\frac{1}{V_\Omega} \sum_{i=1}^{N_p} n_i q_i S(\mathbf{x}, \mathbf{x}_i), \qquad S_{Y_{g,k}} = -\frac{1}{V_\Omega} \sum_{i=1}^{N_p} n_i \dot{m}_{i,k} S(\mathbf{x}, \mathbf{x}_i), \tag{3.59}$$

where q_i is the heat exchange rate from solid particle, $\mathbf{f}_i = \mathbf{f}_{d,i} + \mathbf{f}_{\nabla_p,i}$ is the sum of the drag force and the pressure gradient force, and $\dot{m}_{i,k}$ is due to pyrolysis and char reactions.
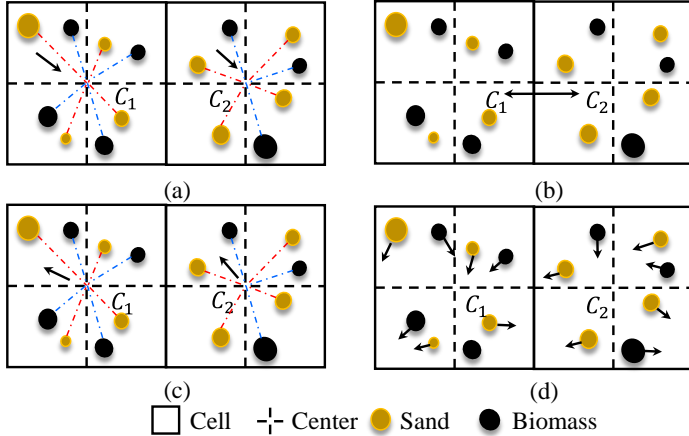
Figure 3.1: Diagram of solution procedure MP-PIC.

Fig. 3.1 shows the solution procedure of the MP-PIC model. In this figure, C_1 and C_2 are the Euler cell centers. Black and yellow particles denote the biomass

and sand particles, respectively. The solution procedure involves the following four steps (the order of steps is not the order of execution in the CFD code):

1. As shown in Fig. 3.1(a), the Euler field quantities in cell C_1 and C_2, e.g., the solid volume fraction and the source terms of the gas phase equations due to the particles, are computed from the Lagrangian particles in the cells.

2. As shown in Fig. 3.1(b), the gas phase transport equations are numerically solved using the finite-volume method described in Section 3.3.1.

3. As shown in Fig. 3.1(c), the Euler field quantities in cell C_1 and C_2, e.g., $\mathbf{u}_g^{n+1}$, is interpolated to the position of the i-th Lagrangian particles, i.e., to compute $\mathbf{u}_{g,i}^{n+1}$ in Eq. (3.57).

4. As shown in Fig. 3.1(d), the properties of the Lagrangian particles are computed by temporal integration of the particle phase equations, using the method described earlier.

In the CGM-PCM approach, a large number of parcels in a small cell contribute to large source terms, and local overloading of solids, i.e., the solid volume fraction (θ_s) is larger than the physically allowable value, e.g., $\theta_s > 0.62$ [112, 127]. Since $\alpha_g = 1 - \theta_s$, a large θ_s leads to a small α_g. Too large source terms and too small α_g can result in numerical instability of the gas phase governing equations. Thus, a threshold in the CFD solver is often employed, e.g., when $\theta_s > 0.62$, θ_s is set to the value of 0.62. The use of such a threshold can result in mass loss of the solid phase in the gas-phase governing equations in PCM (due to the increased α_g). Hence, a distribution kernel method (DKM) is developed to address this issue, as well as the cell searching strategy and parallel computation method for the DKM. A detailed description of the DKM model is given in the following chapter.
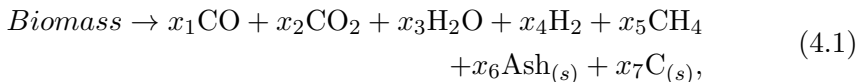
Chapter 4

Distribution kernel method for reactive dense particle-gas flow

In this chapter, the three-dimensional multi-phase particle-in-cell (MP-PIC) model presented in the previous chapters is applied to simulate biomass combustion and gasification in fluidized bed reactors. The MP-PIC model is coupled with a coarse grain method (CGM) which clusters fuel and sand particles into so-called parcels. CGM is computationally efficient; however, it can cause numerical instability if the clustered parcels pass through small computational cells, resulting in solid overloading in computational cells. To address this problem, a distribution kernel method (DKM) is proposed and implemented in an open-source CFD code, OpenFOAM v6. In the DKM, a redistribution procedure is employed to spread the solid volume and source terms of parcels to the surrounding domain. The numerical stiffness problem caused by the CGM can be remedied by this method. The DKM model is validated with experimental results from two lab-scale reactors. The model is able to capture the transient heat transfer process in a lab-scale bubbling fluidized bed (BFB) reactor under varying superficial velocities and sand loads. Then, the model is employed to study the combustion/gasification process in the other BFB reactor under varying ambient temperatures, equivalent air ratios, and steam-to-biomass ratios. The DKM is shown to improve the accuracy and robustness of the model.

4.1 Methodology

The governing equations of the continuous and discrete phases are described in the Euler-Lagrange framework. The interactions between the discrete and continuous phases are modeled using the mass, momentum, and energy source terms. Details of the gas-solid governing equations are presented in Section 3.1 of Chapter 3. Here, a brief summary of the used models is presented. Reynolds averaged Navier–Stokes (RANS) turbulence closure is employed in the gas-phase governing equations. A Partially Stirred Reactor (PaSR) model is used to account for turbulence chemistry interaction when computing the source terms due to gas phase chemical reactions. The standard k-ε model is used to determine the eddy viscosity. Details of the particle models are presented in Section 3.2 of Chapter 3. Two types of particles, i.e., biomass and sand, exist in the solid phase system. A thermochemical biomass particle undergoes a series of conversion processes: initially drying and devolatilization, subsequently oxidation of volatile and char, and finally, char heterogeneous reaction by reacting with oxygen/steam/carbon dioxide while sand particles are assumed to be chemically inert. The mass conversion rate of biomass particles considered here is the sum of evaporation, devolatilization, and char conversion rates. The forces acting on the individual biomass and sand particles include drag, gravity, pressure gradient, and interparticle stress. The Wen-Yu drag model is used to model the drag force. The MP-PIC method is employed to model the interparticle stress. The heat transfer of individual particles includes convection, radiation, latent heat, pyrolysis heat, and char reactions heat. The P-1 model is employed in the radiation model. The coarse grain method (CGM) is used to reduce the computational cost. More details are presented in Chapter 3.

The pyrolysis product consists of heavy hydrocarbon species (such as tar), light hydrocarbon species (such as methane), water, carbon monoxide, carbon dioxide, etc. Pyrolysis models including detailed tar species have been reported (e.g., [198]). The aim of this Chapter is to develop a robust MP-PIC model that can be used to study a wide range of particle loads. Hence, a one-step pyrolysis model and a simplified homogeneous volatile gas and heterogeneous char reaction mechanism are employed in this Chapter, following the literature [58, 59, 103, 134, 146, 194, 199–201]. However, more advanced and complex chemical kinetic models (e.g., including tar chemistry) [198, 202, 203] can be employed in the developed model framework. The one-step pyrolysis reaction model is

$$Biomass \rightarrow x_1 CO + x_2 CO_2 + x_3 H_2O + x_4 H_2 + x_5 CH_4$$
$$+ x_6 Ash_{(s)} + x_7 C_{(s)}, \tag{4.1}$$

where x_j are the stoichiometric constants. The constants are taken from [103,

168], $x_1 = 0.331$, $x_2 = 0.257$, $x_3 = 0.056$, $x_4 = 0.032$, $x_5 = 0.074$, $x_6 = 0.204$, and $x_7 = 0.046$. $\text{Ash}_{(s)}$ and $\text{C}_{(s)}$ denote respectively ash and char in the solid phase.

As discussed in Section 2.6.2 of Chapter 2, heterogeneous reactions of char with the surrounding gas species (such as O_2, CO_2, H_2O) are complex processes, involving char-O_2, char-CO_2, and char-H_2O reactions. Here, a global reaction model is employed for char reaction, see Table 4.1. High molecular weight hydrocarbons (tar) are treated as unstable products and reactions with sulfur and nitrogen are not taken into account [58, 199]. Table 4.1 lists the homogeneous and heterogeneous reactions considered, where the chemical kinetic rate constants are taken from the literature [146, 194, 199, 204].

Table 4.1: Homogeneous and heterogeneous reactions considered in biomass combustion and gasification. Note: $\text{C}_{(s)}$ is solid phase char. C_k represents the molar concentration of gas species k.

Reference	Homogeneous reactions	Kinetic rate [Kmol/m³/s]
R1 [194, 199]	$CH_4 + H_2O \rightarrow CO + 3H_2$	$R_1 = 0.312 exp(-15,098/T_g)C_{CH_4}C_{H_2O}$
R2 [194, 199]	$CO + H_2O \rightarrow CO_2 + H_2$	$R_2 = 2.5 \times 10^8 exp(-16,597/T_g)C_{CO}C_{H_2O}$
R3 [194, 199]	$CO_2 + H_2 \rightarrow CO + H_2O$	$R_3 = 9.43 \times 10^9 exp(-20,563/T_g)C_{CO_2}C_{H_2}$
R4 [194, 199]	$CH_4 + 2O_2 \rightarrow CO_2 + 2H_2O$	$R_4 = 2.119 \times 10^{11} exp(-24,379/T_g)C_{CH_4}^{0.2}C_{O_2}^{1.3}$
R5 [194, 199]	$CO + 0.5O_2 \rightarrow CO_2$	$R_5 = 1.0 \times 10^{10} exp(-15,154/T_g)C_{CO}C_{O_2}^{0.5}C_{H_2O}^{0.5}$
R6 [194, 199]	$H_2 + 0.5O_2 \rightarrow H_2O$	$R_6 = 2.2 \times 10^9 exp(-13,109/T_g)C_{H_2}C_{O_2}$

Reference	Heterogeneous reactions	Kinetic rate [s/m]
R7 [146, 204]	$C_{(s)} + 0.5O_2 \rightarrow CO$	$R_7 = 0.046 \times 10^7 exp(-13,523/(R_u T_i))$
R8 [146, 204]	$C_{(s)} + H_2O \rightarrow CO + H_2$	$R_8 = 1.71 \times 10^7 exp(-211,000/(R_u T_i))$
R9 [146, 204]	$C_{(s)} + CO_2 \rightarrow 2CO$	$R_9 = 9.1 \times 10^6 exp(-166,00/(R_u T_i))$

4.1.1 Distribution kernel model

To address the overloading issue, a new method, the so-called distribution kernel method (DKM) is proposed. It gives the advantage of easy implementation and low computational cost. As shown in Fig. 4.1, the parcels in a computational cell (marked as cell-o) with PCM are clusters of sand and biomass particles from the surrounding domain (marked as a circular region). To avoid numerical instability caused by locally too many particles in cell-o, DKM re-distributed the particles and the associated source terms in the parcels of cell-o to the surrounding domain from which the particles are clustered. The redistribution algorithm is constructed in such a way that the solid phase volume and source terms are conserved before and after distribution.

A filtering kernel function $g(\mathbf{x}, t)$, which is defined based on the distance of the

PCM   DKM

• Particle   ● Parcel $\boxed{o}$ Scoping Cell o $\overset{..}{()}$d Distribution Radius
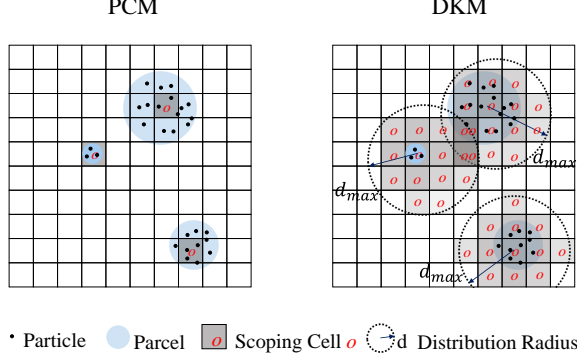
Figure 4.1: Schematic illustration of PCM and DKM.

surrounding cells to cell-o, is employed in the present work. The integration of the kernel function over the entire given physical space is unity. Similar strategies were used by Jesse et al. [205], Wang et al. [169], Sun et al. [112], and Zhang et al. [114]. The surrounding cells of a local cell can be located by a new grid search algorithm based on a given distance d_{max}, as used in the present work.

The total volume of solid phase V_s in a given domain Ω is calculated by

$$V_s = \int_{\Omega} \theta_0(\mathbf{x}, t) dV, \tag{4.2}$$

where $\theta_0(\mathbf{x}, t)$ is the solid volume fraction before redistribution. V_s must be the same before and after redistribution,

$$V_s = \int_{\Omega} \theta_0(\mathbf{x}, t) dV \equiv \int_{\Omega} \theta(\mathbf{x}, t) dV = \int_{\Omega} g(\mathbf{x}, t) V_s dV, \tag{4.3}$$

which leads to

$$\theta(\mathbf{x}, t) = g(\mathbf{x}, t) V_s = g(\mathbf{x}, t) \int_{\Omega} \theta_0(\mathbf{x}, t) dV, \tag{4.4}$$

where $\theta(\mathbf{x}, t)$ is the solid volume fraction after redistribution. A simple redistribution function $g'(\mathbf{x}, t)$ is employed,

$$g'(\mathbf{x}, t) = (1 - \frac{|\mathbf{x} - \mathbf{x}_0|}{d_{max}})^2, \tag{4.5}$$

where $\mathbf{x}_0$ is the position vertor of the centroid of cell-o. d_{max} is a prescribed distance within which solid phase volume and source terms will be redistributed.

The function $g'(\mathbf{x}, t)$ may not satisfy Eq. (4.3). By normalization of $g'(\mathbf{x}, t)$, the filtering kernel function $g(\mathbf{x}, t)$ can be obtained from $g'(\mathbf{x}, t)$,

$$g(\mathbf{x}, t) = g'(\mathbf{x}, t) / \int_\Omega g'(\mathbf{x}, t) dV, \tag{4.6}$$

i.e.,

$$\int_\Omega g(\mathbf{x}, t) dV = 1. \tag{4.7}$$

$g(\mathbf{x}, t)$ can be used to redistribute the source term for the mass conservation equation,

$$S_m(\mathbf{x}, t) = g(\mathbf{x}, t) S_M = g(\mathbf{x}, t) \int_\Omega S_{m0}(\mathbf{x}, t) dV, \tag{4.8}$$

which is shown to satisfy mass conservation:

$$S_M = \int_\Omega S_{m0}(\mathbf{x}, t) dV \equiv \int_\Omega S_m(\mathbf{x}, t) dV = \int_\Omega S_M g(\mathbf{x}, t) dV, \tag{4.9}$$

where subscript "0" denotes quantities before redistribution. Similarly, the source terms for the momentum equations and the energy equation, and the species transport equations can be redistributed using $g(\mathbf{x}, t)$:

$$\mathbf{S}_u(\mathbf{x}, t) = g(\mathbf{x}, t) \int_\Omega \mathbf{S}_{u0}(\mathbf{x}, t) dV, \tag{4.10}$$

$$S_q(\mathbf{x}, t) = g(\mathbf{x}, t) \int_\Omega S_{q0}(\mathbf{x}, t) dV, \tag{4.11}$$

$$S_{Y_k}(\mathbf{x}, t) = g(\mathbf{x}, t) \int_\Omega S_{Y_k 0}(\mathbf{x}, t) dV. \tag{4.12}$$

4.1.2 Implementation of DKM and parallel computation

The MP-PIC and DKM model are implemented in an open-source CFD code, OpenFOAM v6 [186], based on coalChemistryFoam. More information about the numerical scheme is referred to Section 3.3. The MP-PIC model is adopted in coalCloud for the discrete phase while the solid/gas interaction is taken into account through the source terms in the governing equations of the continuous phase.

In the DKM, the surrounding cells within a certain distance to cell-o, d_{max}, are selected for redistribution operations. The cell that is partly located within
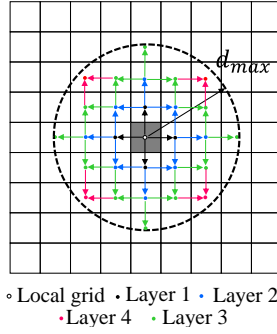
Figure 4.2: Cell searching strategy employed in the DKM model.

the sphere of d_{max} is considered to be in the domain of distribution if the distance between the center of the given cell to the center of cell-o is less than or equal to d_{max}. An efficient cell search algorithm is needed since the computational cost would increase hugely if all cells are looped during searching. Three search strategies, namely shared-point-based, shared-edge-based, and shared-face-based, are used in the present work. As an example, Fig. 4.2 presents a schematic diagram of the searching procedure of the shared-face-based method. First, the neighboring cells that share one of the faces pertaining to the local cell are selected, see the black arrow in Fig. 4.2. And then, the blue arrows represent the second layer, and the search continues until the given maximum distance d_{max}, as shown in Fig. 4.2, is reached for all the latest selected cells. After each search, the selected cells outside of the scope of d_{max} are removed. Note that, in a static mesh and a fixed d_{max}, the search of the neighboring cells is only needed to be performed once.

Since the searching strategy is cell-based without any specific direction, it works perfectly in the unstructured mesh. However, when the simulation domain is decomposed into several sub-domains in parallel computation, it is not straightforward to search the neighboring cells across sub-domains. Thus, the whole simulation domain is considered in the master processor and the communication between master and slave processors is achieved by the message-passing interface (MPI).

As an example, as shown in Fig. 4.3, the domain of redistribution involves four sub-domains in four slave processors. The DKM procedure is done as follows. First, cell searching is performed in the master processor. The solid volume and source terms in cell-o are transferred from slave processor 2 to the master processor. Then, the source terms of cell-o will be distributed to the cells within the sphere of diameter d_{max} in the master processor. Finally, the distributed
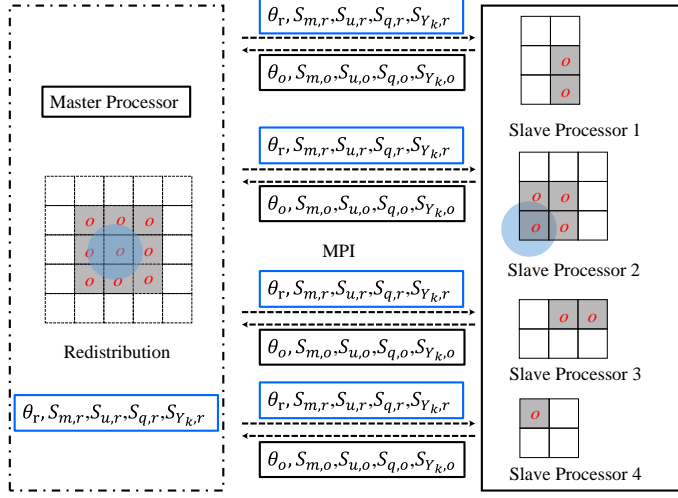
Figure 4.3: Schematic diagram employed in the DKM parallelization.

source terms are returned to the sub-domains in the slave processors from the master processor.

4.2   Case setup, initial and boundary conditions

Two lab-scale fluidized bed reactors are employed to evaluate the MP-PIC model based on the DKM and PCM. The geometries of the two reactors are shown in Fig. 4.4. The first reactor hereafter referred to as Case 1, is a bubbling fluidized bed (BFB) reactor where the heat transfer between hot sand particles and cold ambient gas was investigated experimentally [206]. This case is to evaluate the heat transfer model and the performance of DKM and PCM. The second reactor hereafter referred to as Case 2, is based on the experiment of biomass combustion and gasification in a lab-scale bubbling fluidized bed furnace [207]. In the original experiment, the furnace has a cylindrical geometry with a 50 mm internal diameter and 1200 mm height. In a previous DEM simulation, the geometry was simplified to a cuboid with an equivalent cross-sectional area [146]. This simplified geometry is to investigate the biomass combustion model and the performance of DKM and PCM, allowing for direct comparison with the DEM results.
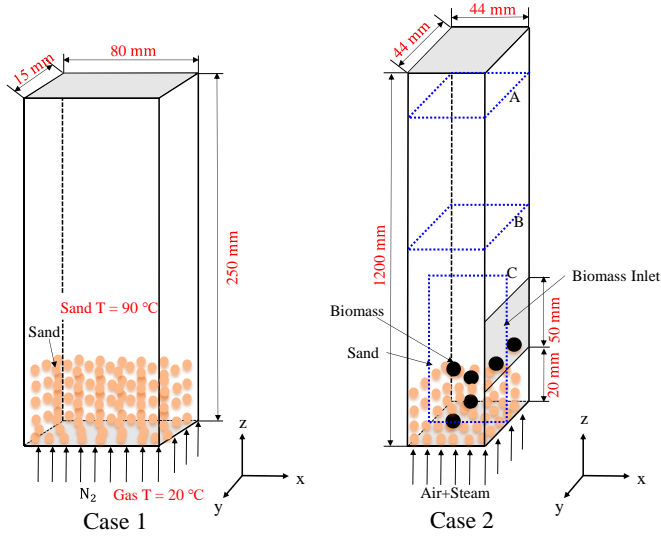
Figure 4.4: Schematic illustration of lab-scale bubbling fluidized bed reactors.

4.2.1 Heat transfer in lab-scale fluidized bed reactor

Particle dynamics and heat transfer in Case 1 are first investigated. The BFB reactor, as illustrated in Figure 4.4, has a depth of 15 mm, a width of 80 mm, and a height of 250 mm. The fluidization gas used in this Chapter is N_2 with a temperature of 20 °C. The gas is supplied from the bottom of the reactor with three different superficial velocities (U_{sup}). The initial filling of the reactor consists of hot sand particles with a uniform diameter of 1 mm and temperature of 90 °C. Table 4.2 shows the physical properties of the sand particles. Sand temperature (T_s) was measured for five operating conditions with a cold anodized aluminum background wall [206, 208]. The total mass of the sand, m_{sand}, was varied from 75 g to 125 g, and the superficial velocity U_{sup}, was varied from 1.33 m/s to 1.90 m/s. Table 4.3 lists the key parameters of the five experimental cases (Cases 1a – 1e) and three additional cases (Cases 1f - 1h) that are simulated to investigate the results with and without DKM.

The outlet boundary is located on the top plane of the reactor, see Fig. 4.4. Since the flow close to the outlet is rather uniform, a zero gradient of dependent variables has been used as the outlet boundary condition, referred to as the 'InletOutlet' boundary condition in OpenFoam. The wall boundary is assumed to be a non-slip and constant temperature of 20 ^{o}C (the same as the gas temperature). For all cases listed in Table 4.3, the simulations are carried out using

Table 4.2: Biomass and sand particle properties. *The biomass mass of 0.002 kg is the total mass of biomass injected within 20 seconds. The biomass is injected into the reactor at a rate of 10^{-4} kg/s.

Cases	particles	d_i [mm]	ρ_i [kg/m³]	$C_{p,i}$ [J/kg/K]	total mass* [kg]	T_i [°C]
Case 1 [206]	sand	1	2500	840	0.075 & 0.125	90
Case 2 [207]	biomass	$0.25 \sim 0.35$	750	1500	0.002	25
	sand	$0.25 \sim 0.7$	2300	840	1.25	$750 \sim 850$

a uniform mesh with a cell size of 2.28 mm and a total number of mesh cells of 23,100. The number of sand parcels is 25,024. The mesh size and parcel number are chosen based on the DEM work of Patil et al. [206]. In the MP-PIC or DEM simulations, the mesh size must be sufficiently larger than the diameter of the particles (without CGM) or the parcels (with CGM). A cell-to-parcel size ratio $\alpha_{c/p}$ is introduced to quantify the relationship between the mesh size and the size of the parcels. $\alpha_{c/p}$ is defined as the cube root of the cell volume (V_c) divided by the particle/parcel diameter, i.e., $\alpha_{c/p} = \sqrt[3]{V_c}/d_p$, where d_p is the diameter of the particle (without CGM) or the equivalent diameter of the parcel (with CGM). In the CGM, a coarse grain ratio (γ) is introduced and is defined as the cube root of the number of particles inside a parcel $N_{p/p}$, i.e., $\gamma = \sqrt[3]{N_{p/p}}$.

Numerical instability may arise if $\alpha_{c/p}$ is small [113]. Different values of $\alpha_{c/p}$ have been used in the literature, e.g., 2.5 [100], $1 \sim 4$ [169], 1.58 [209], and stable numerical results were obtained. These values could be difficult to achieve in large-scale furnaces with complex geometry since certain small-size cells are needed to discretize the geometry and the system involves quadrillion or more particles, which are clustered into millions of parcels, i.e., in each parcel, there might be millions of sand and biomass particles or more. In Case 1, the ratio of the present cell size to the diameter of parcel $\alpha_{c/p}$ is 1.73, which was selected following the suggestion of a previous work [206]. A value of $1\sim 2$ for γ was used in Qi et al. [103] and 1.44 was employed in Lichtenegger and Miethlinger et al. [209]. For Case 1a–1e, γ is 1.32 – 1.56, and in each parcel the number of particles is on average about $2\sim 4$. For Cases 1g and 1h, higher values of γ are tested to evaluate the performance of DKM at higher solid phase loads.

4.2.2 Combustion and gasification in lab-scale fluidized bed reactor

In Case 2 combustion and gasification of rice husk in a lab-scale bubbling fluidized bed reactor were investigated. As shown in Fig.4.4, the biomass inlet has a length of 44 mm and height of 50 mm and is located at a height of 20 mm above

Table 4.3: Key parameters and run-cases for the BFB reactor Case 1. The parcel number N_{parcel} is 25024.

Cases	1a	1b	1c	1d	1e	1f	1g	1h
U_{sup} [m/s]	1.33	1.71	1.90	1.33	1.71	1.33	1.33	1.33
m_{sand} [kg]	0.075	0.075	0.075	0.125	0.125	0.100	0.150	0.175
$N_{particle}$ [-]	57,324	57,324	57,324	95,541	95,541	76,433	114,649	133,758
γ [-]	1.32	1.31	1.32	1.56	1.56	1.45	1.66	1.75
$\alpha_{c/p}$ [-]	1.73	1.73	1.73	1.46	1.46	1.57	1.37	1.30

Note: $N_{particle}$ is the real number of particles without CGM.

the bottom of the reactor. The mixture of air and steam enters the fluidized bed from the bottom of the reactor and biomass is fed into the reactor at a rate of $1 \cdot 10^{-4}$ kg/s via a screw feeder. Yields of gaseous products were measured at the reactor outlet by Loha et al. [200, 207]. Seven cases were measured (and simulated here) by varying operating conditions, e.g., 1) the equivalent air ratio (EAR), which is the ratio of the mass of air to that of dry biomass divided by the stoichiometric ratio of the mass of air to that of dry biomass, 2) the steam-to-biomass ratio SR, which is the ratio of the mass of steam to the mass of dry biomass, and 3) the reactor operation temperature T_r. An electric heater heats the furnace and the desired temperature is set through a PID controller [207]. The initial temperature of walls, sand, and gas in the entire domain is set to be the same as the reactor temperature. Air and steam flowing into the fluidized bed are preheated to 200 °C, respectively. The EAR is varied from 0.3 to 0.4, the SR is varied from 0.2 to 0.8, and the T_r is varied from 750 °C to 850 °C. Table 4.4 shows the key parameters of the seven cases. Similar to Case 1, zero gradient boundary condition has been used at the outlet boundary of Case 2 (the top plane of the reactor, Fig. 4.4), while the wall is assumed to be non-slip with a constant temperature of T_r.

Table 4.4: Key parameters studied in Case 2, with different equivalent air ratio (EAR), steam to biomass ratio (SR), and reactor operation temperature (T_r).

Cases	2a	2b	2c	2d	2e	2f	2g
EAR [-]	0.30	0.35	0.40	0.35	0.35	0.35	0.35
SR [-]	0.5	0.5	0.5	0.2	0.8	0.5	0.5
T_r [°C]	800	800	800	800	800	750	850

Table 4.5: Mesh sensitivity study for Case 2b and key parameters. The coarse grain ratio γ is calculated based on the mean diameter of particles in the parcel. N_{parcel} for biomass is the total number of parcels injected within 20 seconds. Note: S and B denote respectively sand and biomass.

Cases	Cell size [mm]	N_{parcel} (S & B)	$\alpha_{c/p}$ (S & B)	γ (S & B)
Coarse mesh	5.5	50,000 & 10,000	2.00 & 6.89	5.49 & 2.66
Medium mesh	4.4	100,000 & 20,000	2.01 & 6.94	4.36 & 2.11
Fine mesh	2.9	300,000 & 60,000	1.92 & 6.60	3.02 & 1.46

Table 4.6: Biomass properties in Case 2 [207]

Ultimate analysis	[wt%]	C	H	O	N	S	Ash
		38.43	2.97	36.36	0.07	0.49	21.68

Proximate analysis	[wt%]	Volatile	Fixed Carbon	Moisture	Ash
		55.54	14.99	9.95	19.52

Rectangular uniform mesh is used in the simulation of Case 2. In order to evaluate the sensitivity of the results to the mesh resolution, Case 2b was simulated using three different meshes resolutions, see Table 4.5. The coarse mesh has a cell size of 5.5 mm, and a coarse grain ratio γ of 5.49 for sand parcels and 2.66 for biomass parcels, based on the mean diameters given in Table 4.2. The medium mesh has a cell size of 4.4 mm, and a coarse grain ratio γ of 4.36 and 2.11 for sand and biomass parcels, respectively. The fine mesh has a cell size of 2.9 mm, and a coarse grain ratio γ of 3.02 and 1.46 for sand and biomass parcels, respectively. The number of parcels was selected in such a way that the cell-to-parcel size ratio $\alpha_{c/p}$ is kept nearly constant for the three meshes, i.e., about 2 for sand parcels and 6.66 – 6.99 for biomass parcels. As a result, the coarse mesh contains 13,504 cells, with 50,000 sand parcels and 10,000 biomass parcels; the medium mesh contains 26,400 cells, with 100,000 sand parcels and 20,000 biomass parcels; the fine mesh contains 78,300 cells, with 300,000 sand parcels and 60,000 biomass parcels. Other detailed properties of biomass and sand are shown in Tables 4.2 and 4.6. The Rosin-Rammler distribution function is employed to model the distribution of particle size. Biomass particle density is assumed to be constant during the conversion process, while the size of the particles decreases during the process. The biomass parcels are injected into the furnace after the sand parcel reaches steady fluidization.

4.3 Results and discussion

4.3.1 Heat transfer in lab-scale fluidized bed reactor
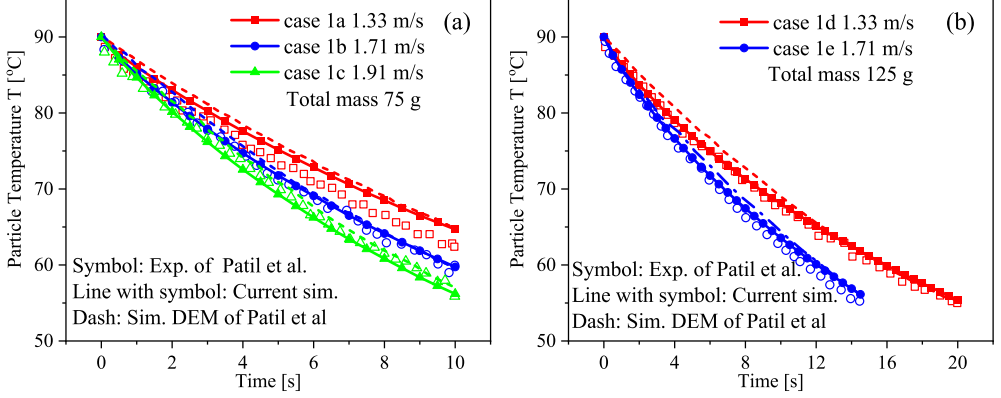
Figure 4.5: Comparison of mean particle temperature between the present simulations using the PCM (solid lines), and previous simulations using the DEM approach (dashed lines) [206], as well as with experiments (circles) [208] for the five cases (Cases 1a − 1e) with the total sand mass of 75 g (a) and 125 g (b) and various N_2 flow superficial velocity.

The results of Case 1, which are described in Table 4.3, are presented in Fig. 4.5. This figure compares the results of the MP-PIC model with PCM to the results of a previous work [206] using a more costly DEM approach and to the experimental measurements [208] for the five cases 1a–1e. As shown in Fig. 4.5, the present PCM results agree very well with the DEM results and the experiments, with a maximum error of (in comparison with experiments) less than 5% at $t = 10$ s, which occurs for Case 1a ($U_{sup} = 1.33$ m/s, $m_{sand} = 75$ g). The convective and radiative heat transfer between the solid particles and the ambient gas, radiative heat transfer between particles, and the conductive heat transfer between particles and walls are taken into account in the heat transfer mechanisms of the model (Eq. 3.49). The mean particle temperature decreases faster as the superficial velocity U_{sup} increases and the slope dT_i/dt decreases over time. Higher U_{sup} leads to higher gas phase mass flux and enhanced mixing of sand and the cold N_2 gas, and as a result, a faster decrease of the mean particle temperature. The last three terms on the right-hand side of Eq. (3.49) are zero since the sand particles are chemically inert. The temperature difference $T_g - T_i$ decreases with time, resulting in a decreasing slope of particle temperature since the convective heat transfer plays a dominant role. dT_i/dt is approximately proportional to $T_g - T_i$, as described in Eq. (3.49). Due to the low operating temperature in Case 1 ($\leq 90^o$C), radiative heat transfer plays an insignificant

role and the particle temperature predicted with radiative heat transfer is nearly identical to that without it.
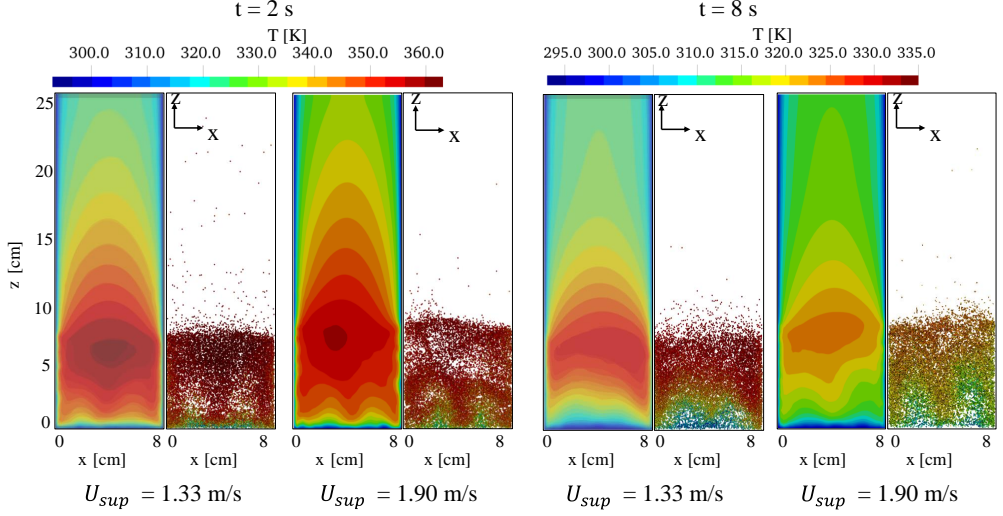
Figure 4.6: Gas temperature, sand particle temperature, and distribution of sand parcels with PCM at 2s and 8s of Case 1a and Case 1c

The temperature distributions for gas and particles for two different U_{sup} with the m_{sand} of 75 g are shown in Fig. 4.6. At the start of the process, $t = 2$ s, a temperature gradient near the bottom of the reactor and near the walls is high, resulting in a high temperature on the top of the bed. At a later time, $t = 8$ s, the sand particles tend to gather near the wall due to the impact of the gas-solid interactions and particle-particle collision, which drive the parcels to flow towards the wall and then descend along the wall. As a result, the high-temperature particles near the wall raise the gas temperature near the wall.

As previously stated in section 4.1.2, DKM is proposed to handle the situation when the fluidized bed is under overloading conditions. To showcase the performance of DKM under overloading conditions, the results from the MP-PIC model using both PCM and DKM are compared. Fig. 4.7 shows the temporal evolution of the mean particle temperature in Case 1, in which the superficial velocity is $U_{sup} = 1.33$ m/s and the mass of sand particles ranges from 75 g to 175 g. The simulations are based on the number of parcels and meshes of Case 1 as listed in Table 4.3 (Cases 1a, 1d, 1f – 1h). As the mass of sand increases, the carrier load $1/\alpha_{c/p}$ varies from 0.58 – 0.77. PCM suffers from numerical
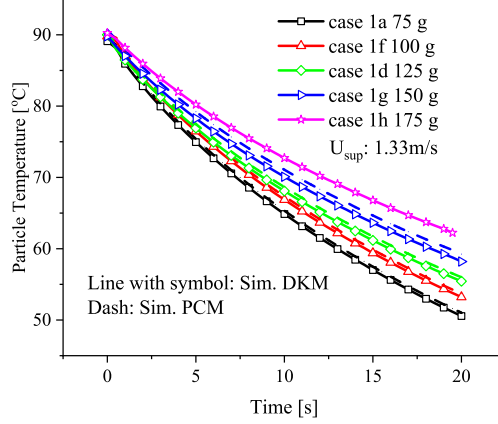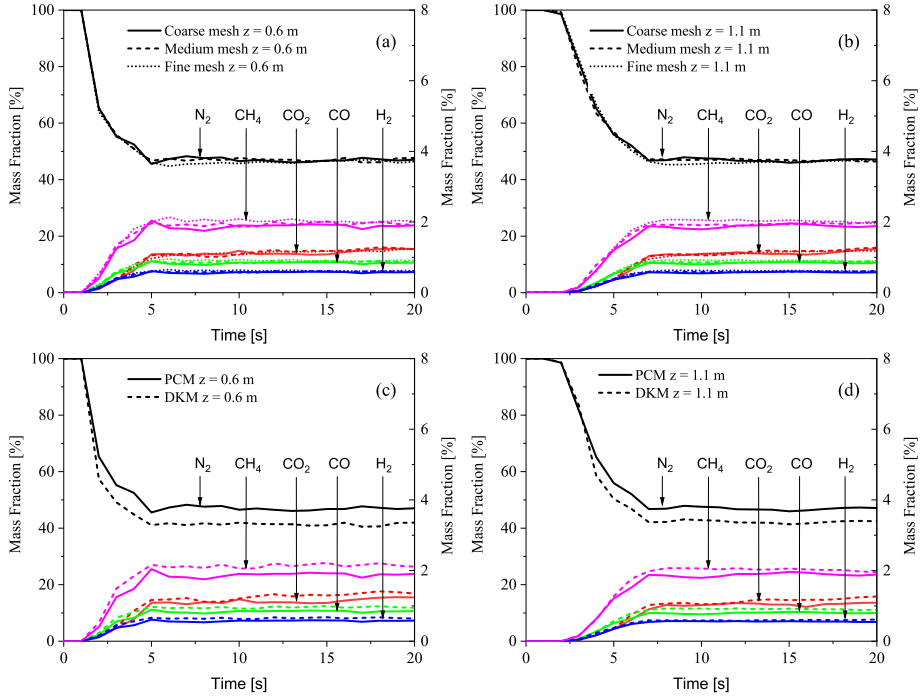
Figure 4.7: Temporal evolution of particle temperature in Case 1. Comparison between PCM and DKM with different carrier loads.

instability and no results could be obtained When the mass of sand is increased to 175 g (Case 1h). The results indicate that PCM can predict the transient heat transfer process up to $m_{sand} \leq 150$ g. DKM can very well predict the transient heat transfer process at this high load condition. Fig. 4.7 shows that when both PCM and DKM are applicable, the results from the two methods agree with each other very well.

4.3.2 Combustion and gasification in lab-scale fluidized bed reactor

The results from the numerical simulations using the MP-PIC model for the lab-scale bubbling fluidized bed, Case 2 in Table 4.4, are presented here. Initially, the reactor is filled with sand particles up to a height of $z = 0.1$ m, and after reaching steady operation, the height of the bubbling fluidized bed reaches about 0.22 m [200]. The biomass combustion/gasification process occurs mainly in the lower 0.5 m of the reactor. Fig. 4.8 shows the temporal evolution of mean mass fractions of N_2, CO_2, CO, H_2, and CH_4 averaged over cross-section planes at two different heights of the reactor ($z = 0.6$ m and $z = 1.1$ m) for Case 2b, simulated using PCM with three different mesh resolutions (Fig. 4.8a–b), and the PCM and DKM approach with the medium mesh (Fig. 4.8c–d). The two sampling cross-sections are indicated in Fig. 4.4 as planes A and B. In the initial transient stage, the biomass particles undergo heating, pyrolysis, partial oxidation, and gasification, during which the mass fractions of gaseous products (CO_2, CO, H_2, and CH_4) increase while the mass fraction of inert gas N_2 decreases. After a

Figure 4.8: Temporal evolution of gas product mass fractions over time with different meshes and number of parcels taken from the cross sections at the height of (a, c) 0.6 m and (b, d) 1.1 m for Case 2b. Values of N_2, CO_2, and CO mass fractions are shown on the left vertical axis while H_2 and CH_4 on the right vertical axis. The results are from the MP-PIC model with PCM and three different meshes (a, b) and from the MP-PIC model with PCM and DKM using the medium mesh (c,d).

short time, the reactor reaches steady operation. For the data sampled at the of plane $z = 0.6$ m, steady results are reached at 5 s, while at the $z = 1.1$ m plane, steady results are reached after 7 s. It is clear that the results from the three meshes agree very well with each other; the results from PCM and DKM agree also well during both the transient stage and the steady operation stage. The difference between the results from the different meshes is smaller than that from PCM and DKM. Based on the convergence behavior of the results from three different meshes, the medium mesh was employed in the simulations of cases 2a – 2g.

Fig. 4.9 shows the distribution of sand particles and sand temperature in a 3D domain of the lower 200 mm region of the reactor. The biomass inlet is located on the right side of the domain, ranging from 20 mm to 70 mm. Due to the heat exchange with cold biomass particles, the temperature of sand particles is lower in the region where biomass particles are mixed with sand particles. Initially, the biomass particles flow upwards along with sand particles near the right side

wall (0.9 – 1 s). When the biomass parcels are injected into the reactor, a small gas bubble forms around the biomass inlet. The biomass particles are squeezed into the near-wall zone by the sand particles due to the lower momentum of the biomass particles than the sand particles. Particles with low density and small size tend to move toward the edge of the bubble and the upper part of the bed as a result of the particle-particle collision and the gas-solid interactions.
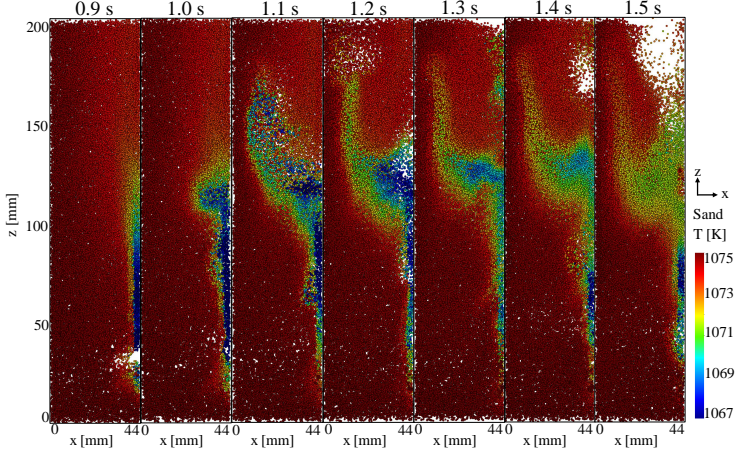
Figure 4.9: Distribution of sand particles and sand temperature of Case 2b during the initial development stage of the reactor, simulated using MP-PIC with PCM.

At $t = 1$ s, the biomass particles start to spread into the center of the reactor due to the particle/particle collision. As the biomass particles move near the wall, the drag force becomes smaller due to the lower carrier velocity $\mathbf{u}_g$. In addition to the drag force, the motion of the particles is driven by the gravity $\mathbf{g}$ and pressure gradient ∇p (Eq. 3.31). The particles descend along the wall until collision force from other particles and higher pressure from the bottom of the bed becomes dominant. Then, the particles can escape the near-wall zone and move to the full fluidization region. From $t = 1.1 – 1.5$ s, the biomass particles appear to interact with the sand particles and the surrounding gas only in the bottom 200 mm region of the reactor. Certain gas bubbles (regions without any particles) can be found at $t = 1.4 – 1.5$ s (in the upper right corner of the domain in Fig. 4.9).

Fig. 4.10 shows the distribution of gas temperature and mass fractions of key species at $t = 20$ s in a cross-section plane near the biomass inlet. The shown cross-section is in the middle plane of the reactor, in a region from the bottom of the reactor to a height of 200 mm. The region is marked as C in Fig. 4.4, where the biomass inlet on the right side of the domain is also indicated. The
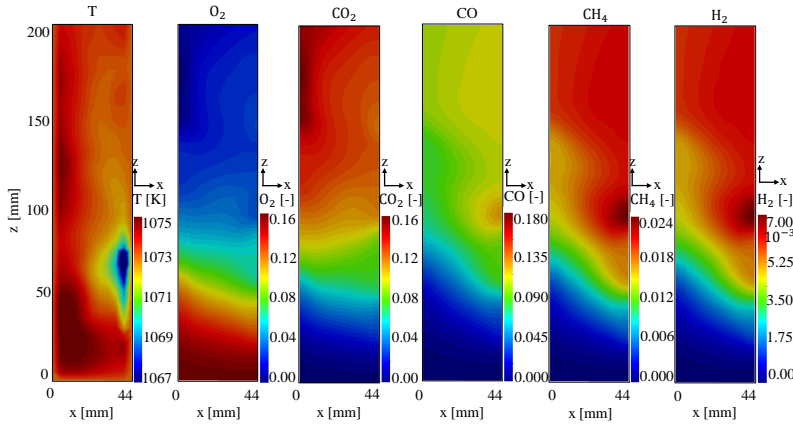
Figure 4.10: Distribution of gas temperature, and mass fractions of O_2, CO_2, CO, H_2, and CH_4 in Case 2b at 20 s, simulated using MP-PIC with PCM.

gas temperature is rather uniform, with a slightly low temperature in the region near the biomass inlet, which corresponds to the cooling by the cold biomass particles. Oxygen is shown to be consumed quickly in the lower region of the bed, by reacting with volatile gases CO, CH_4, and H_2, forming CO_2. Higher mass fractions of CO, CH_4, and H_2 can be seen on the right side of the reactor, above the biomass inlet, indicating the region where the pyrolysis and gasification reactions take place.

In the present bubbling fluidized bed reactor, the biomass particles constitute only 0.16% of the total mass of the solid phase over the 20 seconds period of operation (see Table 4.2). As a result, the heat release/loss through combustion, pyrolysis, and gasification has a relatively insignificant impact on the particle temperature and gas temperature compared to convective and radiative heat transfer. This is the reason that the particle temperature and gas temperature are fairly homogeneous in space and nearly the same as that of the reactor operation temperature, see Figs. 4.9 and 4.10.

Fig. 4.11 compares the steady-state product gas mole fractions at the reactor outlet obtained from the simulations and experiments for the seven cases listed in Table 4.4. The effect of equivalent air ratio (EAR) on the product gas is shown in Figs. 4.11a and 4.11d. When EAR is increased from 0.3 to 0.4, the yields of H_2, CH_4, and CO decrease, while the yields of CO_2 and N_2 increase. This trend is shown in the experimental data and is supported by the model predictions, although the effect of EAR on the predicted results is relatively weaker. This trend can be explained by the combustion/gasification reaction
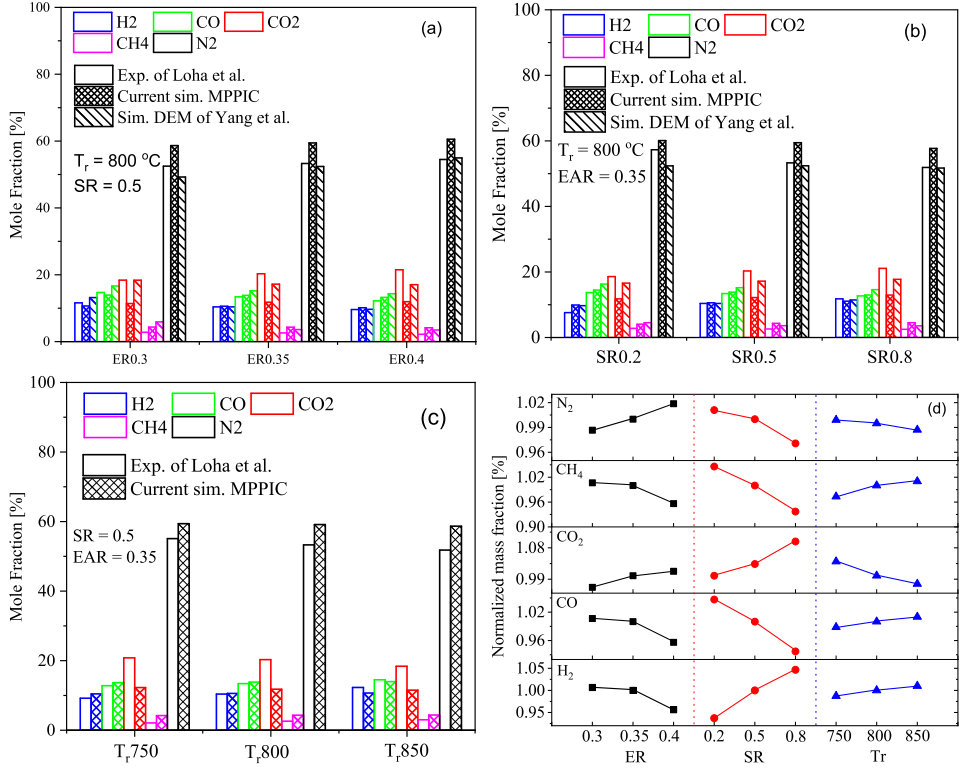
Figure 4.11: Comparison of the mole fractions of product gas between the MP-PIC/PCM simulations (pattern fill), the previous simulations using the DEM approach [146] (slash fill), as well as with experiments (blank fill) [207] for seven cases (Cases 2a - 2g) at different operation conditions: (a) SR 0.5, T_r 800 °C with various EAR: 0.30, 0.35, 0.40, (b) EAR 0.35, T_r 800 °C with various SR: 0.2, 0.5, 0.8, and (c) EAR 0.35, SR 0.50 with various T_r: 750 °C, 800 °C, 850 °C. In (d), the results from the MP-PIC/PCM simulations are re-plotted to show the trend of the product gas, where the gas mass fractions have been normalized by the corresponding results of Case 2b.

model shown in Table 4.1, which shows that an increase in the supply of air to the reactor (an increase in EAR) will enhance the oxidation of H_2, CH_4, and CO, resulting in an increasing CO_2 yield.

As shown in Figs. 4.11b and 4.11d, when SR increases, the yields of CH_4, CO and N_2 decrease, while the yields of H_2 and CO_2 increase. This is because the increased amount of steam in the reactor promotes the water-gas shift reaction (reaction R2), the gasification reaction with H_2O (reaction R8), and the methane/water reaction (reaction R1), see Table 4.1. It is observed that higher operation temperature T_r results in higher yields of H_2, CH_4, and CO, and lower yields of the CO_2 and N_2, see Figs. 4.11c and 4.11d. This can be attributed to the enhanced gasification/oxidation reactions of char, as shown in Table 4.1.

Apart from the comparison with the experimental measurements, the MP-PIC model results are compared with the DEM results of Yang et al. [146]. It is shown that the computational time required in the MP-PIC simulations is significantly shorter than that in the DEM simulations. With a similar number of mesh cells and processors (64 processors), the DEM simulation took 73 days to simulate a physical time of 20 seconds of the combustion/gasification process [146], whereas the present MP-PIC simulations took less than 2 days (with a Xeon E5-2698v3 Haswell 2.3 GHz CPU). Despite the significant reduction in computational cost, the MP-PIC model results agree very well with the experiments and the DEM results for most species, with the exception of CO_2 and N_2. Compared with the experimental results, the average relative error for H_2 and CO predicted from MP-PIC is 9.13% and 5.94%, respectively. The high relative error of CH_4 can be attributed to the simplified pyrolysis model and the absence of tar in the model [58] and the low concentration of CH_4 in the product gas.
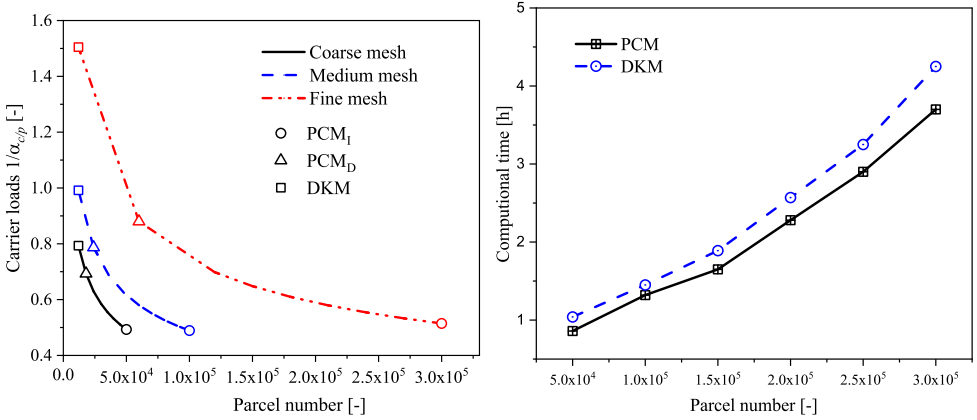

Figure 4.12: Carrier loads under which stable solution exists for Case 2b. The subscript "I" indicates the baseline setup given in Table 4.4; subscript "D" indicates the condition close to numerical instability. Lines with symbols in the right figure indicate the computational time required to simulate the combustion/gasification process for 1 second of physical time.

The results from PCM and DKM, as well as the numerical stability and computational cost of DKM and PCM, are evaluated under the EAR, SR, and T_r conditions of Case 2b. The number of parcels and mesh resolution is varied, with the number of biomass parcels being modified in proportion to the number of sand parcels (with the number of biomass parcels being 20% of that of the sand parcels). As shown in Fig. 4.12, the carrier load increases as the number of parcels decreases. The fine mesh has a higher carrier load for a given number of parcels. Each symbol denotes a simulation case that is numerically stable and has achieved a converged solution. For the PCM, the simulation case with

the highest carrier load that still performs a stable numerical solution is marked with triangles. The maximum carrier loads for the coarse, medium and fine meshes are 0.69, 0.79, and 0.88, respectively. A stable numerical solution can be obtained for the DKM even with much higher carrier loads. The medium mesh can handle carrier loads close to 1, and the fine mesh can allow for overloading parcels, e.g., with a carrier load of 1.5.

Physically, a carrier load close to 1 means that the cell is filled with solid particles, and a carrier load larger than 1 is not possible. However, numerically, this situation is unavoidable due to irregular small-size CFD cells in complex fluidized bed boiler geometries. In DKM, the contribution of local overloading to the solid volume and source terms are redistributed to the surrounding cells (Eqs. 4.8-4.12). Thus, the DKM offers a more robust method that allows for achieving numerical solutions with local carrier overloading. With the cell searching strategy shown in Fig. 4.2 and Fig. 4.3, the DKM is computationally efficient. The cases with different numbers of sand parcels are tested in parallel computation with 128-core to obtain results for a physical time of 1 s, and the running time of each case is shown in Fig. 4.12. The computational efficiency tends to decline as the number of parcels in the computational domain increases. The increase in computational time of DKM is within 20% of that for PCM.
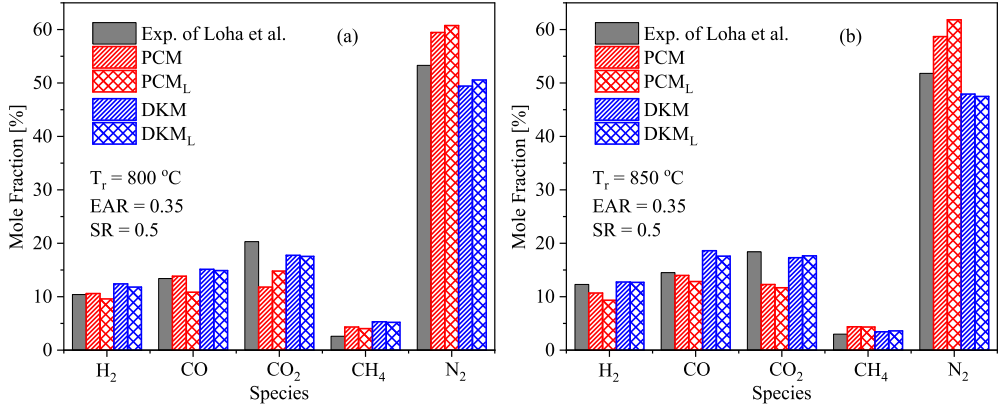
Figure 4.13: Mole fractions of product gases from experiments and numerical simulations using PCM and DKM for Case 2b with different parcel numbers.

Since the source term is redistributed in the DKM, the results from DKM and PCM could be different. Fig. 4.7 shows that, for Case 1, the difference between PCM and DKM results is noticeable but not significant. Fig. 4.13 shows the predicted product gas mole fractions for Case 2 with PCM and DKM based on the medium mesh. The results with 50,000 sand parcels (and 10,000 biomass parcels) are labeled as PCM_L and DKM_L, and the results with 100,000 sand

parcels (and 20,000 biomass parcels) are marked as PCM and DKM. As shown in Fig. 4.13, the DKM results are less sensitive to the number of parcels than the PCM results. The maximum relative error between PCM and PCM_L is 12.6%, while the DKM and DKM_L are less than 5.5%. The DKM results also agree better with the experiments than the PCM results, in particular for CO_2 and N_2.

The gas phase governing equations are invalid when the gas volume fraction is negative. The maximum load of solid in a CFD cell is thus limited. The theoretical maximum solid volume fraction of a sphere of diameter d_p in the cube of the side length of d_p is $\pi/6 \sim 0.52$. Considering the impact of the collision deformation, and the filling of the void by tiny size particles, the maximum solid volume fraction is about 0.62 [112, 200]. This is the maximum pack limit of particles in a cell. If the solid volume fraction exceeds the maximum pack limit, the results may become non-physical or numerical instability. In PCM, solid volume fraction is often set to the maximum pack limit if it is above the limit. This will result in a loss of solid mass. The finer the mesh, the worse the situation can become [114]. As shown in Fig. 4.13, the loss of biomass in the overloading cells gives rise to the under-prediction of CO_2 mass fraction from PCM as compared with the experiments, and the over-prediction of mass fraction of N_2. The DKM results are in better agreement due to source term redistribution that mitigates the loss of biomass in the overloading cells. For the same reason, biomass loss is likely the reason for the lower gas product mole fractions of H_2, CO, and CH_4 predicted by PCM, see Fig. 4.11.

The loss of solid mass in the PCM simulation due to local overloading is in-directly related to the "loss" of the solid volume fraction (θ), which is a result of the numerical implementation of the maximum pack limit. The mass of the solid phase that is solved in the discrete phase equation (3.17) is not affected by the loss of θ, since the maximum pack limit is applied to θ but not directly to the solid mass (m_i). For the same reason, the source terms (Eq. 3.59) of the gas phase governing equations are not affected explicitly. Instead, the source terms are reduced implicitly due to the change of gas volume fraction (α_g). From Eqs. (3.1,3.5) it appears that an increase of α_g is equivalent to a decrease of the source terms from solid biomass conversion. Since α_g increases when θ is decreased, the mass of gas produced from biomass conversion decreases.

To confirm the above discussion, the total mass of sand particles in the reactor of Case 2 is evaluated in two different ways. First, the total mass of sand (M_s)

is computed from the discrete phase,

$$M_s = \sum_{i=1}^{N_s} m_{s,i}$$

where N_s is the total number of sand parcels and $m_{s,i}$ is the mass of the i-th sand parcel. It is found that M_s is 1.25 kg, i.e., conserved in the process. Second, M_s is computed from the solid volume fraction

$$M_s = \rho_s \int_{\Omega} \theta(\mathbf{x}, t) dV$$

where ρ_s is the density of sand particles and Ω is the entire domain of the reactor. Since the mass of biomass is only 0.16% of the total mass of the solid phase within the 20 seconds of operation (see Table 4.2), it is expected that M_s computed from the second method should be only slightly higher than that from the first method, with an increase less than $0.0016(\rho_s/\rho_b)$, i.e., 0.49% (where ρ_b is the density of biomass particles). It is found that M_s from the PCM simulations of Case 2b (shown in Fig. 4.13) computed using the second method fluctuates in time around a mean value of 1.12 kg, which is about 10.4% reduction of the sand mass. DKM can significantly mitigate the loss of θ. For Case 2b, the DKM results show a loss of M_s by a mean value of 4%. The loss of θ in DKM is also due to the numerical implementation of the maximum pack limit. In the future study, the DKM redistribution scheme needs to be further improved to avoid local overloading to exceed the maximum pack limit.

4.4 Summary

In this Chapter, a three-dimensional MP-PIC model was developed for numerical simulation of heat transfer and biomass combustion/gasification process in fluidized bed reactors. The conventional MP-PIC method is based on the particle centroid method (PCM) and coarse grain method (CGM), which is computationally efficient but suffers from local overloading if the CFD cell is fine or if locally small-size cells are used. The latter is typically encountered in studies of fluidized bed furnaces with complex geometries. A distribution kernel method (DKM) is proposed to replace PCM, aiming to improve the accuracy and robustness of the method. The following conclusions are drawn:

- The DKM approach can effectively handle the overloading problem of PCM. It is shown that the PCM simulation becomes unstable if the carrier

load is high, while DKM can allow for a significantly higher carrier load without suffering from numerical instability. This enables the use of local small-size cells typically encountered in the simulation of fluidized bed boilers with complex geometries.

- For low carrier load conditions, e.g., Case 1 studied in this work, the DKM and PCM results agree with each other very well. At high carrier load conditions, e.g., Case 2 studied in this work, the DKM approach gives an improved prediction of the product gas yields from biomass combustion/gasification, compared with the PCM approach. It is found that the DKM results are less sensitive to the number of parcels than the PCM approach.

- The present MP-PIC/DKM approach can capture the transient heat transfer process and biomass combustion/gasification process of bubbling fluidized bed reactors. The DKM can be further improved by allowing for dynamic selection of the distance of the redistribution kernel.
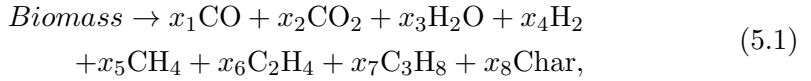
Chapter 5

An empirical model for biomass pyrolysis

In this chapter, the multi-phase particle-in-cell (MP-PIC) model coupled with the distribution kernel method (DKM), discussed in the previous chapter, is employed to investigate biomass gasification in two lab-scale fluidized bed gasifiers (FBGs). New development of a biomass pyrolysis model based on an empirical one-step mechanism is made to improve the prediction accuracy of gasification products. The simulation results are compared with those from the Particle Centroid Method (PCM) and experimental measurements. It is shown that the DKM can improve the robustness and mesh independence. The simulation results with the new pyrolysis model agree well with the experimental data under different gasification conditions. The new pyrolysis model is shown to improve the sensitivity of the yields of gasification products to operating temperature. The model is able to capture the trend of gas products with respect to variations in steam/biomass ratio (SR) and operating temperature (T_r). The mechanisms of the formation of gas products are analyzed based on the numerical results. By increasing the SR and T_r, the production of H_2 and CO_2 is shown to increase while the production of CO and CH_4 to decrease. It is shown that varying the steam/biomass ratio in the range of $0.8 \sim 2.0$ has a minor effect on the pyrolysis process and heterogeneous reactions while having a significant effect on homogeneous reactions, leading to changes in the final composition of the gas products. Varying the gasifier temperature T_r has on the other hand a crucial effect on the pyrolysis process, the gasification products, and carbon conversion.

5.1   Methodology

The governing equations of the continuous and discrete phases involved in fluid-ized bed gasifiers are described in Chapter 3, where details of turbulence closure, sub-models for heat/mass transfer between the gas and the particle phases, and MP-PIC/PCM models can be found. In the following, a detailed description of the new biomass pyrolysis model is presented. Since most FB simulations have been carried out using one-step models and the employed chemical rate constants vary significantly in the literature, it is important to develop a more robust one-step model that can be used to simulate biomass pyrolysis under a wider range of operating conditions. This has motivated the present work, in which a more consistent approach to determine the rate constants by enforcing element mass conservation law is proposed. A global reaction mechanism is considered for the pyrolysis of dry ash-free (DAF) biomass, where the formation of gaseous species, tar, and char is governed by the following reaction,

$$Biomass \rightarrow x_1\text{CO} + x_2\text{CO}_2 + x_3\text{H}_2\text{O} + x_4\text{H}_2$$
$$+x_5\text{CH}_4 + x_6\text{C}_2\text{H}_4 + x_7\text{C}_3\text{H}_8 + x_8\text{Char}, \tag{5.1}$$

where x_k are the stoichiometric coefficients of volatile and char. High molecular weight hydrocarbons (tar) are assumed to be cracked to lighter hydrocarbons in the form of C_2H_4 and C_3H_8 [210].

The stoichiometric coefficients x_k and the mass fractions of species k in the yield of the DAF biomass pyrolysis, $Y_{k,F}$, satisfy the following relation

$$x_k = (Y_{k,F}/M_k)\sum_i x_i M_i, \tag{5.2}$$

where M_k is the molar mass of species k, $k = \text{CO}, \text{CO}_2, \text{H}_2\text{O}, \text{H}_2, \text{CH}_4, \text{C}_2\text{H}_4$, C_3H_8, and char. In the present model, char is assumed to be pure carbon.

Assume that the element mass fractions of C, H, and O in the DAF biomass are respectively $\beta_{\text{C,F}}$, $\beta_{\text{H,F}}$ and $\beta_{\text{O,F}}$. Element mass conservation law suggests the following equations to be satisfied during the pyrolysis of biomass:

$$\beta_{\text{C,F}} = \sum_k \beta_{\text{C},k} Y_{k,F},$$
$$\beta_{\text{H,F}} = \sum_k \beta_{\text{H},k} Y_{k,F}, \tag{5.3}$$
$$\beta_{\text{O,F}} = \sum_k \beta_{\text{O},k} Y_{k,F},$$

where $\beta_{l,k}$ denotes the mass fraction of element l in species k.

It is shown that the model constants reported in the literature are not always consistent with the conservation law of element mass fractions of C, H, and O in the studied biomass. The model constants are often not reactor temperature dependent [67, 103, 168]. In the following, a method of computing the stoichiometric coefficients is described, accounting for the reactor temperature effect and the element mass conservation during the pyrolysis of biomass.

The operating temperature T_r has an important effect on the pyrolysis products. The stoichiometric coefficients of fixed values in pyrolysis reactions result in a low sensitivity of gasification products to T_r, which is in contrast to the experiment results. To alleviate this issue, an empirical model for the stoichiometric coefficients of biomass pyrolysis reaction is proposed in this Chapter. The model constants are derived from the mass conservation of elements C, H, and O and energy conservation during pyrolysis reactions. Similar approaches have been used previously by Thunmann et al. [126, 211] for calculation of the biomass pyrolysis gas composition, Klason and Bai [212] for calculation of biomass combustion in a fixed bed, and Naves et al. [116] for prediction of the biomass pyrolysis products.

The model can be written as

$$\mathbf{A}\mathbf{Y} = \mathbf{R}, \tag{5.4}$$

where matrix $\mathbf{A}$ is

$$\mathbf{A} = \begin{bmatrix} \beta_{C,C_3H_8} & \beta_{C,C_2H_4} & \beta_{C,CH_4} & \beta_{C,CO} & \beta_{C,CO_2} & 0 & 0 \\ 0 & 0 & 0 & \beta_{O,CO} & \beta_{O,CO_2} & \beta_{O,H_2O} & 0 \\ \beta_{H,C_3H_8} & \beta_{H,C_2H_4} & \beta_{H,CH_4} & 0 & 0 & \beta_{H,H_2O} & \beta_{H,H_2} \\ LHV_{C_3H_8} & LHV_{C_2H_4} & LHV_{CH_4} & LHV_{CO} & 0 & 0 & LHV_{H_2} \end{bmatrix}. \tag{5.5}$$

The first three rows of matrix $\mathbf{A}$ are from element mass conservation (i.e., Eq.5.3), and the last row is from the energy conservation law during pyrolysis. Matrix $\mathbf{Y}$ and the right-hand-side term $\mathbf{R}$ are respectively

$$\mathbf{Y} = \begin{bmatrix} Y_{C_3H_8,F} \\ Y_{C_2H_4,F} \\ Y_{CH_4,F} \\ Y_{CO,F} \\ Y_{CO_2,F} \\ Y_{H_2O,F} \\ Y_{H_2,F} \end{bmatrix} \quad \text{and} \quad \mathbf{R} = \begin{bmatrix} \beta_{C,F} - Y_{ch,F} \\ \beta_{O,F} \\ \beta_{H,F} \\ \alpha \cdot LHV_V \end{bmatrix}, \tag{5.6}$$

where $\alpha = \beta_{C,F} + \beta_{H,F} + \beta_{O,F} - Y_{ch,F}$. LHV_V denotes the lower heating value of pyrolysis gas. Eq. (5.4) consists of 4 equations for 9 unknowns, i.e., the

pyrolysis yield $Y_{k,F}$ and LHV_V. Five additional equations are required to close the system of equations.

Table 5.1: Empirical parameters derived by Neves et al. [116].

Equation	Coefficient of determination
$Y_{\mathrm{H_2,F}} = 0.145 \times (1 - exp(-0.11 \times 10^{-2} \cdot T_r))^{9.384}$	$R^2 = 0.94$
$Y_{\mathrm{CO,F}} = Y_{\mathrm{H_2,F}} \cdot (3 \times 10^{-4} + 0.0429/(1 + (T_r/632)^{-7.23}))^{-1}$	$R^2 = 0.88$
$Y_{\mathrm{CH_4,F}} = -2.18 \times 10^{-4} + 0.146 \times Y_{\mathrm{CO,F}}$	$R^2 = 0.88$
$Y_{\mathrm{ch,F}} = 0.106 + 2.43 \times exp(-0.66 \times 10^{-2} \cdot T_r)$	$R^2 = 0.56$
$\mathrm{LHV}_V = -6.23 + 2.47 \times 10^{-2} \cdot T_r$	$R^2 = 0.78$

Naves et al. [116] reviewed the pyrolysis experimental data in the literature and found empirical relations for pyrolysis products $Y_{\mathrm{H_2,F}}$, $Y_{\mathrm{CO,F}}$, $Y_{\mathrm{CH_4,F}}$, $Y_{\mathrm{ch,F}}$ and the pyrolysis gas lower heating value LHV_V with expect to variations of T_r. The empirical relations are shown in Table 5.1. Eqs. 5.2 and 5.4 and the five empirical relations in Table 5.1 constitute a closed system of equations to compute the stoichiometric coefficients x_k.

Table 5.2: Heterogeneous and homogeneous reactions and the corresponding kinetic rates. Note: $E^{'}$ is defined as $E^{'} = E/R_u$ [K].

|	Reactions	A_k	$E_k^{'}$ [K]	Ref.
R1	$C + CO_2 \rightarrow 2CO$	8.3 s/m	5,256	[213]
R2	$C + H_2O \rightarrow CO + H_2$	45.6 s/m	5,256	[213]
R3	$CO + H_2O \rightarrow CO_2 + H_2$	2.5×10^8 m^3/(kmol·s)	16,597	[214]
R4	$CO_2 + H_2 \rightarrow CO + H_2O$	9.4×10^9 m^3/(kmol·s)	20,563	[214]
R5	$CH_4 + H_2O \rightarrow CO + 3H_2$	312 m^3/(kmol·s)	15,098	[214]

The global heterogeneous and homogeneous reactions are employed to couple with the CFD model and listed in Table 5.2.

5.2 Numerical method and computational cases

The MP-PIC with PCM and DKM models are implemented in an open-source, finite volume-based CFD code, OpenFOAM v6 [186]. More information about the numerical scheme is given in Section 3.3. To maintain the computational efficiency of the DKM model, an efficient cell search algorithm is required to find the neighboring cells for source term redistribution. Detailed information about the cell search scheme used in the DKM is given in Chapter 4.

Two lab-scale fluidized bed gasifiers are selected to validate the present model. A schematic illustration of the gasifiers and computational domains is shown in

Fig. 5.1. The first gasifier was studied experimentally by Song et al. [52], and numerically simulated by several groups [58, 67, 102, 103, 168]. The gasifier is of a rectangular shape, with a cross-section of 40×230 mm^2, and a height of 1500 mm. Biomass and gasification agent (a mixture of steam and inert gas nitrogen) were supplied to the gasifier through an inlet at the bottom of the gasifier, Fig. 5.1b. The biomass particles were transported by the gasification agent upwards in the gasifier and mixed with hot bed materials (silicon sand particles), where the biomass particles underwent drying, pyrolysis, and char/steam gasification. Bed materials and residual char particles in the gasifier were circulated to a high-velocity fluidized bed combustor where the air was supplied to burn out the residual char from the gasifier, see Fig. 5.1a. Cyclones and a combination of several loop seals were employed to allow for the bed materials and residual char to be circulated between the gasifier and the combustor and to prevent bypassing of the flue gas from the combustor to the gasifier. Electric heaters were used in the gasifier and the combustor to control the temperature of the combustor and gasifier. Thus, the gasifier was operating independently of the combustor. For this reason, in previous numerical studies of the gasifier, the combustor section was neglected for simplicity and the results were shown to be acceptable [58, 67, 102, 103, 168]. This approach is taken here as well to allow for a comparison of the present results with previous numerical simulations.
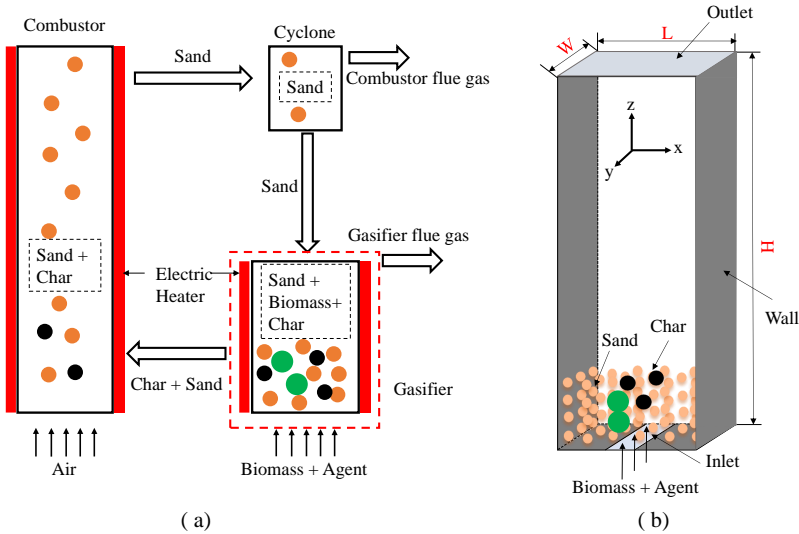
Figure 5.1: Schematic illustration of lab-scale bubbling fluidized bed reactors of Song et al. [52] and Erkiaga et al. [46]. The gasification agent is a mixture of nitrogen and steam for Song et al. [52] and pure steam for Erkiaga et al. [46], respectively. Note: the particles with yellow, black, and green represent the sand, char, and biomass, respectively.

Gasification products were collected at the outlet in the upper part of the gasifier. Yields of gaseous products at the outlet of the gasifier were measured at varying steam/biomass ratios (SR) using sampling techniques and an offline gas analyzer (chromatograph, Agilent 6890N), from which the mass fractions of H_2, O_2, CO, CO_2, CH_4, and other heavier hydrocarbons were measured. The steam/biomass ratio is defined as the ratio of the mass flow rate of steam to that of biomass. In the experiments of Song et al. [52], the SR was varied from 0.8 to 2.0 with the operating temperature of $T_r = 820°C$. Note that T_r is the reference temperature of the gasifier, which is the temperature of the gasifier wall and the characteristic temperature of the bed materials. Biomass, steam, and N_2 were supplied from an orifice with a 10 mm width at the center of the bottom plane of the reactor. The N_2 was used as the pneumatic conveying medium for biomass at a flow rate of 6.9×10^{-4} kg/s. Biomass, which was fresh pine wood, was injected with a fixed feeding rate of 8.3×10^{-4} kg/s, and a total weight of 11 kg of sand was fed in the gasifier at the start. The ultimate and proximate analysis of the biomass is presented in Table 5.3. The initial temperature of biomass particles is 25 °C, whereas the initial temperature of the bed material is set to T_r. The physical properties of initial biomass and sand particles are presented in Table 5.4. In the model, the size distribution of particles is considered using the Rosin-Rammler distribution function. The number of sand parcels was selected to be 66,129 and 3000 biomass parcels per second were injected into the domain.

Table 5.3: Ultimate and proximate analyses of the biomass fuels in gasifiers of Song et al. [52] and Erkiaga et al. [46].

Ultimate analysis [wt%]	Biomass	C	H	O	N &S
Song et al. [52]	Pinewood	46.29	6.48	46.08	1.15
Erkiaga et al. [46]	Pindwood sawdust	49.33	6.06	44.57	0.04
Proximate analysis [wt%]	Volatile	Fixed Carbon	Moisture	Ash	
Song et al. [52]	71.78	14.77	11.89	1.56	
Erkiaga et al. [46]	73.4	16.7	9.4	0.5	

Table 5.4: Initial biomass and sand particle properties for the cases of Song et al. [52] and Erkiaga et al. [46].

Gasifiers	Particles	d_i [mm]	ρ_i [kg/m^3]	$C_{p,i}$ [J/kg/K]	T_i [°C]
Song et al. [52]	Biomass	$1 \sim 2.5$	750	1500	25
	Sand	$0.25 \sim 0.7$	2300	840	820
Erkiaga et al. [46]	Biomass	$0.3 \sim 1$	750	1500	25
	Sand	$0.3 \sim 0.4$	2600	840	$800 \sim 900$

The second gasifier selected in this Chapter is the one experimentally studied by Erkiaga et al. [46]. This case was chosen to investigate the gasification process

with varying SR and T_r. The main section of the gasifier is of cylindrical shape and has a dimension of 225 mm in height, and 60.3 mm in diameter. The gasifier was connected to a tube of 7.6 mm diameter at the bottom plane through a conical section of 73 mm height. The biomass fuel was supplied to the top of the gasifier whereas the gas mixture of air, nitrogen, and steam was supplied from the tube at the bottom plane. The gasifier was placed inside a 1250W radiant oven and the operating temperature was adjustable, from 800 °C to 900 °C. The SR was varied from 0 to 2. For the case with SR of 1, the steam flow and biomass flow rate were both 1.5 g/min. For the case with SR of 2, the biomass feeding rate was reduced to 0.75 g/min. For the case with SR of 0, the steam was replaced by N_2 with a flow rate of 2 L/min. A total mass of 0.07 kg of sand was fed to the gasifier at the start. The ultimate and proximate analysis of the biomass is presented in Table 5.3. The composition of sand is assumed to be pure calcium carbonate. The physical properties of the initial biomass and sand particles are presented in Table 5.4. In the numerical simulations, the gasifier geometry was simplified to a cuboid, following the same strategy for the gasifier of Song et al. [52]. It has been shown that the gasification products at the top of the gasifier are insensitive to the detailed geometry of the gasifier since the height of the gasifier is 5 times the width of the gasifier. The residence time of the biomass particles is sufficiently long, which allows for a complete gasification process.

For the two gasifiers, the outlet boundary of the computational domain is on the top plane of the gasifiers, where a fixed-pressure boundary condition is applied and a zero-gradient condition for the rest of the variables is assumed. The wall boundary is assumed to be non-slip and constant temperature (the gasifier operating temperature T_r). The computational cases in Table 5.5 are simulated using 64-cores of a Xeon E5-2698v3 Haswell computer platform (2.3 GHz CPU) to obtain results for a physical time of 30 seconds of the gasification process. The running time of each case is less than 24 h (1536 CPU hours). The geometry of the first gasifier was simplified to a computational domain with a dimension of 1200×230×40 mm. The total number of mesh cells is 30,000 with a cell number of 200×30×5 in various dimensions. The geometry of the second gasifier was simplified to a cuboid with a dimension of 300×60×8 mm^3. The gas flow inlet was simplified to an 8×8 mm^2 square. The total number of mesh cells is 18,000 with a cell number of 150×30×4 in various dimensions.

5.3 Results and discussion

Seven computational cases were simulated to evaluate the gasification model and to investigate the gasification process. Table 5.5 shows the computational cases. Cases 1–4 are based on the gasification experiments of Song et al. [52]. In these cases, the impact of local overloading of particles on the predicted results from PCM and DKM models is evaluated (Cases 1 and 2), and the impact of parameter d_{max} on the DKM results is studied (Case 3). In Case 4, the influence of SR on the predicted gasification product gas yield is investigated. Cases 5–7 are based on the gasifier of Erkiaga et al. [46]. The performance of the two pyrolysis models for the prediction of gasification products is evaluated under various operating temperatures and SRs.

Table 5.5: Computational cases, operating conditions, and numerical setup. In the PCM and DKM cases the pyrolysis model (Eq. 4.1) is based on constant values of stoichiometric coefficients, while DKMC indicates the DKM model with the new pyrolysis model. d_p is the equivalent diameter of the sand parcel, $d_p = (6m_s/\rho_s\pi)^{(1/3)}$. Here, m_s is the mass of a sand parcel.

| Cases	Model	T_r	SR	$\alpha_{c/p}$	d_{max}/d_p	Exp.
	[-]	[°C]	[-]	[-]	[-]	[-]
1	DKM	820	1.2	1.33∼ 3.98	5	Song et al. [52]
2	PCM	820	1.2	1.33∼ 3.98	-	Song et al. [52]
3	DKM	820	1.2	1.98	3∼9	Song et al. [52]
4	DKM	820	0.8∼2	1.98	5	Song et al. [52]
5	DKM	900	0∼2	1.9	5	Erkiaga et al. [46]
6	DKM	700∼900	1	1.9	5	Erkiaga et al. [46]
7	DKMC	700∼900	1	1.9	5	Erkiaga et al. [46]

The sensitivity of numerical results to the mesh size is investigated in Cases 1 and 2. Five different mesh sizes are used, i.e., 0.0067, 0.008, 0.01, 0.0133, and 0.02 m, respectively. It is found that the yields of gasification products (CO, H_2, CH_4, and CO_2) at the gasifier outlet predicted using the five meshes and DKM model differ only slightly. As the mesh size is decreased from 0.01 m to 0.0067 m, the yield of CO decreased by 3%, the yield of H_2 increased by 0.2%, the yield of CH_4 increased by 1%, and the yield of CO_2 increased by 1%. The results from PCM are more sensitive to the mesh size. The simulation with PCM did not converge when the finest mesh (0.0067 m mesh size) was used due to the local overloading of particles. Based on the mesh sensitivity study, the 0.01 m mesh size was selected as the baseline mesh size in the following simulations. Further discussion on the mesh size and local overloading will be presented in Chapter 4.

5.3.1 Simulation of fluidization and bubble evolution
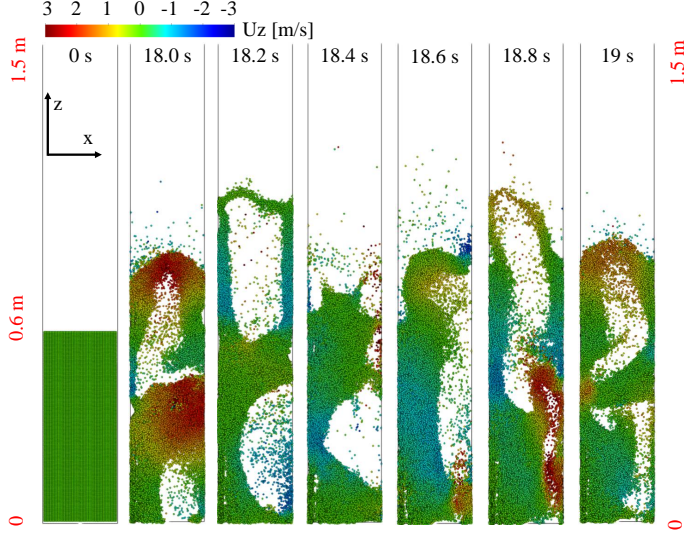
Figure 5.2: Instantaneous distribution of sand parcel showing the formation and collapse of the bubbles in the gasifier, simulated using MP-PIC with DKM for the baseline case ($T_r = 820\ ^\circ$C, SR $= 1.2$, Case 1) of Song et al. [52].

Figs. 5.2 and 5.3 show the formation and development of gas bubbles in the bed over time for the baseline case (SR $= 1.2$ and $T_r = 820\ ^\circ$C, i.e., Case 1) of Song et al. [52]. The start of biomass injection is $t = 0$ s. At $t = 0$, the sand particles are uniformly distributed in the lower part of the gasifier (with a 0.6 m height). After 18 seconds the quasi-steady-state fluidization is reached. The formation and collapse of bubbles evolve in time and space. A typical period of bubble formation and collapse can be visualized from 18 s to 19 s in Figs. 5.2 and 5.3. As shown in Fig. 5.2, at $t = 18.0$ s two large gas bubbles are formed with one bubble close to the inlet and another bubble in the higher bed region. Inside the bubble higher gas pressure develops because of the stack of sand parcels. Due to the high momentum of the gas flow from the bottom inlet, the bubble rises, and the bed expands. From 18 s to 18.2 s, the high-pressure gas pushes the sand parcels further upwards. Since the parcels around the bubble move slower than the gas in the bubble, the gas escapes from the bubble, and the bubble collapse at $t = 18.4$ s. The bed materials return to a similar height as that at $t = 18.0$ s, followed by a new sequence of formation ($t = 18.6$ s to $t = 18.8$ s) and collapse of the bubble at $t = 19$ s. This process of bubble formation
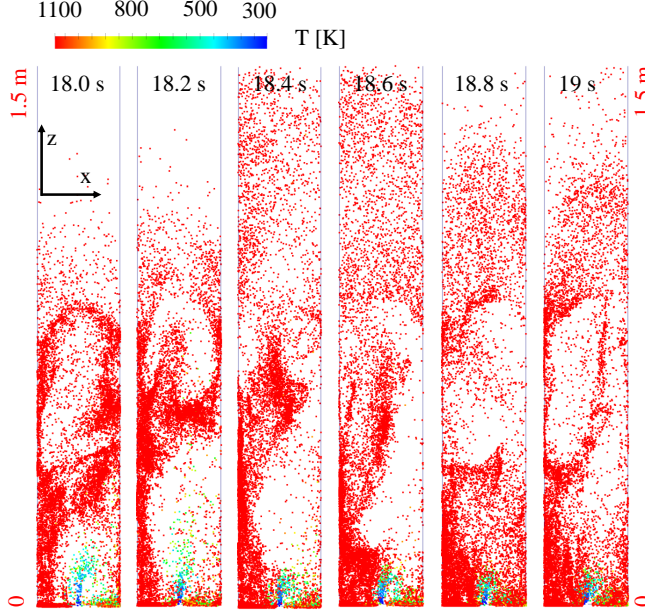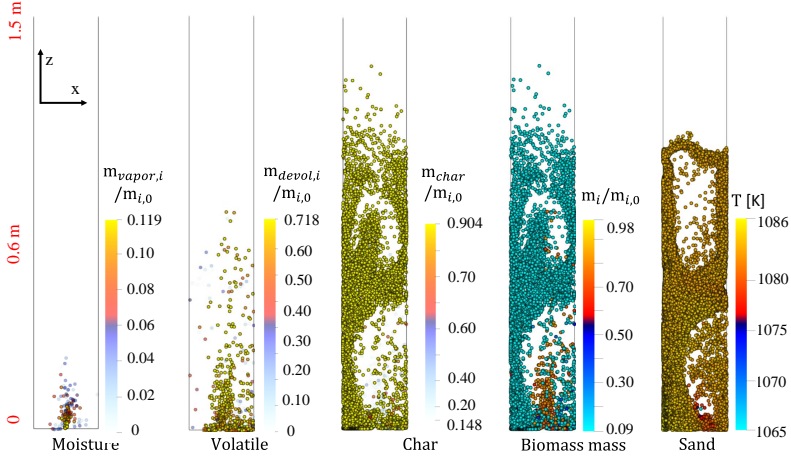
Figure 5.3: Instantaneous distribution of biomass parcels following the formation and collapse of the bubbles in the reactor, simulated using MP-PIC with DKM for the baseline case ($T_r = 820\ °C$, SR = 1.2, Case 1) of Song et al. [52]. The color bar indicates the particle temperature.

and collapse is rather random, and bubbles at different positions have different fluidization frequencies due to different pressure drops. The biomass particles follow a similar pattern as the sand particles, except that some small biomass char can fly further downstream than the sand particles do.

The gasifier is a spout-fluidized bed reactor. The gas velocity in the proximity of the steam/biomass inlet is higher than the fluidization velocity of the particles. Since the size of the sand particles varied from $0.25 \sim 0.75$ mm, and initial biomass particle size varied from $1.0 \sim 2.5$ mm, the minimum fluidization velocity U_{mf} varies from 0.048 m/s $\sim$ 0.73 m/s and 0.48 $\sim$ 0.76 m/s for the sand and biomass particles, respectively, according to Ergun correlation [148, 215] for the minimum fluidization. The inlet gas velocity varied from 3.4 m/s to 5.8 m/s, under the different steam/biomass ratio conditions listed in Table 5.5.

The high inlet gas velocity carried the biomass particles upwards from the bottom of the gasifier. The fuel particles are mixed with the sand particles and heated up quickly by the sand particles, from room temperature to the reactor operating temperature T_r. As a result of drying and devolatilization, the mass of the particles decreased quickly. Figure 5.4 shows the distribution of bio-

Figure 5.4: Instantaneous distributions of wet biomass particles (with the mass of water vapor in the particle $m_{vapor} > 0$), of particles undergoing pyrolysis (with volatile mass in the particle $m_{devol} > 0$), of char particles (m_{char}, with a negligible mass of volatile in the particle), and of the entire fuel particles with the color denoting the mass of the particles normalized by their corresponding initial mass, and distribution of the sand particles with color indicating their temperature. The results were from numerical simulations using MP-PIC with DKM for the base case ($T_r = 820\ ^{\circ}$C, SR $= 1.2$) of Song et al. [52]. The time instant corresponds to t=18.2 s in Fig. 5.2).

mass particles at a time instant (corresponding to t=18.2 s in Fig. 5.2), where the mass loss due to drying ($m_{vapor}/m_{p,0}$), and pyrolysis ($m_{devol}/m_{p,0}$) can be identified. Drying of particles occurred in the proximity of the gasifier inlet, $z < 0.3m$, whereas pyrolysis took place in the region of $z < 0.7m$. Most of the fuel particles are in the form of char. As shown in Fig. 5.4, the spatial distributions of sand particles and biomass particles show certain similarities, e.g., very few particles in the gas bubble region, but the distributions are not identical.

The process of bubble formation and collapse has an important impact on the gasification process and the local concentration of gas species. This can be evidenced in the instantaneous distribution of CO_2, which indicates the result of the pyrolysis, gasification, and volatile reactions, see Fig. 5.5. The CO_2 concentration is high at the bottom of the gasifier in the region surrounding the inlet, e.g., region A. This can be attributed to the accumulation of pyrolysis products in the recirculation zone. Slightly above the inlet, in region B, the CO_2 concentration becomes low because of local high gas velocity in the gas bubble and thus the short residence time of local biomass particles. In this region, the biomass particles are newly injected from the bottom inlet and the particles are undergoing drying and the biomass particle temperature is low, see Figs. 5.2 and 5.3. Further downstream in region C, the biomass particles are heated up
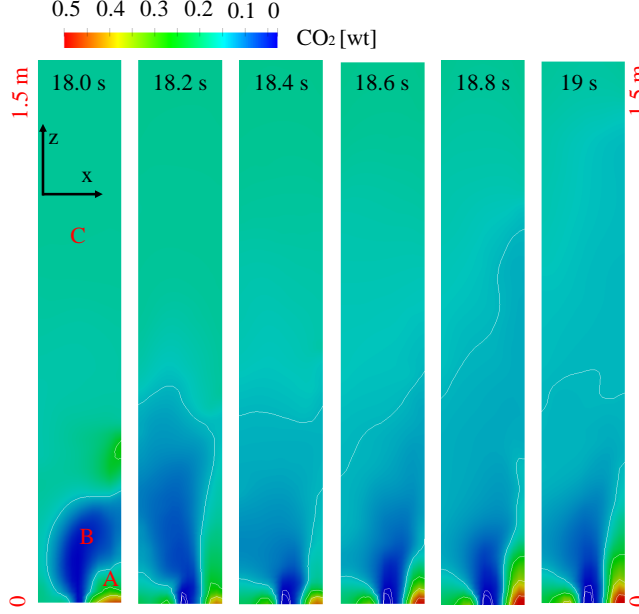
Figure 5.5: Instantaneous distribution of mole fraction of CO_2 in the reactor, simulated using MP-PIC with DKM for the base case ($T_r = 820\ ^\circ$C, SR $= 1.2$) of Song et al. [52].

quickly to reactor temperature (T_r) and the pyrolysis and gasification reactions start to occur resulting in an increase of CO_2 concentration.

The spatial distribution of CO_2 varies significantly in time in the vicinity of the bubble formation/collapse region. The bubble region disturbs the flow pattern making the CO_2 distribution vary in time. Further downstream where the sand particles are scarce, the residence times of the biomass particles are sufficiently long, and the gasification process is nearly completed. The CO_2 distribution becomes more uniform. A nearly constant value of CO_2 mole fraction is observed at the reactor outlet (for $t = 18$ s to $t = 19$ s). This is true for all gaseous species. Thus, the results at the outlet after 18 s are used to compare with the experiments of gaseous species from the gasifier.

## 5.3.2   Local overloading and performance of the DKM model

The local overloading can happen when the solid volume fraction, θ_s, is higher than the physical packing limit in a cell. The physical packing limit refers to the maximum solid volume fraction that the local cell can accommodate. As

discussed in previous studies the limit for such a system is $\theta_s \sim 0.62$, see e.g. [112, 127]. Exceeding this limit will lead to numerical instability or non-physical results, such as a violation of mass conservation.

Fig. 5.6 shows the comparison of the performance of DKM and PCM with regard to local overloading. A distribution function $f(\theta_s)$ for the solid mass fraction of the cells containing parcels, as expressed below, is used to evaluate the model performance with regard to overloading,

$$f(\theta_s) = N_{\theta_s}/N_{cell}. \tag{5.7}$$

In this expression, N_{θ_s} and N_{cell} are the number of cells with the value of θ_s and the total number of cells containing one or more parcels in the domain, respectively. This function is calculated at 5 s, 10 s, and 15 s for both models, as presented in Fig. 5.6. In PCM, over 15% of cells fall in the overloading region ($\theta_s > 0.62$) while in the DKM model, the overloading problem is improved and over 98% of θ_s is less than 0.6.
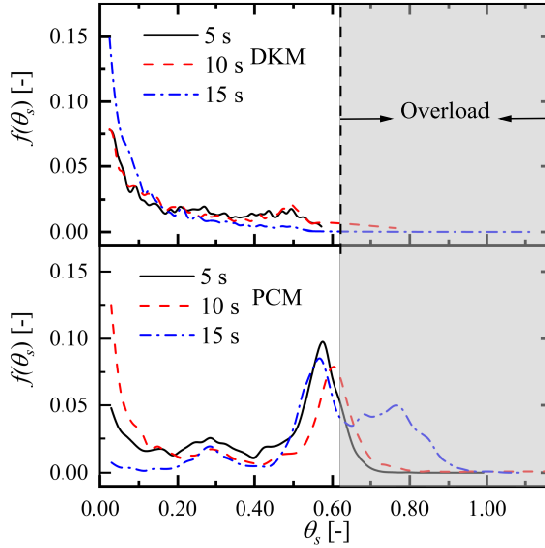
Figure 5.6: The distribution function of solid phase volume fraction at different time t for cases of Song et al. [52], 5s, 10s, and 15s simulated using DKM (Case 1) and PCM (Case 2). The shaded area indicates the overloading conditions.

Large source terms and small $\alpha_g (= 1 - \theta_s)$ from large parcels in a cell can cause numerical instabilities, leading to numerical artifacts. This issue arises when small cell size is used in comparison to the size of the parcel. To quantify this effect, the ratio between the cell size and the parcel size, as defined below, is
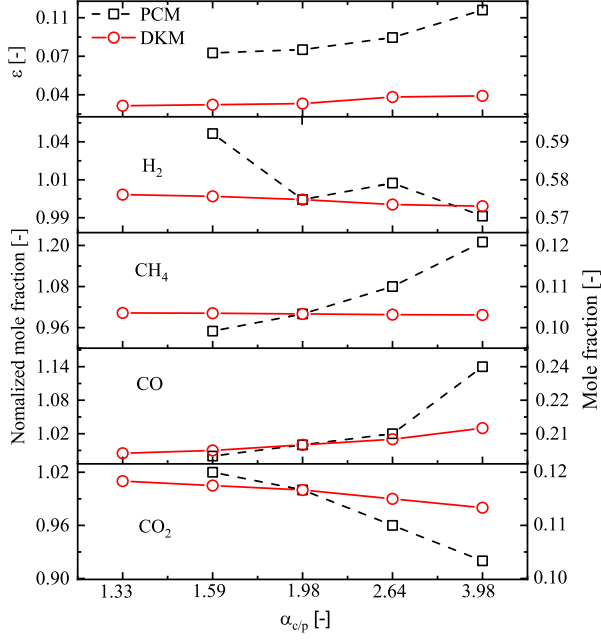
Figure 5.7: Effect of mesh size on the predicted product gas yield at the outlet of the gasifier of Song et al. [52]. The time-averaged mole fractions of species at the outlet of the gasifier are normalized based on the case with $\alpha_{c/p} = 1.98$. The results are obtained with DKM (Case 1) and PCM (Case 2).

used to evaluate the model performance,

$$\alpha_{c/p} = \sqrt[3]{V_c}/d_p. \tag{5.8}$$

where d_p is the equivalent diameter of the same parcel, see Table 5.5.

Five different mesh sizes are used, resulting in five different $\alpha_{c/p}$ of 1.33, 1.59, 1.98, 2.64, and 3.98. Smaller $\alpha_{c/p}$ means higher mesh resolution. These values correspond to grid cell sizes of 0.0067 m, 0.008 m, 0.01 m, 0.0133 m, and 0.02 m, respectively. Fig. 5.7 shows the results from PCM and DKM with regard to different mesh sizes and different $\alpha_{c/p}$. The mole fractions of different species at the outlet of the reactor, as presented in Fig. 5.7, are normalized with respect to the case with $\alpha_{c/p}$ of 1.98. At $\alpha_{c/p}$ of 1.33, the finest grid, the PCM model did not give a converged numerical solution due to local overloading. Increasing $\alpha_{c/p}$ to 1.59, PCM predicted a significantly higher H_2 and CO_2 mole fraction but a lower CO and CH_4. Within the studied range of $\alpha_{c/p}$, the PCM predicted a maximum relative change of the mole fractions of 4%, 21%, 13% and 8% for H_2, CH_4, CO, and CO_2, respectively. In DKM, the relative change is less than 5% for all the species. Overall, PCM strongly depends on predicted results on

the mesh size. DKM shows an improved mesh independence for all the studied cases, due to the better mass conservation of the solid phase.

To examine the mass loss due to the use of the θ_s limiter, the total mass of sand particles in the domain is computed in two different ways, (a) by summing up the total mass of parcels ($M_{s,d}$), and (b) by integration of the solid volume fraction in the domain ($M_{s,c}$). A mass loss error (ε) is defined as,

$$\varepsilon = \frac{M_{s,d} - M_{s,c}}{M_{s,d}} \times 100\%, \tag{5.9}$$

to evaluate the performance of the two models. The total mass of sand ($M_{s,d}$) computed from the discrete phase is

$$M_{s,d} = \sum_{j=1}^{N_{sand}} m_{s,j}, \tag{5.10}$$

where N_{sand} is the total number of sand parcels in the entire gasifier and $m_{s,j}$ is the mass of j-th sand parcel. It is found that $M_{s,d}$ is 1.25 kg, the same as that initially placed in the gasifier of Song et al. [52]. This means that the mass of sand is conserved in the gasifier. On the other hand, $M_{s,c}$ computed from the solid volume fraction of the sand particles (θ_s) indicates the mass loss due to the use of θ_s limiter.

$$M_{s,c} = \rho_s \int_{\Omega} \theta_s(\mathbf{x}, t) dV, \tag{5.11}$$

where ρ_s is the density of sand particles and Ω is the entire domain of the reactor. As shown in Fig. 5.7, the mass loss error in the prediction with DKM is less than 4%, and the result has a weak dependence on mesh size. With PCM, an increase in $\alpha_{c/p}$ leads to an increase in mass loss error ε, from 7% to more than 11%. With a coarse mesh (large $\alpha_{c/p}$), the local overloading will have a large contribution to the mass loss due to the large local cell volume. A fine mesh would however give rise to high local source terms and locally small α_g. This leads to numerical instability, e.g., in the case of $\alpha_{c/p} = 1.33$, the simulation with the PCM model could not converge.

The parameter d_{max} in Eq. 4.6 is selected to define the size of the domain of redistribution in the DKM model. A sensitivity study of the results to d_{max} is performed. As shown in Fig. 5.8, four different d_{max}/d_p of 3, 5, 7, 9 are tested to evaluate the sensitivity of predicted gasification products to d_{max}. The mole fractions of species have low sensitivity to d_{max}/d_p in the range of $3 \sim 10$. As d_{max}/d_p increases, the number of surrounding cells increases at a rate of $(d_{max}/d_p)^3$ in the three-dimensional domain. The number of surrounding cells
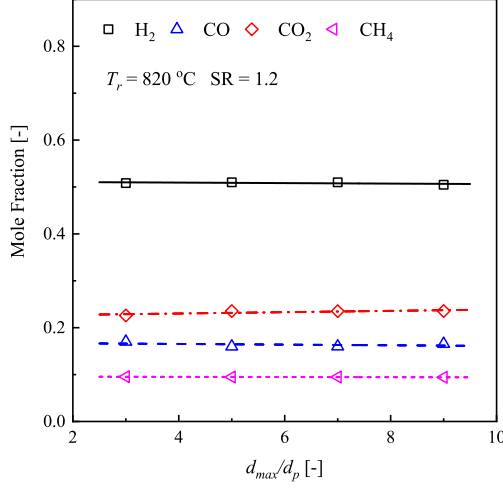
Figure 5.8: Effect of parameter d_{max}/d_p in the DKM (Case 3) on the predicted gasification products at the outlet of the gasifier of Song et al. [52].

to distribute the source terms will increase eight-fold when d_{max}/d_p is increased from 2 to 4 leading to higher computational cost. A value of $3 \sim 5$ for d_{max}/d_p is shown suitable for the cases evaluated in this Chapter.

5.3.3 Biomass gasification under different steam/biomass ratio conditions

The DKM model is used to investigate the effect of operating conditions on the yield of different species in FBGs. In Fig. 5.9, the mole fractions of H_2, CH_4, CO, and CO_2 at the outlet of the gasifier are presented for different steam/biomass ratios. Experimental measurements and previous numerical results are presented for comparison. The current numerical results agree well with the experimental measurements of Song et al. [52], as well as the simulations of Wang et al. [67] and Qi et al. [103]. The trend of increasing H_2 yield and decreasing CO yield with increasing SR is very well captured.

Increasing the steam/biomass ratio corresponds to the increase of steam concentration and superficial velocity of the FBG. As shown in Fig. 5.9(a), by increasing the SR, the mole fraction of H_2 increases while the mole fraction of CH_4 decreases. The mechanism behind this can be explored using the present model. During the gasification process of biomass and homogeneous reactions, H_2 is produced from three sources: pyrolysis, the heterogeneous reaction of char
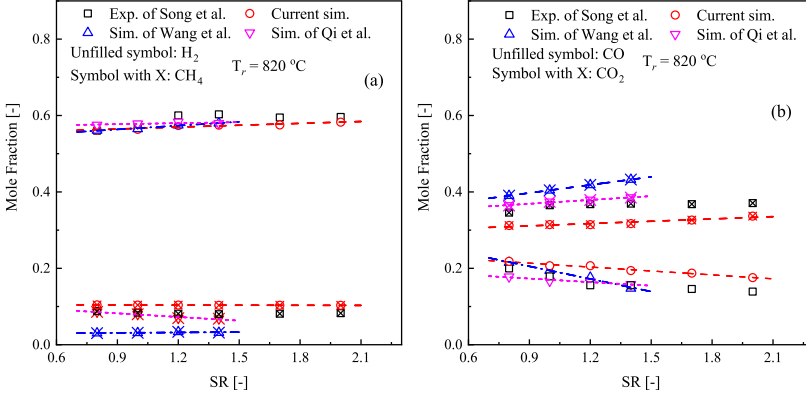
Figure 5.9: Comparison of the mole fractions of H_2, CH_4, CO, and CO_2 between the present simulations (Dashed line with circle mark) using DKM (Case 4), previous simulation by Wang et al. [67] (Dash dotted line with triangle mark), the previous simulation by Qi et al. [103] (Short dashed line with nabla mark), as well as with experiments of Song et al. [52] (Square mark) at different steam/biomass ratios and operating temperature T_r of 820 °C. Note: A value of 0.2 is added to the mole fractions of CO_2.

and steam (R2), and homogeneous reactions (R3, R4, and R5). The pyrolysis process is highly affected by the furnace temperature, however, less affected by the steam concentration. The stoichiometric coefficients in Eq. 5.1 are constant for all the SR conditions in this model, indicating that the variation of the mole fractions of H_2 and CH_4 with SR is not due to pyrolysis reactions. On the other hand, increasing the steam concentration will increase the rate of the heterogeneous reaction (R2) leading to higher H_2 formation. Moreover, the reaction rate of char, as presented in Eq. 3.26, is affected by parameters As_i, p_k, $R_{d,k}$, and Da'_k. The increase of SR increases the rate of reaction R2 by increasing p_k, since As_i and Da'_k are constants ($R_{r,k} \gg R_{d,k} \to Da'_k \approx 1$), and $R_{d,k}$ is only affected by the gas and particle temperatures. However, the effect of R2 on H_2 formation is very limited due to the very small diffusion rate and parcel surface area. Therefore, the increase of H_2 with SR is mainly due to the homogeneous reactions R3 and R5, which are in favor of H_2 formation due to the increase of steam concentration. Related to water-gas shift reaction R3 and R4, as SR increases, the rate of R3 increases while the rate of R4 has no significant change, leading to more consumption of CO and in favor of H_2 and CO_2 formation. Compared to the trend of H_2, the CH_4 mole fraction is rather constant, due to the fact that the kinetic rate of reactions R4 and R5 is much slower than R3.

Fig. 5.9(b) shows the comparison of mole fractions of CO and CO_2 between the results from the current simulation and experimental data of Song et al. [52], as well as the simulations of Wang et al. [67] and Qi et al. [103]. The results show
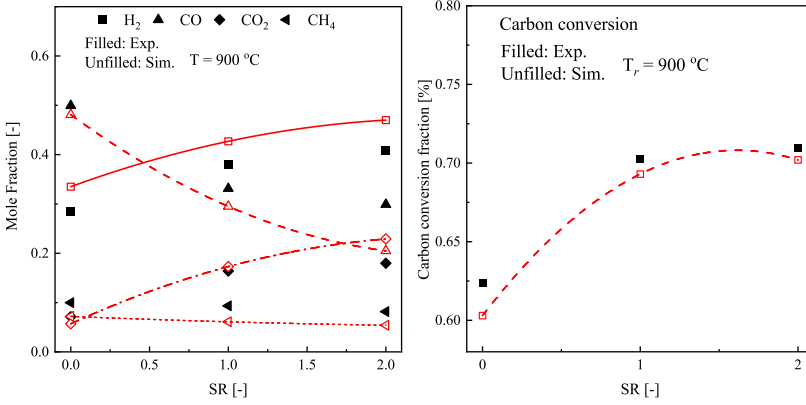
Figure 5.10: Comparison of the mole fractions of H_2, CH_4, CO and CO_2, and carbon conversion ratio between predictions using the DKM (Cases 5) and experiments of Erkiaga et al. [46] (filled symbol) under different steam/biomass ratio conditions.

a decreasing trend of CO with increasing SR. CO is produced from the pyrolysis process, heterogeneous reactions R1 and R2, and homogeneous reactions R3, R4, and R5. By increasing SR, the reactions R4 and R5 are in favor of CO formation while the reaction R3 is in favor of CO consumption. Due to the kinetic rate R4 being much slower than R3, the mole fraction of CO decreases as the SR increases while the mole fraction of CO_2 increases.

5.3.4 Biomass gasification under different gasifier operating conditions

The gasifier of Erkiaga et al. [46] is selected to evaluate the gasification model in a wider range of operating conditions, including gasifier temperatures and steam/biomass ratios. Fig. 5.10 shows a comparison of the mole fractions of main gaseous products (H_2, CH_4, CO, and CO_2) and the carbon conversion ratio between the predictions using DKM with the new pyrolysis model and the experimental measurement. The carbon conversion ratio is defined as

$$CCR = \frac{\sum_k \beta_{C,k} Y_k}{\beta_{C,F}},$$
(5.12)

where Y_k represents the mass fraction of species k in the gasification products that contain carbon element, i.e., C_3H_8, C_2H_4, CH_4, CO, H_2, and CO_2. $\beta_{C,k}$ and $\beta_{C,F}$ are the element mass fraction of C in the species of k and in the DAF biomass, respectively, see Eq. (5.3). For a wide range of steam/biomass ratio, i.e. $0 \sim 2$, the simulation results agree well with the experimental measurement

of Erkiaga et al. [46]. Within the SR range of $0 \sim 1$, the composition of gasification products changes significantly with SR, and the carbon conversion ratio increases from 0.61 to 0.69. For the SR range of $1 \sim 2$, the product composition varies with SR at a slower rate compared to that under the low SR conditions. This result is consistent with the experiments of Song et al. [52], as shown in Fig. 5.9. The level of carbon conversion ratio reaches the maximum value of 0.7 and keeps nearly constant with further increase of SR.

The impact of SR on biomass gasification may be explained as follows. At low concentrations of steam, the gas products are mainly produced from pyrolysis. At high SR conditions, the high concentration of steam promotes the heterogeneous reaction (R2) and homogeneous water-gas shift reaction (R3). The enhanced heterogeneous reaction R2 results in a higher carbon conversion ratio and higher yield of H_2, along with enhanced production of CO. The enhanced water-gas shift reaction R3 converted a large portion of the CO to H_2 and CO_2, resulting in a further increase of the yield of H_2. With increasing SR, the homogeneous reaction R5 is also enhanced, which results in a decrease of CH_4 mole fraction in the final gasification products. Finally, as the steam surrounding the biomass particles tends to saturate at high SR, further increase of steam does not show an increasing impact on the rate of biomass gasification.

Fig. 5.11 shows a comparison of the compositions of gaseous products and the carbon conversion ratio at different T_r from the numerical simulations and the experiments of Erkiaga et al. [46]. The conventional model in which the stoichiometric coefficients of volatile are kept constant (M2), and the new pyrolysis model (M1), are used to simulate the gasification process. Since the predicted carbon conversion ratio of M1 agrees very well with the experiments at T_r of 900 °C, the stoichiometric coefficients at this temperature have been chosen in M2. The yields of H_2 and CO_2 and the carbon conversion ratio are shown to increase while the yields of CO and CH_4 are shown to decrease with increasing T_r. The yields of gaseous products show a nearly linear variation with T_r. The predicted results using the new pyrolysis model agree better with the experimental measurements of Erkiaga et al. [46] than the conventional pyrolysis model. Using the conventional pyrolysis model, the sensitivity of mass fractions of the products to T_r is significantly underestimated compared with the experimental measurements.

The mechanisms of biomass gasification at different gasifier operating temperatures can be explained as follows. The impact of T_r is manifested through the pyrolysis reaction, the heterogeneous reactions (R1 and R2), and the homogeneous reactions (R3, R4, and R5). Among these reactions, the pyrolysis reaction plays a very important role. As shown in Fig. 5.12, the mass fractions of pyro-
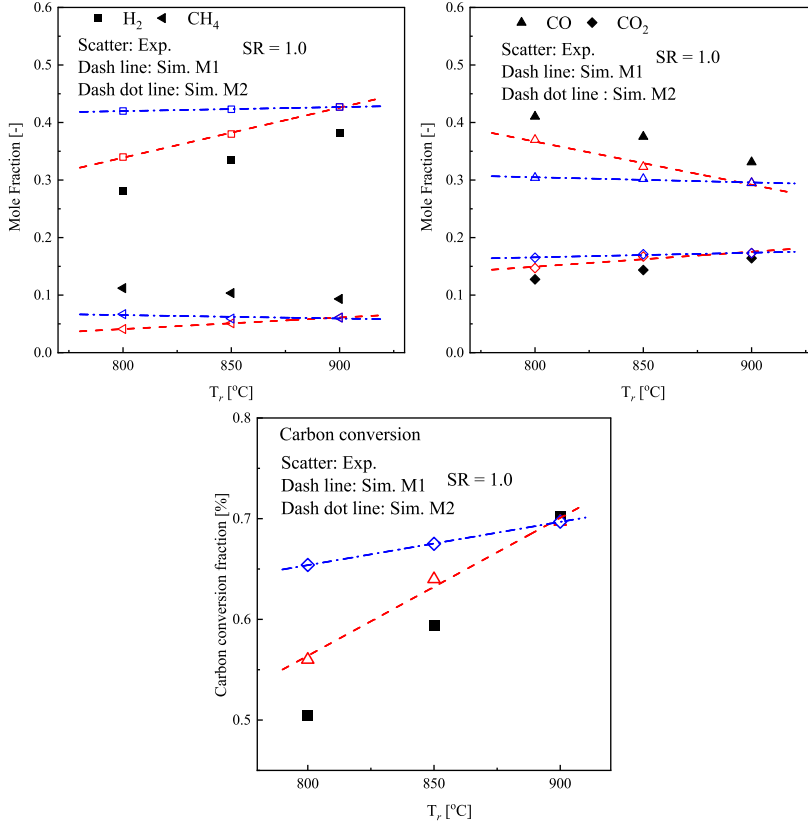
Figure 5.11: Comparison of the mole fractions of H_2, CH_4, CO and CO_2, and carbon conversion ratio between predictions of Case 7 with the DKMC (Dash line), Case 6 with the conventional pyrolysis model (Dash dot line) and the experiments of Erkiaga et al. [46] (filled symbol) under different operating temperatures.

lysis gas species are strongly affected by T_r. In particular, the mass fraction of H_2 increases with T_r, which results in an increasing mole fraction of H_2 in the final gasification products. The lower carbon conversion ratio at low T_r is also largely due to the high char mass fraction after the pyrolysis reaction.

Although the pyrolysis step has a great impact on the final products of biomass gasification, the char gasification reactions (R1, R2) and the homogeneous gas reactions (R3–R5) are also important. As shown in Fig. 5.12, CO_2 is the main gas species from pyrolysis below 850 °C while CO has the highest mass fraction above 850 °C. The trend of CO and CO_2 mass fractions of the final gasification product is however opposite to that after the pyrolysis, as shown in Fig. 5.11. The high CO mole fraction at low T_r is likely due to the higher amount of char, which results in a high production CO due to the gasification
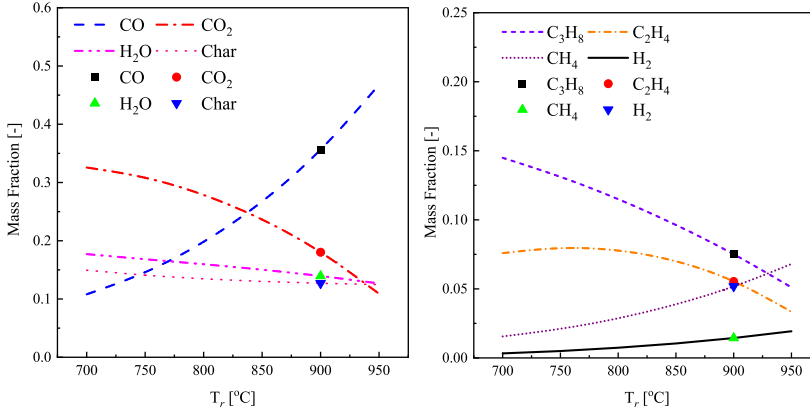
Figure 5.12: Mass fractions of pyrolysis gas products and char at varying T_r under conditions of the experiments of Erkiaga et al. [46]. The mass fractions of the pyrolysis gas and char were calculated using the pyrolysis model (Eq. 5.4) for a range of T_r (700 $^\circ$C $\sim$ 950 $^\circ$C).

reactions R1 and R2. Reaction R1 also consumes a large portion of CO_2 leading to a lower CO_2 mole fraction in the final gasification gas at low temperatures. Since the mass fraction of CH_4 in the pyrolysis gas is rather low, and CH_4 is involved only in reaction R5, the variation of the mole fraction of CH_4 is not highly sensitive to T_r. This explains the nearly constant CH_4 yield in the gasification gas at different T_r, which is observed in both experiments and model predictions. With the conventional pyrolysis model, the pyrolysis char and CO_2 are independent of T_r; the predicted final mole fraction of CO and CO_2 in the gasification products are therefore fairly independent of T_r. This indicates the importance of incorporating temperature-dependent stoichiometric coefficients in the one-step pyrolysis model Eq. (5.1).

5.3.5 Discussion

The developed pyrolysis model improves the prediction of gasification products at varying operating temperatures. However, certain limitations/shortcomings exist in the one-step pyrolysis model, which can be further explored and improved in the future. The one-step pyrolysis model is developed based on the empirical data of the pyrolysis experiments for various biomass fuels, under different operating conditions (heating rate, particle size, etc.). More data samples are needed to verify the reliability of the empirical corrections. Moreover, a more comprehensive pyrolysis mechanism of biomass and pyrolysis products (gaseous, char, ash, and tar) needs to be developed to address the complexity of pyrolysis

and the impact of biomass composition. The present one-step pyrolysis model is a step forward toward the computation of the pyrolysis products for varying biomass properties (i.e., the element mass fractions of C, H, and O) and operating temperature. However, only seven major pyrolysis products (CO, CO_2, CH_4, H_2, H_2O, C_2H_4 and C_3H_8) could be calculated using the pyrolysis model, see Eq. 20. When more than seven pyrolysis products are considered, the model cannot be closed due to the requirement of more empirical input. To this end, a multi-step pyrolysis model with low computational cost and a reduced model for tar decomposition in the gas phase is desirable to reveal the underlying pyrolysis mechanism in CFD simulations. Moreover, global homogeneous reactions, see Table 1, are employed in the current CFD model. These global reactions have been employed in CFD simulations of fluidized bed combustion and gasification due to their simplicity and high computational efficiency [58, 59, 67, 86–88, 103, 168, 169, 207, 216]. However, these global reactions do not consider the actual reaction paths occurring in the homogeneous phase, since key species such as radicals H, O, and OH are neglected. More detailed chemical reaction models with elementary reactions and radical species are required to uncover the transformation paths of gas species in the homogeneous phase.

5.4 Summary

A three-dimensional computational fluid dynamics (CFD) model is developed and evaluated for numerical simulations of biomass gasification in fluidized bed gasifiers (FBGs) under different steam/biomass ratio (SR) and gasifier operating temperature (T_r) conditions. The CFD model is based on the multi-phase particle-in-cell (MP-PIC) model and the distribution kernel method (DKM, Chapter 4) that aims to solve the local overloading problem in the numerical simulation of FBGs using the conventional particle centroid method (PCM). A new one-step pyrolysis model is proposed to improve the sensitivity of the gasification products to operating temperature T_r. The gas/solid interactions, particle collision, heat and mass transfer, radiation, and homogeneous and heterogeneous chemical reactions are considered in this model. The main conclusions are summarized as follows:

- The 3D CFD model with DKM can overcome the local overloading problem that the PCM can not simulate. A mesh-independent result can be achieved with the DKM, while the PCM results show a clear dependency on the mesh size. DKM yields a better agreement with the experimental measurements than the conventional PCM.

- The new empirical pyrolysis model can capture the trend of gasification products with respect to the variation in SR and T_r. It is found that the mole fractions of H_2 and CO_2 increase and the mole fractions of CO and CH_4 decrease as SR and T_r increase within a range of SR of $0 \sim 2$ and T_r of 800 °C $\sim$ 900 °C. The new pyrolysis model predicted a better dependence of the gasification products on T_r.

- The mechanisms of the experimentally observed trend of gasification yield are investigated based on the CFD model. The gasification products are affected by the biomass pyrolysis reaction, heterogeneous char gasification reactions, and homogeneous gas reactions. The H_2 concentration in the final gasification products and the carbon conversion ratio are strongly affected by the pyrolysis reaction. However, the heterogeneous char gasification reactions and homogeneous volatile gas reactions, in particular the water-gas shift reaction $CO + H_2O \leftrightarrow CO_2 + H_2$, have also an important impact on the CO, CH_4 and CO_2 concentrations in the final gasification products.

Chapter 6

CFD simulation of biomass combustion in an industrial CFB boiler
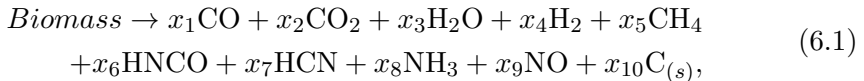
In this chapter, the MP-PIC model with the coarse grain method (CGM) and the distribution kernel method (DKM) discussed in the previous chapters is employed to investigate the hydrodynamic and combustion characteristics of biomass particles in an industrial-scale circulating fluidized bed (CFB) boiler. The challenge of CFD simulation in industrial-scale fluidized bed boilers is the high computational cost due to the huge number of particles in the system. With MP-PIC and CGM, local particle overloading could occur, leading to the numerical simulation diverging. The MP-PIC/CGM coupled with DKM was shown to overcome the local overloading problem. The CFD predictions were compared with onsite temperature experiments in the furnace. The predicted furnace temperature agreed fairly well with the data measured during the furnace operation. The CFD results were used to analyze the transient solids mixing and fluidization characteristics, and the thermochemical process in biomass combustion. The physical and chemical processes of the granular flow in the industrial-scale CFB boiler were analyzed to gain insight into the CFB boiler operation.

6.1   Methodology

In the current CFD model, the governing equations of the continuous and discrete phases involved in the fluidized bed boiler are described in the Eulerian

and Lagrangian frameworks, respectively. The detailed description of governing equations for the gas phase, turbulence closure models, and sub-models for the particle phase was presented in Chapter 3. In the following further details about the biomass pyrolysis model and gas phase NO_x chemistry are presented.

A one-step pyrolysis model involving nitrogen conversion is employed, following the literature [39, 58, 67, 103, 127, 146]. The one-step pyrolysis reaction model is written as

$$Biomass \rightarrow x_1CO + x_2CO_2 + x_3H_2O + x_4H_2 + x_5CH_4$$
$$+x_6HNCO + x_7HCN + x_8NH_3 + x_9NO + x_{10}C_{(s)}, \tag{6.1}$$

where $C_{(s)}$ denotes char in the solid phase. x_j are the stoichiometric constants, i.e., $x_1 = 0.5014$, $x_2 = 0.0954$, $x_3 = 0.0864$, $x_4 = 0.0512$, $x_5 = 0.1060$, $x_6 = 0.0021$, $x_7 = 0.0043$, $x_8 = 0.0067$, $x_9 = 0.0005$, and $x_{10} = 0.1458$. In this model, volatile nitrogen-containing species released during the pyrolysis process include NH_3, NO, HCN, and HNCO, whose release rates are proportional to biomass pyrolysis.

Biomass NO_x formation mechanism has been investigated for several decades. Winter et al. [217] investigated the NO_x formation of different biomass fuels in a fluidized bed combustor and a grate furnace. NO, N_2O, HCN, and NH_3 were measured in the flue gas shortly after biomass combustion while N_2O was rapidly converted to N_2. HCN was formed in quantities similar to NH_3 during woody biomass combustion and the HCN/NH_3 ratios depend on the H/N ratio in biomass fuels. According to the measurements of Bassilakis et al. [218] and Hansson et al. [219], HNCO is a significant intermediate product for NO_x formation during biomass combustion. In the study of Bassilakis et al. [218], the mass ratios (dry basis) of NH_3/HCN/HNCO at a heating rate of 30 K/min are 37/43/20 for wheat straw and 35/26/39 for tobacco, respectively. Hansson et al. [219] reported that the mass ratios (dry basis) of NH_3/HCN/HNCO are 57/28/15 at a pyrolysis temperature 973 K and 31/60/9 at 1273 K, respectively. According to studies by Leppälahti and Koljonen [220] and Weissinger et al. [221], NH_3 is the main nitrogen-containing intermediate product during biomass pyrolysis. Zhou et al. [39] showed that up to 1-4% of nitrogen is directly converted to NO during biomass pyrolysis. Despite numerous studies on NO_x formation in biomass combustion, there is no general consensus on the ratio of NH_3/HCN/HNCO/NO in the published literature. Based on the above studies, the components containing nitrogen in the pyrolysis products are NH_3, HCN, HNCO, and NO in descending order. NH_3 is the main component of pyrolysis nitrogenous products while the ratio of HCN/HNCO is approximately 2. The mass ratio of NH_3/HCN/HNCO/NO during biomass pyrolysis is estimated to

be 51/31/15/3 in the present work. This ratio is used to determine the model constants x_j in Eq. (6.1).

Simplified homogeneous reactions of volatile gas and heterogeneous reactions of char used in this study are listed in Table 6.1. In this model, thermal NO formation is neglected because the maximum temperature in the furnace is lower than 1600 K, i.e., fuel-NO_x from nitrogen in the biomass is the main source of NO_x formation. This chemical kinetic model is selected mainly due to its high computational efficiency. The NO chemistry (R9–R16) has been used by Zhou et al. [39] to predict NO formation in straw combustion in a fixed bed furnace showing good accuracy.

Table 6.1: Homogeneous and heterogeneous reactions considered in biomass combustion and gasification. Note: $C_{(s)}$ is solid phase char. C_k represents the molar concentration of gas species k.

Reference	Reactions	Reaction rate [Kmol/m³/s]
R1 [194, 199]	$CH_4 + H_2O \rightarrow CO + 3H_2$	$0.312 exp(\frac{-15,098}{T_g})C_{CH_4}C_{H_2O}$
R2 [194, 199]	$CO + H_2O \rightarrow CO_2 + H_2$	$2.5 \times 10^8 exp(\frac{-16,597}{T_g})C_{CO}C_{H_2O}$
R3 [194, 199]	$CO_2 + H_2 \rightarrow CO + H_2O$	$9.43 \times 10^9 exp(\frac{-20,563}{T_g})C_{CO_2}C_{H_2}$
R4 [194, 199]	$CH_4 + 2O_2 \rightarrow CO_2 + 2H_2O$	$2.119 \times 10^{11} exp(\frac{-24,379}{T_g})C_{CH_4}^{0.2}C_{O_2}^{1.3}$
R5 [194, 199]	$CO + 0.5O_2 \rightarrow CO_2$	$1.0 \times 10^{10} exp(\frac{-15,154}{T_g})C_{CO}C_{O_2}^{0.5}$
R6 [194, 199]	$H_2 + 0.5O_2 \rightarrow H_2O$	$2.2 \times 10^9 exp(\frac{-13,109}{T_g})C_{H_2}C_{O_2}$
R7 [222]	$NH_3 + O_2 \rightarrow NO + H_2O + 0.5H_2$	$1.21 \times 10^9 exp(\frac{-8,000}{T_g})C_{O_2}C_{NH_3}$
R8 [222]	$NH_3 + NO \rightarrow N_2 + H_2O + 0.5H_2$	$8.73 \times 10^{17} exp(\frac{-8,000}{T_g})C_{NO}C_{NH_3}$
R9 [39, 223]	$CH_4 + NO \rightarrow HCN + H_2O + 0.5H_2$	$2.7 \times 10^6 exp(\frac{-9,466}{T_g})C_{NO}C_{CH_4}$
R10 [39, 223]	$CH_4 + NO \rightarrow CO + 2H_2 + 0.5N_2$	$2.7 \times 10^6 exp(\frac{-9,466}{T_g})C_{NO}C_{CH_4}$
R11 [39, 223]	$HCN + 0.5O_2 \rightarrow CNO + 0.5H_2$	$2.14 \times 10^5 exp(\frac{-10,000}{T_g})C_{O_2}C_{HCN}$
R12 [39, 223]	$CNO + 0.5O_2 \rightarrow CO + NO$	$2.14 \times 10^5 exp(\frac{-10,000}{T_g})C_{O_2}C_{HCN}$
R13 [39, 223]	$CNO + NO \rightarrow N_2 + 0.5O_2 + CO$	$1.02 \times 10^9 exp(\frac{-25,460}{T_g})C_{O_2}C_{HCN}$
R14 [39, 223]	$HNCO \rightarrow NCO + 0.5H_2$	$2.14 \times 10^5 exp(\frac{-10,000}{T_g})C_{O_2}C_{HNCO}$
R15 [39, 223]	$NCO + 0.5O_2 \rightarrow NO + CO$	$2.14 \times 10^5 exp(\frac{-10,000}{T_g})C_{O_2}C_{HNCO}$
R16 [39, 223]	$NCO + NO \rightarrow N_2 + 0.5O_2 + CO$	$1.02 \times 10^9 exp(\frac{-25,646}{T_g})C_{O_2}C_{HNCO}$
R17 [146, 204]	$C_{(s)} + 0.5O_2 \rightarrow CO$	$0.046 \times 10^7 exp(\frac{-13,523}{R_u T_i})$
R18 [146, 204]	$C_{(s)} + H_2O \rightarrow CO + H_2$	$1.71 \times 10^7 exp(\frac{-211,000}{R_u T_i})$
R19 [146, 204]	$C_{(s)} + CO_2 \rightarrow 2CO$	$9.1 \times 10^6 exp(\frac{-166,00}{R_u T_i})$

6.2 Numerical methods and computation cases

6.2.1 Numerical scheme

The governing equations are numerically solved using an open-source CFD code, Open-FOAM v6 [224], where the MP-PIC collision model for the discrete phase and the DKM model for the coupled source terms were implemented. Moreover, an efficient cell search algorithm to find the neighboring cells and a strategy of the message passing interface (MPI) for the parallel computation were implemented for DKM. More details about the cell search scheme are given in Chapter 4.

A finite volume method (FVM) was used for the numerical solution of the continuous phase equations. More details about the FVM scheme and the numerical scheme for the solid phase are given in Section 3.3.

6.2.2 Computational cases

The CFD model was applied to simulate the granular flow and combustion process of biomass in an industrial-scale CFB boiler. A schematic illustration of the boiler is shown in Fig. 6.1, where only half of the computational domain is shown in the figure due to the symmetry of the geometry. The boiler has a 110 MW thermal power output. Shown in the figure are the two key parts of the boiler, the furnace (combustion chamber), and the cyclones (for recovery of flying-ash, char, and sand particles).

The furnace section has a height of 30 m ($z-$direction), a width of 8.7 m ($x-$direction), and a depth of 5.4 m ($y-$direction). The primary air inlet is at the bottom of the furnace and 8 secondary air inlets are at the height of $z = 5.5$ m (upper row) and 1.0 m (lower row). The primary air inlet is of a rectangular shape, with a cross-section of 8.7 m $\times$ 2.4 m. The secondary air inlets are of a circle shape, with a diameter of 0.4 m at the lower row and a diameter of 0.475 m at the higher row, see Fig. 6.1. The lower part of the furnace has a trapezoidal shape, with a height of 6.5 m. Further up the furnace has a rectangular cross-section, with a 20 m height and a cross-section of 5.4 m $\times$ 8.7 m. The cyclones are of cylindrical shape and have a height of 9.25 m and a diameter of 4.0 m. The cyclones are connected to the furnace through two pipes of 0.5 m diameter for circulating the solid particles. Flue gas flows to the top box above the furnace where an outlet region is indicated in Fig. 6.1.

Figure 6.1: Computational domain of the 110 MWth industrial-scale CFB boiler. Only half of the computational domain is shown due to the symmetry of the furnace geometry.

The proximate analysis and physical properties of the biomass and sand particles are presented in Table 6.2. The biomass is a mixture of waste wood, wood chips, sawdust, and bark with a mass ratio of 6/3/2/1. A total mass of 60,000 kg of sand particles was fed to the furnace at the start of the simulation. The biomass was supplied to sand-returning pipes just before it gets into the furnace at a mass injection rate of 12.7 kg/s. Other detailed properties of biomass and sand are shown in Table 6.2. The Rosin-Rammler distribution function was adopted to describe the size distribution of the sand and biomass particles. The minimum and maximum sizes of particles are given in Table 6.2. The sand particles are chemically inert while the temperature of sand particles varies in space and time. Biomass particles are modeled as constant density, but their size varies in time during their thermochemical conversion. Biomass particles are removed from the computational domain when burned out.

Table 6.2: Initial biomass and sand particles used in the CFB furnace.

Key parameters	d_i [mm]	ρ_i [kg/m^3]	Cp_i [J/kg·K]	feed rate [kg/s]	total mass [t]	T_i [°C]
Biomass	$0.50 \sim 5$	750	1500	12.70	-	25
Sand	$0.125 \sim 0.5$	2300	860	-	60	800
Ultimate [wt]	C	H	O	N	Ash	
Biomass	0.505	0.0057	0.386	0.0097	0.041	

Table 6.3: Locations of temperature measurement points in the furnace. x and y represent the two horizontal coordinates and z represents the vertical coordinate, see Fig. 6.1.

Location	P1	P2	P3	P4	P5	P6	P7	P8	P9	P10
x [m]	3	0	-3	-3	0	3	-4	4	-4	-4
y [m]	-0.5	-0.5	-0.5	0.5	0.5	0.5	0	1	1	0
z [m]	0.4	0.4	0.4	0.4	0.4	0.4	8.5	9.3	9.3	9.3
Location	P11	P12	P13	P14	P15	P16	P17	P18	P19	P20
x [m]	-4	4	4	-4	-4	-4	-4	4	4	4
y [m]	-1	-1	0	0	-1	0	1	1	0	-1
z [m]	9.3	9.3	9.3	13.5	24.5	24.5	24.5	24.5	24.5	24.5

The boundary conditions are specified as follows. At the primary air and secondary air inlets constant gas velocity and temperature are specified. The fluidization gas from the primary air inlet and secondary air inlets has a temperature of 200 °C. The air supplied from the primary air inlet has a mass flow rate of 15.21 m^3/s and secondary air inlets with a mass flow rate of 22.8 m^3/s. The outlet boundary of the computational domain (as indicated on the left surface of the top box) is assumed to have a fixed-pressure boundary condition, where a zero-gradient condition for other variables is also assumed. The air inflow boundary is prescribed with Dirichlet boundary conditions, where the inlet flow velocity is computed from the mass-flow rate condition. The wall boundary is assumed to be non-slip and at a constant temperature of 1,173 K. The Courant–Friedrichs–Lewy (CFL) number is 0.2 in the iteration of gas phase equations.

The CFD mesh is generated using the ANSYS Workbench v17.2 package. Unstructured grids used in the present study are generated using the ANSYS ICEM v19.1 package. Three sets of unstructured grids were used to evaluate the mesh independence of simulated results. The fine mesh contains 604,634 cells, with 988,551 sand parcels and 100,000 biomass parcels; the medium mesh contains 512,286 cells, with 743,568 sand parcels and 80,000 biomass parcels; the coarse mesh contains 413,541 cells, with 497,781 sand parcels and 50,000 parcels.

Figure 6.2 shows a comparison of mean gas temperature along the centerline of the furnace (i.e., along $z-$direction at $x = 0$ and $y = 0$, see Fig. 6.1). It is shown that the results from the three meshes are rather similar, with the results

from the fine mesh and the medium mesh showing closer agreement. The results from the fine mesh are discussed in the following.
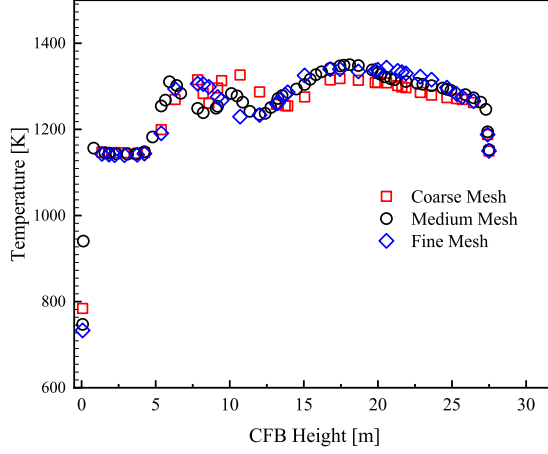
Figure 6.2: Mean gas temperature along the centerline of the furnace ($x = 0$ and $y = 0$).

The gas temperature in the furnace is measured using thermocouples at 20 monitoring locations. The coordinates of the monitoring locations are presented in Table 6.3. The origin of the coordinate is at the center of the primary air inlet as shown in Fig. 6.1. This temperature data will be compared with the numerical results in the following section.

6.3 Results and discussion

First, numerical simulation using MP-PIC coupled with PCM (without the use of DKM) was used to simulate the dense particle flow and combustion process in the furnace. It was found that the numerical simulation quickly diverged and no solution was obtained. The MP-PIC with DKM could give a stable numerical solution. Thus, the particle local overloading problem in PCM and DKM is first discussed below.

6.3.1 Performance of PCM and DKM

Particle local overloading can happen when the solid volume fraction θ_s is higher than the physical packing limit in a mesh cell. The physical packing limit refers to the maximum solid volume fraction that the local cell can accommodate. For
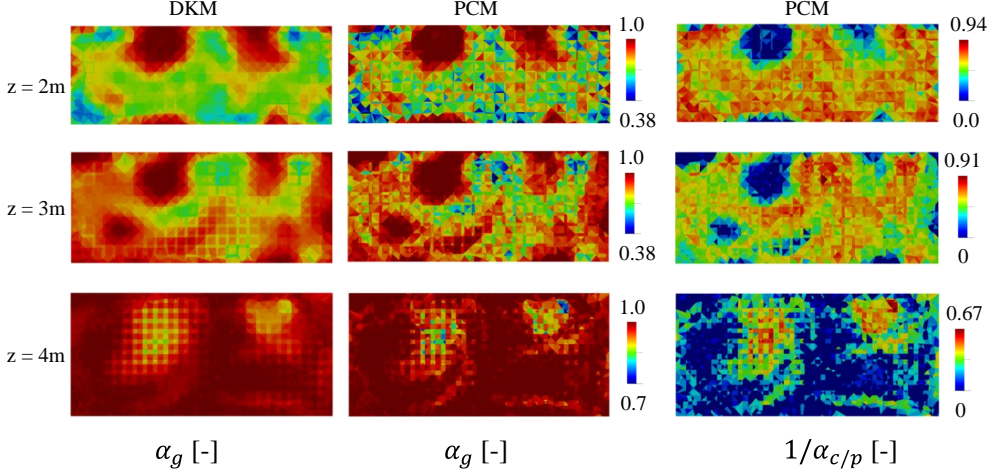
Figure 6.3: Distribution of gas volume fraction α_g and particle load $1/\alpha_{c/p}$ at the different heights of the furnace ($z = 2$, 3 and 4 m), predicted using PCM and DKM.

spherical particles, this limit is about 0.62 [112, 127], which means that the lowest value of gas volume fraction in a cell is 0.38. Figure 6.3 presents the distribution of gas volume fraction α_g with and without the use of DKM, and the local particle load $1/\alpha_{c/p}$ without the use of DKM.

$$\alpha_g = 1 - \frac{V_s}{V_c}, \qquad \alpha_{c/p} = (\frac{V_c}{V_s})^{1/3}, \tag{6.2}$$

where V_c and V_s denote respectively the cell volume and the solid phase volume in the local cell. For the furnace height $z = 2 \sim 4$ m, where the particles are densely located, local overloading is clearly evident. When no DKM is applied (termed as PCM), the local particle load ($1/\alpha_{c/p}$) can be as high as 0.94 at $z = 2$ m. The gas volume fraction in this case is as low as 0.17, which is lower than the physical limit of 0.38. In order to maintain numerical stability and avoid non-physical solutions, a numerical limiter is applied in the OpenFOAM solver, i.e., it is set to the value of 0.38 when $\alpha_g < 0.38$. It is seen that in the PCM calculation, a rather large portion of the domain has applied such a limiter. In the DKM calculation the region needs to apply the limiter is significantly smaller, especially at higher furnace height. The source terms in the PCM method are rather 'noisy', i.e., similar to the distribution of α_g and $1/\alpha_{c/p}$. This is likely the reason that the numerical simulation could not converge. Furthermore, due to the numerical limiter applied to α_g, α_g is numerically increased, causing an error in the numerical solution [127].

Figure 6.4 shows a comparison of the gas temperature at different locations from
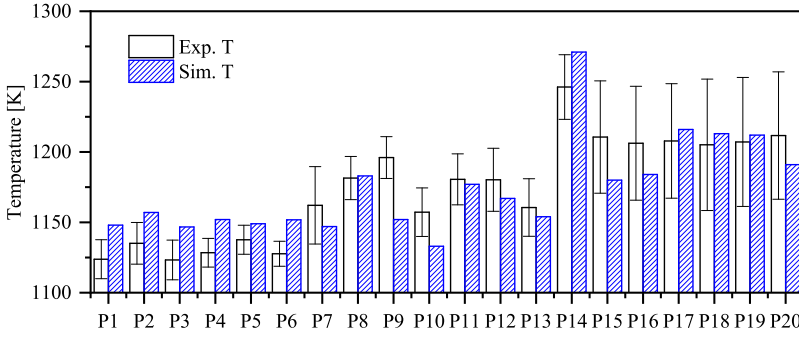
Figure 6.4: Comparison of gas temperature between the numerical simulation using MP-PIC and DKM and experiment of at different monitoring locations. The spatial coordinates of the 20 locations are given in Table 6.3.

numerical simulations using the MP-PIC and CGM/DKM models. As listed in Table 6.3, P1 – P6 is at the fuel-supplying region with $z = 0.4$ m. In this region, the sand and biomass particles exchange heat and the biomass particles start the thermochemical conversion. The temperature of the gas is relatively low in this region, around 1100 K to 1150 K. The gas temperature is rather uniform in the horizontal plane. P7 – P13 is at the furnace height $z = 9.3$ m, which is above the inlets of the secondary air. In this region the gas temperature is higher than that in the fuel-supplying region, indicating that the thermochemical conversion process has progressed and exothermic volatile reactions taking place. The gas temperature at this furnace height is rather non-uniform, varying significantly in the horizontal plane. P7, P10, and P13 are on the symmetric plane with $y = 0$ and near the side wall of the furnace $|x| = 4$ m. The gas temperature is similar and relatively low compared to other locations. P8, P9, P11 and P12 are off the symmetric plane with $|y| = 1$ m and $|x| = 4$ m. The gas temperature in these locations is higher than those on the symmetric plane. P14 is at the furnace height $z = 13.5$ m, where the gas temperature is the highest. Further up in the furnace, $z = 24.5$ m, the gas temperature is slightly lower than that at $z = 13.5$ m, but the gas temperature is rather uniform in the horizontal plane, see P15 – P20. The numerical simulation using the MP-PIC and CGM/DKM is shown to fairly well replicate the experimentally observed trend of gas temperature.

6.3.2 Granular flow and characteristics of fluidization

To understand the temperature distribution discussed above, it is important to know the granular flow and the fluidization process of the sand and biomass particles. An instantaneous distribution of biomass and sand particles in the
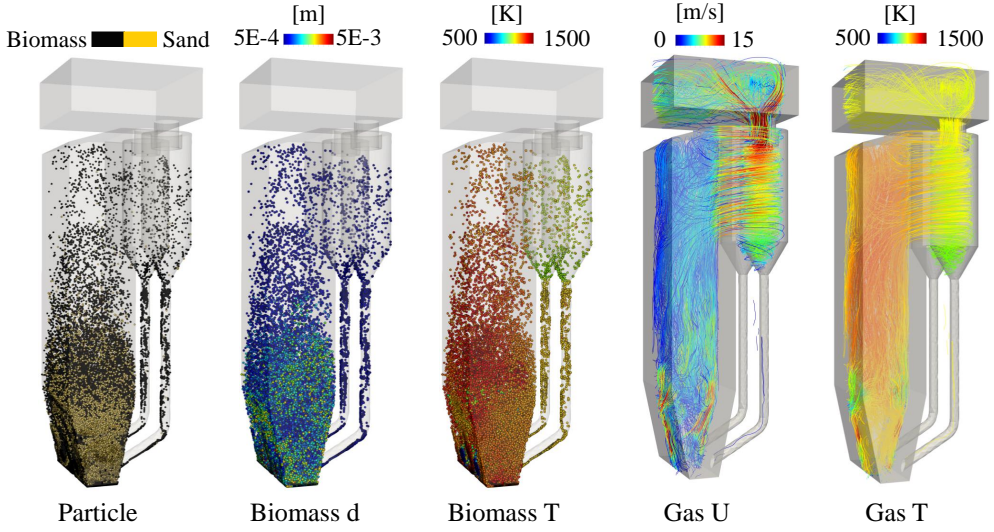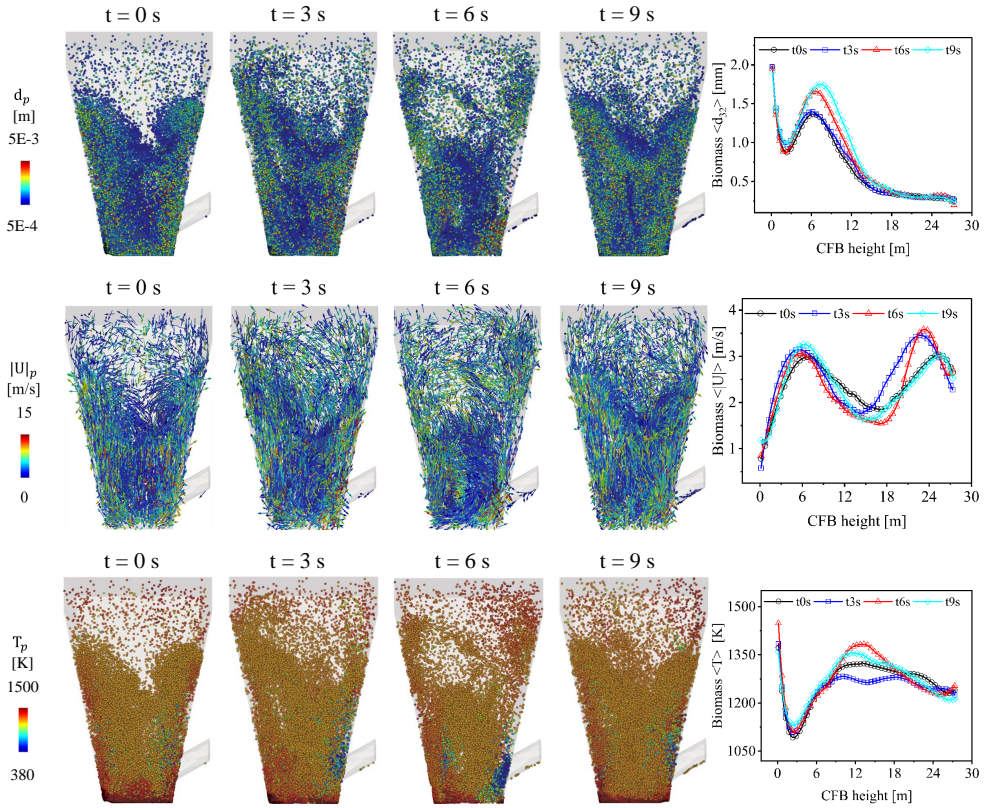
Figure 6.5: Spatial distribution of sand and biomass particles (left panel), biomass particles colored with particle size and temperature (second and third panels), gas flow streamlines colored with gas flow speed and gas temperature (fourth and fifth panels), at an instant of time during the stationary operation stage. The results are obtained using MP-PIC and DKM models.

furnace and in the cyclones is shown in Fig. 6.5. The results are taken at an arbitrary time after the numerical simulation reached a statistically steady state. Also shown in the figure are the distribution of biomass particles colored with their size and temperature, and the gas flow streamlines colored with the gas temperature and gas flow velocity. The sand particles are initially deposited in the lower part of the furnace $z = 0 \sim 6$ m, and the biomass particles are then injected. The fluidization air flow is supplied from the primary air inlet with a velocity of about 1 m/s, and the second air inlet with a higher velocity (> 10 m/s). The sand and biomass particles are fluidized and the quasi-steady-state fluidization is reached after 15 s physical time.

It is clear that the furnace can be divided into two regions, the dense particle region in the lower part of the furnace, within 8 m ($z < 8$ m) above the bottom plane of the furnace, and the dilute particle region further up in the furnace and in the cyclones, i.e., $z > 8$ m. Most particles are located in the dense particle region where the size of biomass particles is relatively larger. The biomass particle temperature is relatively low near the inlet and it is quickly heated up in the dense particle region. The gas flow in the dense particle region is rather complex due to granular flow gas/solid interaction. In the dilute particle region, the gas flow is accelerated when entering the cyclones forming a swirling flow motion. The swirling gas flow shows a 'vortex breakdown' structure when

entering the top-box, where an inner recirculating zone can be found. The gas flow exits the furnace at the outlet located on the left surface of the top-box. The particles in the cyclones are seen to be separated from the gas flow and returned back to the furnace through the two connecting pipes. The gas temperature shows a locally cold region and a hot region in the low part of the furnace, indicating the non-uniform nature of the dense particle region. Further up in the furnace, the gas temperature is more uniform in space. This explains the larger spatial variation of gas temperature observed in the experiments at the furnace height of $z = 9.3$ m (thermocouple locations P8 – P13) and more uniform temperatures at the furnace height of $z = 24.5$ m (thermocouple locations P15 – P20).

Figure 6.6: Spatial distribution of biomass particles in the dense particle region, colored with the particle diameter (upper row) d_{32} and temperature (bottom row), and velocity vector of the biomass particles at $t =0$, 3 s, 6 s, and 9 s. $t = 0$ is an arbitrary time after the flow and combustion process reach statistically steady states. The right panel shows the cross-section averaged Sauter mean diameter (d_{32}) of the particles, the velocity of the particles, and the temperature of the particles along the furnace height at $t =0$, 3 s, 6 s, and 9 s. The results are from numerical simulations using MP-PIC and DKM.

Figure 6.6 shows the instantaneous distributions of biomass particles in the dense particle region at four instants of time. $t = 0$ corresponds to an arbitrary time after the furnace reaches a statistically stationary operation state. Also shown in the figure are the cross-section averaged Sauter mean diameters of biomass particles, and biomass particle velocity and temperature at different furnace heights. Gas bubbles can be identified, e.g., in the bottom row of the figure. The bubble's location and size evolve over time. The gas bubbles in the upper part of the dense particle region are large in size and the bubbles periodically break up (e.g. at $t = 0$) and form (e.g. at $t = 3$ s). It can be seen that larger particles can be found near the bottom of the furnace, due to gravity. These particles move around in the bottom of the furnace, and at the same time, the particles undergo drying, pyrolysis (devolatilization), char oxidation, and gasification. It is seen that the particle temperature is higher near the primary air inlet than that further up in the furnace, due to the exothermic reactions of the particles. When the particles become smaller and lighter they are blown upward in the furnace; hence, the mean diameter of the particles has a tendency to become smaller along the furnace height, i.e., in the region of $0 < z < 3$ m.

At the lower row of the secondary air inlet (close to the furnace height as indicated by the tube connecting the cyclones), the cold fresh biomass particles are injected; thus, the mean temperature in this furnace height is relatively low. It is seen that small particles tend to be found in the center of the furnace where the particle velocity is low, and the larger particles tend to move at a higher velocity and are found in the near wall region around the gas bubbles where the velocity of the gas is higher. These larger particles flowing upward in the furnace around the boundaries of the gas bubbles may be the reason that the mean diameter of the particles increases along the furnace height in the region from the particle inlet to the upper surface of the dense particle region. Further up in the dilute particle region, the biomass particles are smaller and hotter (due to loss of mass during thermochemical conversion). These are mainly char particles. It is worth noting that the bubble formation and breakup are highly unsteady, leading to temporally evolving particle properties (diameter, velocity, and temperature). However, the overall trend of the particle characteristics discussed above is similar at different times, see the right panel of Fig. 6.6.

6.3.3 Thermochemical conversion process of biomass particles

Figure 6.7 shows the cross section averaged gas phase properties: gas temperature T_g, gas pressure drop ΔP_g, and gas velocity, gas volume fraction, and mass fractions of H_2 and CO_2, from numerical simulations. The pressure drop
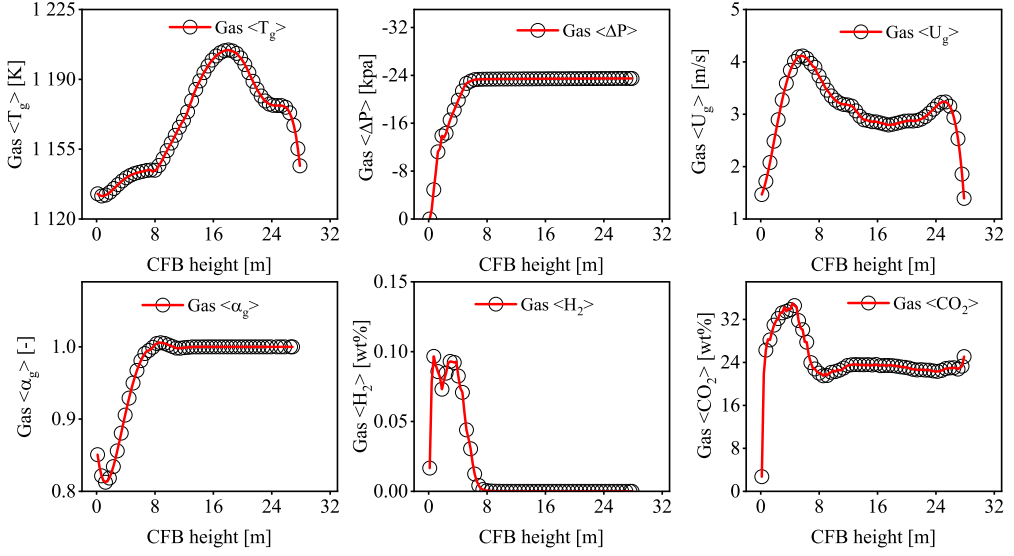
Figure 6.7: Cross section averaged gas properties at different heights of the furnace including gas temperature (T_g), pressure drop (ΔP), gas velocity (U_g), gas volume fraction (α_g), and mass fractions of H_2 and CO_2.

increases along the furnace height, varying rapidly in the dense particle region, reaching a plateau in the dilute particle region, i.e., $z > 8$ m. In the dense particle region, the averaged gas volume fraction varies significantly, becoming nearly 1 in the dilute particle region. The gas temperature increases slowly along the furnace height in the dense particle region. In this region the fuel particles undergo drying and pyrolysis releasing volatile gas such as CO, H_2, and CH_4, along with CO_2 and H_2O, as well char. Combustion of CO, H_2, CH_4, and char in the dilute particle region is the reason that the gas temperature continues to increase along the furnace height until $z = 18$ m, and the rapid decrease of H_2 mass fraction. The rapid decrease of CO_2 in the upper part of the dense particle region is likely due to the rapid mixing with the air that erupted from the gas bubbles. Further downstream the gas temperature decreases a little along the furnace height due to the heat loss to the walls. This result is consistent with the temperature measurement shown in Fig. 6.4, i.e., the highest gas temperature is around P14 ($z = 13.5$ m).

The mean gas velocity (U_g) increases across the dense particle region due to the supply of secondary air in the region. The gas velocity decreases when erupted from the dense particle region, reaching a rather constant flow speed before being accelerated when entering the cyclones, see also Fig. 6.5. The gas velocity profile helps explain the particle velocity shown in Fig. 6.6. It

is clear that in most parts of the furnace, the gas velocity is higher than the particle velocity, indicating that the gas flow is dragging the particles, making the particles accelerate to the gas flow velocity. In the upper part of the furnace the particle velocity at similar to the gas velocity due to the smaller particles that tend to follow the gas flow.
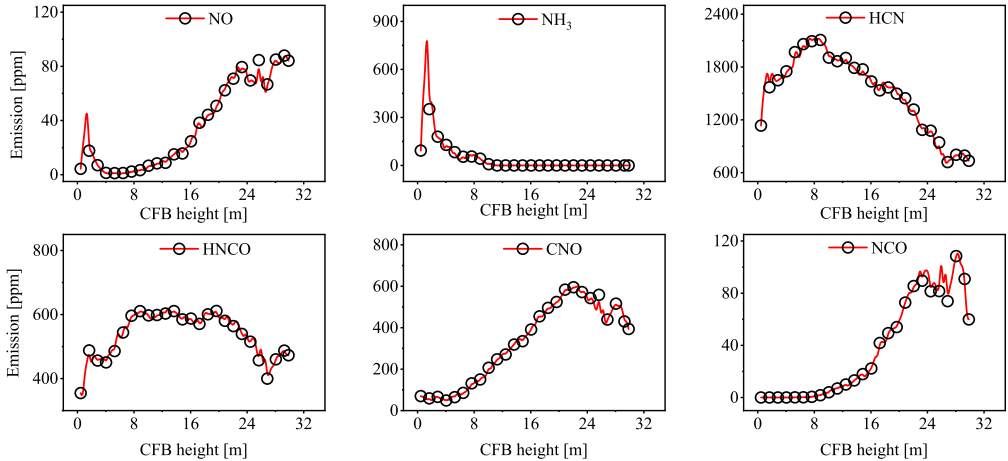
6.3.4 NO$_x$ formation process
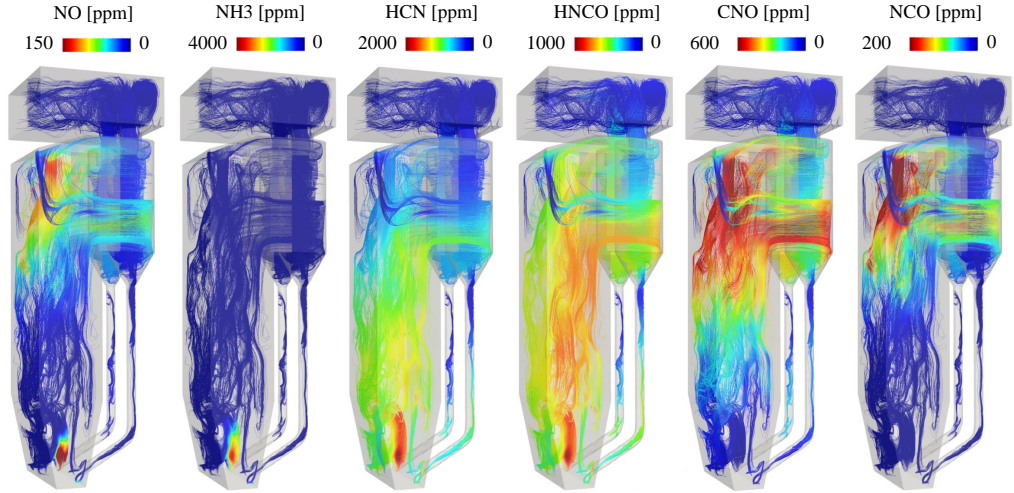
Figure 6.8: Spatial distribution of mass fractions of nitrogen-containing species including NO, NH$_3$, HCN, HNCO, CNO, and NCO at different heights of the furnace.

A spatial distribution of mass fractions of nitrogen-containing species, i.e., NO, NH$_3$, HCN, HNCO, CNO, and NCO, was shown in Fig. 6.8 and cross-section averaged nitrogen-containing species was shown in Fig. 6.9. The NO concentration shows a local peak at $z = 2$ m and then decreases to a low level at $z = 4$-14 m (due to reactions with NH$_3$ and CH$_4$, through reactions R8–R10). This local peak is a result of biomass pyrolysis, which releases NO along with other species in the volatile, see Eq. (6.1) and Fig. 6.8. Further up in the furnace, NO concentration increases gradually and reaches a level of about 80 ppm at $z = 24$-30 m. The formation of NO is mainly in the dilute particle region ($z > 8$ m), due to the oxidation of NH$_3$ (R7), CNO (R12), and NCO (R15).

A similar tendency of NO was observed in the study of Vainio et al. [41], indicating a reasonable prediction in the current simulation. The NH$_3$ concentration shows also a local peak at $z = 2$ m due to the volatile release in the pyrolysis

period. NH_3 is quickly consumed along the furnace height by reactions with O_2 (which forms NO, through reaction R7) and with NO (which consumes NO, i.e. through reaction R8). Above $z = 10$ m, the NH_3 concentration is nearly zero. HNCO and HCN show a tendency to rise first (due to biomass pyrolysis) and then decrease (due to volatile combustion, e.g., R11, R14) along the furnace height. CNO and NCO gradually increase along the furnace height and reach a peak near $z = 24$ m, largely due to volatile combustion (R11, R14).

As a summary, it appears that biomass pyrolysis mainly occurs in the dense region of the furnace ($z < 8$m), leading to extremes of NO, NH_3, HCN, and HNCO, see Eq. 6.1. After pyrolysis, NO was reduced by R8, R9, R10, R13, and R16. After a large amount of air is injected into the secondary inlets, NH_3 is converted to NO by R7 in large quantities, leading to an increase in NO and a decrease in NH_3. Above the secondary air inlets, HCN and HNCO were oxidized and converted to N_2 by R11-R16. It should be noted that the concentrations of NO, as well as CNO and NCO, fluctuate greatly at $z = 24$–30 m due to the interaction with the cyclones, which induced the formation of unsteady rotational flow (swirling flow) structures, as shown in Fig. 6.8.

Figure 6.9: Cross-section averaged mass fractions of nitrogen-containing species at different heights of the furnace including NO, NH_3, HCN, HNCO, CNO, and NCO.

6.3.5   Discussion

The above-detailed information about the granular flow and thermochemical conversion in the CFB furnace can be used to understand the flow and combus-

tion process in the furnace. As discussed above, the NO formation process can be explained using the chemical kinetic model. The bubble formation, breakup process, and division of dense and dilute particle regions can explain the gas temperature field and the interaction of the particles with secondary air.

The CFD simulation can be used to improve the operation of the furnace, e.g., for different biomass fuels, the primary air and secondary air supply may be optimized to achieve better fluidization in the dense particle region and combustion in the furnace.

It should be noted, however, the present CFD results need more thorough validation under industrial CFB boiler operating conditions. Due to the lack of experimental data, the current CFD results are validated against mean gas temperature experimental data at a few sampling locations. More experimental data for the gaseous species and particles in the furnace are desirable for further validation of the model.

6.4 Summary

CFD simulations are carried out to study biomass combustion in an industrial-scale circulating fluidized bed (CFB) boiler. The CFD model is based on the multi-phase particle-in-cell (MP-PIC) collision model (presented in Chapter 3), coarse grain method (CGM, Chapter 2, 3), and the distribution kernel method (DKM, Chapter 4) that aims to solve the local particle overloading problem in the numerical simulation of CFB boilers. The hydrodynamic and combustion properties of the solid and gas phases are analyzed to gain insight into the physical and chemical processes in the furnace. The main conclusions are drawn as follows:

- The CFD model can capture the granular flow and thermochemical conversion processes in the CFB furnace. The predicted temperature field agrees fairly well with the thermocouple experiments. The model is numerically stable and overcomes the local overloading problem.

- The CFB furnace can be divided into different regions according to the characteristics of granular flow. In the lower part of the furnace, there is a dense particle region where most particles are located. In this region, gas bubbles are formed. The gas bubbles evolve in space and time. The bubbles break up close to the dense region's upper boundary. Above the dense particle region is the dilute particle region, where the particles are

smaller and lighter. These particles tend to follow the gas flow. Further downstream, the tiny particles are separated in the cyclones and returned to the furnace through connecting pipes.

- When the biomass particles are supplied to the furnace, the larger particles tend to follow the high-speed gas flow in the boundary of the gas bubbles or to fall to the bottom of the furnace due to gravity. The Sauter mean diameter of the particles is relatively low in the fuel injection region due to the falling of larger particles toward the bottom of the furnace.

- Drying and pyrolysis of the biomass particles occur mainly in the dense particle region. Oxidation of volatile gas and char particles continues in the dilute particle region. This explains that the furnace's highest temperature is in the furnace's mid-height where most of the volatile gas is combusted. Further downstream, the gas temperature becomes more uniform in space, and the gas temperature is slightly lower than that in the mid-height region.

- Biomass pyrolysis in the dense particle region contributes to releasing NH_3, HCH, and HNCO. The combustion of volatile gas further up in the dilute region contributes to converting the nitrogen-containing species to CHO, NCO, and NO.

Chapter 7

Conclusion and future work

7.1 Conclusion

In this thesis, a three-dimensional computational fluid dynamics (CFD) model is developed for the numerical simulation of physical and chemical processes in fluidized bed reactors. The CFD model is based on the multi-phase particle-in-cell (MP-PIC) collision model, the particle centroid method (PCM) coupled with the coarse grain method (CGM), and the distribution kernel method (DKM). In CFD simulation of biomass combustion and gasification in fluidized bed reactors using MP-PIC/PCM/CGM model a challenge is the local particle overloading, which gives rise to non-physical particle and gas volume fraction and frequent failure of achieving a numerical solution. To solve this problem DKM model is developed in this thesis and presented in Chapter 4. In addition to the local overloading issue, the development of a cost-effective chemical kinetic model for biomass pyrolysis is another challenge. In Chapter 5, new development of a one-step semi-empirical pyrolysis model is presented. The CFD model is evaluated for numerical simulations of biomass combustion and gasification in lab-scale bubbling fluidized bed (BFB) furnaces and an industrial-scale circulating fluidized bed (CFB) furnace. The hydrodynamic and combustion properties of the solid and gas phases are analyzed to gain insight into the physical and chemical processes in the furnaces.

The following conclusions are drawn:

- The DKM can effectively handle the particle local overloading problem of MP-PIC/PCM/CGM. The MP-PIC coupled with PCM/CGM gives an

unstable solution if the solid load in a computational cell is high, while the MP-PIC coupled with DKM can improve the numerical instability at higher solid load conditions. Compared with the PCM/CGM, the DKM improves the prediction of gas product yields in biomass combustion/gasification. The DKM is less sensitive to the number of parcels than the PCM/CGM and can achieve mesh-independent results. The CFD model with DKM can capture the transient heat transfer and biomass combustion/gasification processes in BFB reactors. The DKM can be further improved by optimizing the redistribution distance of the kernel function.

- The one-step semi-empirical pyrolysis model can improve the prediction of gasification products with respect to the variation in steam-to-biomass (SR) and operating temperature T_r. As SR and T_r increase within an SR of $0 \sim 2$ and T_r of $800 \sim 900$ °C, the yield of H_2 and CO_2 increase and the yield of CO and CH_4 decrease. The pyrolysis model predicts a better dependence of the gasification products on T_r. The gasification products are affected by the biomass pyrolysis reaction, heterogeneous char reactions, and homogeneous gas reactions. The H_2 yield in the final gasification products and the carbon conversion ratio are strongly affected by the pyrolysis reaction. However, the heterogeneous char gasification reactions and homogeneous volatile gas reactions have also an important impact on the CO, CH_4, and CO_2 concentrations in the final gasification products.

- The CFD model is applied to simulate the granular flow and thermochemical conversion processes of biomass in an industrial fluidized bed furnace. The results indicated that the furnace can be divided into two regions, a dense particle region in the lower part of the furnace and a dilute particle region in the upper part of the furnace. In the dense particle region, gas bubbles form and break up periodically. Larger biomass particles tend to gather in the boundary of the gas bubbles or the bottom of the furnace. The Sauter mean diameter of the particles is relatively low in the fuel injection region. Drying and pyrolysis of the biomass particles occur mainly near the biomass fuel inlets in the dense particle region. The small particles in the upper region of the fluidized bed furnace are mainly char and ash particles. Oxidation of volatile gas and char particles continues in the upper region resulting in the highest temperature in the mid-height of the furnace. Further downstream the gas temperature becomes more uniform in space and the gas temperature is slightly lower than that in the mid-height region.

- NO_x formation in the industrial CFD furnace is investigated. The numerical results indicated that the formation of NO is mainly from the oxidation of nitrogen-containing species in the dilute particle region in the upper part of the furnace. The nitrogen-containing species are released from biomass pyrolysis in the dense particle region in the lower part of the furnace. It is expected that by optimizing the secondary air supply the granular flow structure in the furnace and therefore the dense and dilution regions in the furnace can be optimized to achieve low emissions of NO and other pollutant species.

7.2   Future work

Further work on the development and application of the current CFD model is needed to improve its computational accuracy.

- In the MP-PIC model, the solid particles are considered virtual points in the Eulerian fields, ignoring the effect of the particle's shape on the fluid flow. The interaction between the fluid phase and the solid is through drag force, and pressure gradient, where the boundary of the solid particles is neglected. The impact of particles on the turbulence field is not explicitly considered. Direct numerical simulation (DNS) of gas/particle interaction in fluidized bed reactor conditions is needed to further develop the model.

- CFD results from the MP-PIC method are not entirely grid-independent. It is essential to keep the cell size sufficiently small compared to the macroscopic characteristic length of the system to achieve grid-independent results. However, the cell size should be bigger than the particle size due to the underlying assumption of the method, i.e., the solid volume fraction should be less than a characteristic value. For spherical particles, this value is 0.62. Typically, a $3 \sim 5$ of cell-to-particle size ratio is a compromise choice with reasonable accuracy. The DKM can be further developed to reduce the cell-to-particle size ratio, hence improving the grid-independency of the results.

- The developed biomass pyrolysis model improves the prediction of gasification products at varying operating conditions. However, certain limitations/shortcomings exist in the one-step pyrolysis model, which can be further explored and improved in the future. The one-step pyrolysis model is developed based on the empirical data of the pyrolysis experiments from various biomass fuels under different operating conditions (heating rate,

particle size, etc.). More experimental data are needed to enhance the reliability of the model. Moreover, a comprehensive pyrolysis mechanism of biomass and pyrolysis products (gaseous, char, ash, and tar) needs to be developed to address the complexity of pyrolysis and the impact of biomass composition. The present one-step pyrolysis model is a step forward toward the computation of the pyrolysis products for varying biomass properties (i.e., the element mass fractions of C, H, and O) and operating temperature. However, only seven major pyrolysis products (CO, CO_2, CH_4, H_2, H_2O, C_2H_4 and C_3H_8) could be calculated using the pyrolysis model. When more than seven pyrolysis products are considered, the model cannot be closed due to the requirement for more empirical input. To this end, a multi-step pyrolysis model with low computational cost and a reduced model for tar decomposition in the gas phase is desirable to reveal the underlying pyrolysis mechanism in CFD simulations.

- The three-dimensional numerical simulation of large-scale fluidized beds remains a significant challenge, and there is a need to further reduce the computational cost. Combining high-performance computing and machine learning is an effective means of achieving this. Additionally, the physical and chemical processes within large-scale fluidized beds are highly complex, and strong turbulence leads to a severe anisotropy of the flow field in the bed. The formation of pollutant emissions, particularly NO_x, is significantly affected by primary, secondary, and tertiary air. To accurately simulate this process, it is necessary to develop a more precise NO_x mechanism model, combined with a more efficient three-dimensional computational model. However, the lack of sufficient experimental data presents challenges in establishing accurate models, and more experimental studies on industrial-scale CFB furnaces are desirable.

References

[1] NASA, *Global climate change*, `https://climate.nasa.gov/`, 2022.

[2] W. B. Association, *Global bioenergy statistics 2021*, `https://www.worldbioenergy.org/global-bioenergy-statistics/`, 2022.

[3] M. Van de Velden, J. Baeyens and I. Boukis, 'Modeling CFB biomass pyrolysis reactors', *Biomass and Bioenergy*, vol. 32, no. 2, pp. 128–139, 2008.

[4] A. V. Bridgwater, 'Renewable fuels and chemicals by thermal processing of biomass', *Chemical engineering journal*, vol. 91, no. 2-3, pp. 87–102, 2003.

[5] H. Fatehi, W. Weng, Z. Li, X.-S. Bai and M. Aldén, 'Recent development in numerical simulations and experimental studies of biomass thermochemical conversion', *Energy & Fuels*, vol. 35, no. 9, pp. 6940–6963, 2021.

[6] I. Bioenergy, *Implementation of bioenergy in Sweden – 2021 update*, `https://www.ieabioenergy.com/`, 2022.

[7] Eurostat, *Simplified energy balances, data received from the website of Eurostat (European Commission)*, `https://ec.europa.eu/eurostat/databrowser/view/NRG_BAL_S__custom_3203970/default/table?lang=en`, 2022.

[8] A. Briones-Hidrovo, J. Copa, L. A. Tarelho, C. Gonçalves, T. P. da Costa and A. C. Dias, 'Environmental and energy performance of residual forest biomass for electricity generation: Gasification vs. combustion', *Journal of Cleaner Production*, vol. 289, p. 125 680, 2021.

[9] M. B. Tilghman and R. E. Mitchell, 'Coal and biomass char reactivities in gasification and combustion environments', *Combustion and Flame*, vol. 162, no. 9, pp. 3220–3235, 2015.

[10]   A. Bridgwater, A. Toft and J. Brammer, 'A techno-economic comparison of power production by biomass fast pyrolysis with gasification and combustion', *Renewable and Sustainable Energy Reviews*, vol. 6, no. 3, pp. 181–246, 2002.

[11]   R. Karamarkovic and V. Karamarkovic, 'Energy and exergy analysis of biomass gasification at different temperatures', *Energy*, vol. 35, no. 2, pp. 537–549, 2010.

[12]   D. Kunii and O. Levenspiel, *Fluidization engineering*. Butterworth-Heinemann, 1991.

[13]   J. Werther, 'Fluidized-bed reactors', *Ullmann's encyclopedia of industrial chemistry*, 2000.

[14]   S. Oka, *Fluidized bed combustion*. CRC press, 2003.

[15]   P. Basu and S. A. Fraser, *Circulating fluidized bed boilers*. Springer, 1991.

[16]   F. Liang-Shih, *Gas-liquid-solid fluidization engineering*. Butterworth-Heinemann, 2013.

[17]   R. Jaiswal, C. E. Agu, R. K. Thapa and B. M. E. Moldestad, 'Study of fluidized bed regimes using computational particle fluid dynamics', 2018.

[18]   W.-C. Yang, 'Modification and re-interpretation of geldart's classification of powders', *Powder technology*, vol. 171, no. 2, pp. 69–74, 2007.

[19]   D. Geldart, 'Types of gas fluidization', *Powder technology*, vol. 7, no. 5, pp. 285–292, 1973.

[20]   J. G. Yates, 'Chapter 1 - some fundamental aspects of fluidization', in *Fundamentals of Fluidized Bed Chemical Processes*, ser. Butterworths Monographs in Chemical Engineering, J. G. Yates, Ed., Butterworth-Heinemann, 1983, pp. 4–71, ISBN: 978-0-408-70909-5. DOI: https://doi.org/10.1016/B978-0-408-70909-5.50008-4. [Online]. Available: https://www.sciencedirect.com/science/article/pii/B9780408709095500084.

[21]   F. Alobaid *et al.*, 'Progress in cfd simulations of fluidized beds for chemical and energy process engineering', *Progress in Energy and Combustion Science*, p. 100 930, 2021.

[22]   A. Gómez-Barea and B. Leckner, 'Modeling of biomass gasification in fluidized bed', *Progress in Energy and Combustion Science*, vol. 36, no. 4, pp. 444–509, 2010.

[23]   W. Zhong, A. Yu, G. Zhou, J. Xie and H. Zhang, 'CFD simulation of dense particulate reaction system: Approaches, recent advances and applications', *Chemical Engineering Science*, vol. 140, pp. 16–43, 2016.

[24]   M. Madadi, A. Abbas *et al.*, 'Lignin degradation by fungal pretreatment: A review', *J Plant Pathol Microbiol*, vol. 8, no. 2, pp. 398–404, 2017.

[25]   S. Hameed, A. Sharma, V. Pareek, H. Wu and Y. Yu, 'A review on biomass pyrolysis models: Kinetic, network and mechanistic models', *Biomass and bioenergy*, vol. 123, pp. 104–122, 2019.

[26]   S. V. Vassilev, D. Baxter, L. K. Andersen and C. G. Vassileva, 'An overview of the chemical composition of biomass', *Fuel*, vol. 89, no. 5, pp. 913–933, 2010.

[27]   C. Di Blasi, 'Modeling chemical and physical processes of wood and biomass pyrolysis', *Progress in energy and combustion science*, vol. 34, no. 1, pp. 47–90, 2008.

[28]   L. Fagernäs, J. Brammer, C. Wilén, M. Lauer and F. Verhoeff, 'Drying of biomass for second generation synfuel production', *Biomass and Bioenergy*, vol. 34, no. 9, pp. 1267–1277, 2010.

[29]   W. Yang, D. Pudasainee, R. Gupta, W. Li, B. Wang and L. Sun, 'An overview of inorganic particulate matter emission from coal/biomass/msw combustion: Sampling and measurement, formation, distribution, inorganic composition and influencing factors', *Fuel Processing Technology*, p. 106 657, 2020.

[30]   S. Ozgen, S. Cernuschi and S. Caserini, 'An overview of nitrogen oxides emissions from biomass combustion for domestic heat production', *Renewable and Sustainable Energy Reviews*, vol. 135, p. 110 113,

[31]   H. Cui and J. R. Grace, 'Fluidization of biomass particles: A review of experimental multiphase flow aspects', *Chemical Engineering Science*, vol. 62, no. 1-2, pp. 45–55, 2007.

[32]   P. Lv, Z. Xiong, J. Chang, C. Wu, Y. Chen and J. Zhu, 'An experimental study on biomass air–steam gasification in a fluidized bed', *Bioresource technology*, vol. 95, no. 1, pp. 95–101, 2004.

[33]   A. Svensson, F. Johnsson and B. Leckner, 'Bottom bed regimes in a circulating fluidized bed boiler', *International Journal of Multiphase Flow*, vol. 22, no. 6, pp. 1187–1204, 1996.

[34]   B. Leckner, 'Regimes of large-scale fluidized beds for solid fuel conversion', *Powder Technology*, vol. 308, pp. 362–367, 2017.

[35]   F. Johnsson, R. Zijerveld, J. v. Schouten, C. Van den Bleek and B. Leckner, 'Characterization of fluidization regimes by time-series analysis of pressure fluctuations', *International journal of multiphase flow*, vol. 26, no. 4, pp. 663–715, 2000.

[36] A. Larsson, M. Kuba, T. B. Vilches, M. Seemann, H. Hofbauer and H. Thunman, 'Steam gasification of biomass–typical gas quality and operational strategies derived from industrial-scale plants', *Fuel Processing Technology*, vol. 212, p. 106 609, 2021.

[37] P. Kolbitsch, J. Bolhàr-Nordenkampf, T. Pröll and H. Hofbauer, 'Operating experience with chemical looping combustion in a 120 kW dual circulating fluidized bed (DCFB) unit', *International Journal of Greenhouse Gas Control*, vol. 4, no. 2, pp. 180–185, 2010.

[38] J. Konttinen, S. Kallio, M. Hupa and F. Winter, 'NO formation tendency characterization for solid fuels in fluidized beds', *Fuel*, vol. 108, pp. 238–246, 2013, ISSN: 0016-2361.

[39] H. Zhou, A. Jensen, P. Glarborg and A. Kavaliauskas, 'Formation and reduction of nitric oxide in fixed-bed combustion of straw', *Fuel*, vol. 85, no. 5-6, pp. 705–716, 2006.

[40] S. Mahmoudi, J. Baeyens and J. P. Seville, 'NOx formation and selective non-catalytic reduction (SNCR) in a fluidized bed combustor of biomass', *Biomass and bioenergy*, vol. 34, no. 9, pp. 1393–1409, 2010.

[41] E. Vainio, A. Brink, M. Hupa, H. Vesala and T. Kajolinna, 'Fate of fuel nitrogen in the furnace of an industrial bubbling fluidized bed boiler during combustion of biomass fuel mixtures', *Energy & fuels*, vol. 26, no. 1, pp. 94–101, 2012.

[42] H. Liu, Y. Zhang, H. Wang and C. You, 'Performance of Fe-Ni-W exchanged zeolite for NOx reduction with NH3 in a lab-scale circulating fluidized bed', *Fuel*, vol. 307, p. 121 807, 2022.

[43] Q. Liu, W. Zhong, A. Yu and C.-H. Wang, 'Co-firing of coal and biomass under pressurized oxy-fuel combustion mode: Experimental test in a 10 kWth fluidized bed', *Chemical Engineering Journal*, vol. 431, p. 133 457, 2022.

[44] E. Garcia, M. F. Mejía and H. Liu, 'Fluidised bed combustion and ash fusibility behaviour of coal and spent coffee grounds blends: CO and NOx emissions, combustion performance and agglomeration tendency', *Fuel*, vol. 326, p. 125 008, 2022.

[45] P. R. Wander, F. M. Bianchi, N. R. Caetano, M. A. Klunk and M. L. S. Indrusiak, 'Cofiring low-rank coal and biomass in a bubbling fluidized bed with varying excess air ratio and fluidization velocity', *Energy*, vol. 203, p. 117 882, 2020.

[46] A. Erkiaga, G. Lopez, M. Amutio, J. Bilbao and M. Olazar, 'Influence of operating conditions on the steam gasification of biomass in a conical spouted bed reactor', *Chemical engineering journal*, vol. 237, pp. 259–267, 2014.

[47] H. Hofbauer and R. Rauch, *Stoichiometric water consumption of steam gasification by the FICFB-gasification process.* na.

[48] S. Koppatz, C. Pfeifer and H. Hofbauer, 'Comparison of the performance behaviour of silica sand and olivine in a dual fluidised bed reactor system for steam gasification of biomass at pilot plant scale', *Chemical Engineering Journal*, vol. 175, pp. 468–483, 2011.

[49] N. M. Nguyen, F. Alobaid, J. May, J. Peters and B. Epple, 'Experimental study on steam gasification of torrefied woodchips in a bubbling fluidized bed reactor', *Energy*, vol. 202, p. 117 744, 2020.

[50] S. Rapagnà, N. Jand, A. Kiennemann and P. U. Foscolo, 'Steam-gasification of biomass in a fluidised-bed of olivine particles', *Biomass and bioenergy*, vol. 19, no. 3, pp. 187–197, 2000.

[51] I. Samprón, F. Luis, F. García-Labiano, M. T. Izquierdo, A. Abad and J. Adánez, 'Biomass chemical looping gasification of pine wood using a synthetic Fe2O3/Al2O3 oxygen carrier in a continuous unit', *Bioresource Technology*, vol. 316, p. 123 908, 2020.

[52] T. Song, J. Wu, L. Shen and J. Xiao, 'Experimental investigation on hydrogen production from biomass gasification in interconnected fluidized beds', *Biomass and bioenergy*, vol. 36, pp. 258–267, 2012.

[53] Z. Zhang and S. Pang, 'Experimental investigation of biomass devolatilization in steam gasification in a dual fluidised bed gasifier', *Fuel*, vol. 188, pp. 628–635, 2017.

[54] H. Shahbeik *et al.*, 'Synthesis of liquid biofuels from biomass by hydrothermal gasification: A critical review', *Renewable and Sustainable Energy Reviews*, vol. 167, p. 112 833, 2022.

[55] M. Cortazar *et al.*, 'A comprehensive review of primary strategies for tar removal in biomass gasification', *Energy Conversion and Management*, vol. 276, p. 116 496, 2023.

[56] D. C. de Oliveira, E. E. Lora, O. J. Venturini, D. M. Maya and M. Garcia-Pérez, 'Gas cleaning systems for integrating biomass gasification with fischer-tropsch synthesis-a review of impurity removal processes and their sequences', *Renewable and Sustainable Energy Reviews*, vol. 172, p. 113 047, 2023.

[57] X. Li, J. Grace, C. Lim, A. Watkinson, H. Chen and J. Kim, 'Biomass gasification in a circulating fluidized bed', *Biomass and bioenergy*, vol. 26, no. 2, pp. 171–193, 2004.

[58] X. Ku, T. Li and T. Løvås, 'CFD–DEM simulation of biomass gasification with steam in a fluidized bed reactor', *Chemical Engineering Science*, vol. 122, pp. 270–283, 2015.

[59] S. Wang, K. Luo, C. Hu and J. Fan, 'CFD-DEM study of the effect of cyclone arrangements on the gas-solid flow dynamics in the full-loop circulating fluidized bed', *Chemical Engineering Science*, vol. 172, pp. 199–215, 2017.

[60] J. Gu, Q. Liu, W. Zhong and A. Yu, 'Study on scale-up characteristics of oxy-fuel combustion in circulating fluidized bed boiler by 3D CFD simulation', *Advanced Powder Technology*, vol. 31, no. 5, pp. 2136–2151, 2020.

[61] D. Kong *et al.*, 'Three-dimensional full-loop numerical simulation of co-combustion of coal and refuse derived fuel in a pilot-scale circulating fluidized bed boiler', *Chemical Engineering Science*, vol. 220, p. 115 612, 2020.

[62] J. Lin, K. Luo, C. Hu, L. Sun and J. Fan, 'Full-loop simulation of a 1 MWth pilot-scale chemical looping combustion system', *Chemical Engineering Science*, vol. 249, p. 117 301, 2022.

[63] S. Yang, S. Wang and H. Wang, 'Numerical study of biomass gasification in a 0.3 MWth full-loop circulating fluidized bed gasifier', *Energy Conversion and Management*, vol. 223, p. 113 439, 2020.

[64] S. Li and Y. Shen, 'CFD investigation of maldistribution in a full-loop circulating fluidized bed with double parallel cyclones', *Powder Technology*, vol. 381, pp. 665–684, 2021.

[65] L. Cai, Z. Xu, X. Wang, H. Bai, L. Han and Y. Zhou, 'Numerical simulation and optimization of semi-dry flue gas desulfurization in a CFB based on the two-film theory using response surface methodology', *Powder Technology*, vol. 401, p. 117 268, 2022.

[66] E. Ghadirian, J. Abbasian and H. Arastoopour, 'CFD simulation of gas and particle flow and a carbon capture process using a circulating fluidized bed (CFB) reacting loop', *Powder technology*, vol. 344, pp. 27–35, 2019.

[67] S. Wang, K. Luo, C. Hu, L. Sun and J. Fan, 'Impact of operating parameters on biomass gasification in a fluidized bed reactor: An eulerian-lagrangian approach', *Powder Technology*, vol. 333, pp. 304–316, 2018.

[68] K. Luo, F. Wu, S. Yang, M. Fang and J. Fan, 'High-fidelity simulation of the 3-D full-loop gas–solid flow characteristics in the circulating fluidized bed', *Chemical Engineering Science*, vol. 123, pp. 22–38, 2015.

[69] B.-H. Lee *et al.*, 'Effect of bed particle size on the gas-particle hydrodynamics and wall erosion characteristics in a 550 MWe USC CFB boiler using CPFD simulation', *Energy*, p. 124 263, 2022.

[70] Q. Tu and H. Wang, 'CPFD study of a full-loop three-dimensional pilot-scale circulating fluidized bed based on emms drag model', *Powder Technology*, vol. 323, pp. 534–547, 2018.

[71] T. Kadyrov, F. Li and W. Wang, 'Impacts of solid stress model on MP-PIC simulation of a CFB riser with EMMS drag', *Powder Technology*, vol. 354, pp. 517–528, 2019.

[72] S. Yang and S. Wang, 'Eulerian-lagrangian simulation of the full-loop gas-solid hydrodynamics in a pilot-scale circulating fluidized bed', *Powder Technology*, vol. 369, pp. 223–237, 2020.

[73] A. Muhammad, N. Zhang and W. Wang, 'CFD simulations of a full-loop CFB reactor using coarse-grained eulerian-lagrangian dense discrete phase model: Effects of modeling parameters', *Powder Technology*, vol. 354, pp. 615–629, 2019.

[74] Q. Ma, F. Lei, X. Xu and Y. Xiao, 'Three-dimensional full-loop simulation of a high-density CFB with standpipe aeration experiments', *Powder technology*, vol. 320, pp. 574–585, 2017.

[75] J.-S. Li, L.-T. Zhu, W.-C. Yan, T. A. B. Rashid, Q.-J. Xu and Z.-H. Luo, 'Coarse-grid simulations of full-loop gas-solid flows using a hybrid drag model: Investigations on turbulence models', *Powder Technology*, vol. 379, pp. 108–126, 2021.

[76] S. Liu, H. Wang, F. Jiang and W. Yang, 'A new image reconstruction method for tomographic investigation of fluidized beds', *AIChE Journal*, vol. 48, no. 8, pp. 1631–1638, 2002.

[77] A. Nikolopoulos *et al.*, 'High-resolution 3-D full-loop simulation of a CFB carbonator cold model', *Chemical Engineering Science*, vol. 90, pp. 137–150, 2013.

[78] Y. Lu, Y. Zhou, L. Yang, X. Hu, X. Luo and H. Chen, 'Verification of optimal models for 2D-full loop simulation of circulating fluidized bed', *Advanced Powder Technology*, vol. 29, no. 11, pp. 2765–2774, 2018.

[79] C.-B. Dinh *et al.*, 'Full-loop study of a dual fluidized bed cold flow system: Hydrodynamic simulation and validation', *Advanced Powder Technology*, vol. 32, no. 3, pp. 670–682, 2021.

[80] B. Deng *et al.*, 'Modeling study on the dynamic characteristics in the full-loop of a 350 MW supercritical CFB boiler under load regulation', *Journal of the Energy Institute*, vol. 97, pp. 117–130, 2021.

[81] A. Blaszczuk, A. Zylka and J. Leszczynski, 'Simulation of mass balance behavior in a large-scale circulating fluidized bed reactor', *Particuology*, vol. 25, pp. 51–58, 2016.

[82] F. J. Collado, 'Hydrodynamics model for the dilute zone of circulating fluidized beds', *Powder Technology*, vol. 328, pp. 108–113, 2018.

[83] T. B. Anderson and R. Jackson, 'Fluid mechanical description of fluidized beds. equations of motion', *Industrial & Engineering Chemistry Fundamentals*, vol. 6, no. 4, pp. 527–539, 1967.

[84] D. Gidaspow, *Multiphase flow and fluidization: continuum and kinetic theory descriptions*. Academic press, 1994.

[85] H. Iddir, H. Arastoopour and C. M. Hrenya, 'Analysis of binary and ternary granular mixtures behavior using the kinetic theory approach', *Powder Technology*, vol. 151, no. 1-3, pp. 117–125, 2005.

[86] M. F. Diba, M. R. Karim and J. Naser, 'Fluidized bed CFD using simplified solid-phase coupling.', *Powder Technology*, vol. 375, pp. 161–173, 2020.

[87] ——, 'CFD modelling of coal gasification in a fluidized bed with the effects of calcination under different operating conditions', *Energy*, vol. 239, p. 122 284, 2022.

[88] ——, 'Numerical modelling of a bubbling fluidized bed combustion: A simplified approach', *Fuel*, vol. 277, p. 118 170, 2020.

[89] J. Chen *et al.*, 'Analysis of biomass gasification in bubbling fluidized bed with two-fluid model', *Journal of Renewable and Sustainable Energy*, vol. 8, no. 6, p. 063 105, 2016.

[90] H. Wu, C. Yang, Z. Zhang and Q. Zhang, 'Simulation of two-phase flow and syngas generation in biomass gasifier based on two-fluid model', *Energies*, vol. 15, no. 13, p. 4800, 2022.

[91] Q. Xiong, S.-C. Kong and A. Passalacqua, 'Development of a generalized numerical framework for simulating biomass fast pyrolysis in fluidized-bed reactors', *Chemical Engineering Science*, vol. 99, pp. 305–313, 2013.

[92] A. Ullah, M. B. Shabbir, M. Umair, M. Nadeem and F. Xin, 'Eulerian CFD analysis of clustering gas-solid flows in fluidized bed pyrolysis reactors', *Journal of Analytical and Applied Pyrolysis*, vol. 158, p. 105 261, 2021.

[93] K. Ding, Q. Xiong, Z. Zhong, D. Zhong and Y. Zhang, 'CFD simulation of combustible solid waste pyrolysis in a fluidized bed reactor', *Powder Technology*, vol. 362, pp. 177–187, 2020.

[94] S. Q. Sia and W.-C. Wang, 'Numerical simulations of fluidized bed fast pyrolysis of biomass through computational fluid dynamics', *Renewable Energy*, vol. 155, pp. 248–256, 2020.

[95] P. Mellin, Q. Zhang, E. Kantarelis and W. Yang, 'An Euler–Euler approach to modeling biomass fast pyrolysis in fluidized-bed reactors–focusing on the gas phase', *Applied Thermal Engineering*, vol. 58, no. 1-2, pp. 344–353, 2013.

[96] L. A. Vandewalle, G. B. Marin and K. M. Van Geem, 'Catchyfoam: Euler–Euler CFD simulations of fluidized bed reactors with microkinetic modeling of gas-phase and catalytic surface chemistry', *Energy & Fuels*, vol. 35, no. 3, pp. 2545–2561, 2020.

[97] A. Sharma, S. Wang, V. Pareek, H. Yang and D. Zhang, 'CFD modeling of mixing/segregation behavior of biomass and biochar particles in a bubbling fluidized bed', *Chemical Engineering Science*, vol. 106, pp. 264–274, 2014.

[98] J. Wang, M. A. van der Hoef and J. Kuipers, 'Why the two-fluid model fails to predict the bed expansion characteristics of geldart a particles in gas-fluidized beds: A tentative answer', *Chemical Engineering Science*, vol. 64, no. 3, pp. 622–625, 2009.

[99] J. Wang, 'Continuum theory for dense gas-solid flow: A state-of-the-art review', *Chemical Engineering Science*, vol. 215, p. 115 428, 2020.

[100] Y. Tsuji, T. Kawaguchi and T. Tanaka, 'Discrete particle simulation of two-dimensional fluidized bed', *Powder Technology*, vol. 77, no. 1, pp. 79–87, 1993.

[101] M. Lungu, J. Siame and L. Mukosha, 'Comparison of CFD-DEM and TFM approaches for the simulation of the small scale challenge problem 1', *Powder Technology*, vol. 378, pp. 85–103,

[102] S. Wang, K. Luo and J. Fan, 'CFD-DEM coupled with thermochemical sub-models for biomass gasification: Validation and sensitivity analysis', *Chemical Engineering Science*, vol. 217, p. 115 550, 2020.

[103] T. Qi *et al.*, 'Biomass steam gasification in bubbling fluidized bed for higher-H_2 syngas: CFD simulation with coarse grain model', *International Journal of Hydrogen Energy*, vol. 44, no. 13, pp. 6448–6460, 2019.

[104]   S. Wang and Y. Shen, 'Coarse-grained CFD-DEM modelling of dense gas-solid reacting flow', *International Journal of Heat and Mass Transfer*, vol. 184, p. 122 302, 2022.

[105]   D. Snider, 'An incompressible three-dimensional multiphase particle-in-cell model for dense particle flows', *Journal of Computational Physics*, vol. 170, no. 2, pp. 523–549, 2001.

[106]   M. Andrews and P. O'Rourke, 'The multiphase particle-in-cell (MP-PIC) method for dense particulate flows', *International Journal of Multiphase Flow*, vol. 22, no. 2, pp. 379–402, 1996.

[107]   P. J. O'Rourke, P. P. Zhao and D. Snider, 'A model for collisional exchange in gas/liquid/solid fluidized beds', *Chemical Engineering Science*, vol. 64, no. 8, pp. 1784–1797, 2009.

[108]   C. H. Kruger and W. Vincenti, 'Introduction to physical gas dynamics', *John Wlley & Sons*, 1965.

[109]   P. J. O'Rourke and D. M. Snider, 'An improved collision damping time for MP-PIC calculations of dense particle flows with applications to polydisperse sedimenting beds and colliding particle jets', *Chemical Engineering Science*, vol. 65, no. 22, pp. 6014–6028, 2010.

[110]   P. J. O'Rourke and D. M. Snider, 'Inclusion of collisional return-to-isotropy in the MP-PIC method', *Chemical Engineering Science*, vol. 80, pp. 39–54, 2012.

[111]   J. E. Hilton and P. W. Cleary, 'Comparison of non-cohesive resolved and coarse grain dem models for gas flow through particle beds', *Applied Mathematical Modelling*, vol. 38, no. 17-18, pp. 4197–4214, 2014.

[112]   R. Sun and H. Xiao, 'Diffusion-based coarse graining in hybrid continuum–discrete solvers: Theoretical formulation and a priori tests', *International Journal of Multiphase Flow*, vol. 77, pp. 142–157, 2015.

[113]   Z. Peng, E. Doroodchi, C. Luo and B. Moghtaderi, 'Influence of void fraction calculation on fidelity of CFD-DEM simulation of gas-solid bubbling fluidized beds', *AIChE Journal*, vol. 60, no. 6, pp. 2000–2018, 2014.

[114]   J. Zhang, T. Li, H. Ström and T. Løvås, 'Grid-independent eulerian-lagrangian approaches for simulations of solid fuel particle combustion', *Chemical Engineering Journal*, vol. 387, p. 123 964, 2020.

[115]   M. Farzaneh, S. Sasic, A.-E. Almstedt, F. Johnsson and D. Pallarès, 'A novel multigrid technique for Lagrangian modeling of fuel mixing in fluidized beds', *Chemical Engineering Science*, vol. 66, no. 22, pp. 5628–5637, 2011.

[116]   D. Neves, H. Thunman, A. Matos, L. Tarelho and A. Gómez-Barea, 'Characterization and prediction of biomass pyrolysis products', *Progress in Energy and Combustion Science*, vol. 37, no. 5, pp. 611–630, 2011.

[117]   C. Di Blasi, 'Combustion and gasification rates of lignocellulosic chars', *Progress in energy and combustion science*, vol. 35, no. 2, pp. 121–140, 2009.

[118]   E. Ranzi *et al.*, 'Chemical kinetics of biomass pyrolysis', *Energy & Fuels*, vol. 22, no. 6, pp. 4292–4300, 2008.

[119]   E. Ranzi, P. E. A. Debiagi and A. Frassoldati, 'Mathematical modeling of fast biomass pyrolysis and bio-oil formation. note I: Kinetic mechanism of biomass pyrolysis', *ACS Sustainable Chemistry & Engineering*, vol. 5, no. 4, pp. 2867–2881, 2017.

[120]   H. Fatehi *et al.*, 'Numerical simulation of ignition mode and ignition delay time of pulverized biomass particles', *Combustion and Flame*, vol. 206, pp. 400–410, 2019.

[121]   H. Fatehi, M. Costa and X.-S. Bai, 'Numerical study on K/S/Cl release during devolatilization of pulverized biomass at high temperature', *Proceedings of the Combustion Institute*, vol. 38, no. 3, pp. 3909–3917, 2021.

[122]   Z. Kaczor, Z. Buliński and S. Werle, 'Modelling approaches to waste biomass pyrolysis: A review', *Renewable Energy*, vol. 159, pp. 427–443, 2020.

[123]   H. Luo, X. Wang, X. Liu, X. Wu, X. Shi and Q. Xiong, 'A review on CFD simulation of biomass pyrolysis in fluidized bed reactors with emphasis on particle-scale models', *Journal of Analytical and Applied Pyrolysis*, vol. 162, p. 105 433, 2022.

[124]   H. Luo *et al.*, 'Experimental and modelling study on the influence of wood type, density, water content, and temperature on wood devolatilization', *Fuel*, vol. 260, p. 116 410, 2020.

[125]   M. R. Karim and J. Naser, 'CFD modelling of combustion and associated emission of wet woody biomass in a 4 MW moving grate boiler', *Fuel*, vol. 222, pp. 656–674, 2018.

[126]   M. Gómez, J. Porteiro, D. Patiño and J. Míguez, 'CFD modelling of thermal conversion and packed bed compaction in biomass combustion', *Fuel*, vol. 117, pp. 716–732, 2014.

[127]   M. Yang *et al.*, 'CFD modeling of biomass combustion and gasification in fluidized bed reactors using a distribution kernel method', *Combustion and Flame*, vol. 236, p. 111 744, 2022.

[128] M. Yang, S. M. Mousavi, H. Fatehi and X.-S. Bai, 'Numerical simulation of biomass gasification in fluidized bed gasifiers', *Fuel*, vol. 337, p. 127 104, 2023, ISSN: 0016-2361. DOI: https://doi.org/10.1016/j.fuel.2022.127104. [Online]. Available: https://www.sciencedirect.com/science/article/pii/S001623612203928X.

[129] M. Yang *et al.*, 'CFD modeling of biomass combustion in an industrial circulating fluidized bed', in *Proceeding of the 12th Mediterranean Combustion Symposium*, 2023.

[130] S. B. Pope and S. B. Pope, *Turbulent flows*. Cambridge university press, 2000.

[131] C. Crowe, M. Sommerfeld, Y. Tsuji *et al.*, *Multiphase Flows with Droplets and Particles*. Ž, 1998.

[132] C. E. Brennen and C. E. Brennen, 'Fundamentals of multiphase flow', 2005.

[133] K. Myöhänen and T. Hyppänen, *International Journal of Chemical Reactor Engineering*, vol. 9, no. 1, 2011. DOI: doi:10.1515/1542-6580.2571. [Online]. Available: https://doi.org/10.1515/1542-6580.2571.

[134] R. I. Singh, A. Brink and M. Hupa, 'CFD modeling to study fluidized bed combustion and gasification', *Applied Thermal Engineering*, vol. 52, no. 2, pp. 585–614, 2013.

[135] C. Loha, S. Gu, J. De Wilde, P. Mahanta and P. K. Chatterjee, 'Advances in mathematical modeling of fluidized bed gasification', *Renewable and Sustainable Energy Reviews*, vol. 40, pp. 688–715, 2014.

[136] S. Chapman and T. G. Cowling, *The mathematical theory of non-uniform gases: an account of the kinetic theory of viscosity, thermal conduction and diffusion in gases*. Cambridge university press, 1990.

[137] Q. Eri, X. Zhao, P. Ranganathan and S. Gu, 'Numerical simulations on the effect of potassium on the biomass fast pyrolysis in fluidized bed reactor', *Fuel*, vol. 197, pp. 290–297, 2017.

[138] M. Syamlal, W. Rogers and T. J. OBrien, 'MFIX documentation theory guide', USDOE Morgantown Energy Technology Center, WV (United States), Tech. Rep., 1993.

[139] C. K. K. Lun, S. B. Savage, D. J. Jeffrey and N. Chepurniy, 'Kinetic theories for granular flow: Inelastic particles in couette flow and slightly inelastic particles in a general flowfield', *Journal of Fluid Mechanics*, vol. 140, pp. 223–256, 1984. DOI: 10.1017/S0022112084000586.

[140] D. Z. Zhang and W. B. VanderHeyden, 'The effects of mesoscale structures on the macroscopic momentum equations for two-phase flows', *International Journal of Multiphase Flow*, vol. 28, no. 5, pp. 805–822, 2002.

[141] A. T. Andrews IV, P. N. Loezos and S. Sundaresan, 'Coarse-grid simulation of gas-particle flows in vertical risers', *Industrial & engineering chemistry research*, vol. 44, no. 16, pp. 6022–6037, 2005.

[142] M. A. van der Hoef, M. Ye, M. van Sint Annaland, A. Andrews, S. Sundaresan and J. Kuipers, 'Multiscale modeling of gas-fluidized beds', *Advances in chemical engineering*, vol. 31, pp. 65–149, 2006.

[143] Z. Y. Zhou, S. B. Kuang, K. W. Chu and A. B. Yu, 'Discrete particle simulation of particle–fluid flow: Model formulations and their applicability', *Journal of Fluid Mechanics*, vol. 661, pp. 482–510, 2010. DOI: 10.1017/S002211201000306X.

[144] A. Elfasakhany, L. Tao, B. Espenas, J. Larfeldt and X.-S. Bai, 'Pulverised wood combustion in a vertical furnace: Experimental and computational analyses', *Applied Energy*, vol. 112, pp. 454–464, 2013.

[145] A. Elfasakhany, T. Klason and X.-S. Bai, 'Modelling of pulverised wood combustion using a functional group model', *Combustion Theory and Modelling*, vol. 12, no. 5, pp. 883–904, 2008.

[146] S. Yang, H. Wang, Y. Wei, J. Hu and J. W. Chew, 'Numerical investigation of bubble dynamics during biomass gasification in a bubbling fluidized bed', *ACS Sustainable Chemistry & Engineering*, vol. 7, no. 14, pp. 12 288–12 303, 2019.

[147] S. Ergun and A. A. Orning, 'Fluid flow through randomly packed columns and fluidized beds', *Industrial & Engineering Chemistry*, vol. 41, no. 6, pp. 1179–1184, 1949.

[148] C. Y. Wen, 'Mechanics of fluidization', in *Chem. Eng. Prog. Symp. Ser.*, vol. 62, 1966, pp. 100–111.

[149] R. Di Felice, 'The voidage function for fluid-particle interaction systems', *International journal of multiphase flow*, vol. 20, no. 1, pp. 153–159, 1994.

[150] H. Pan, X.-Z. Chen, X.-F. Liang, L.-T. Zhu and Z.-H. Luo, 'CFD simulations of gas–liquid–solid flow in fluidized bed reactors—A review', *Powder Technology*, vol. 299, pp. 235–258, 2016.

[151] L. Lu, Y. Xu, T. Li and S. Benyahia, 'Assessment of different coarse graining strategies to simulate polydisperse gas-solids flow', *Chemical Engineering Science*, vol. 179, pp. 53–63, 2018.

[152] N. Deen, M. V. S. Annaland, M. A. Van der Hoef and J. Kuipers, 'Review of discrete particle modeling of fluidized beds', *Chemical engineering science*, vol. 62, no. 1-2, pp. 28–44, 2007.

[153] B. Hoomans, J. Kuipers, W. J. Briels and W. P. M. van Swaaij, 'Discrete particle simulation of bubble and slug formation in a two-dimensional gas-fluidised bed: A hard-sphere approach', *Chemical Engineering Science*, vol. 51, no. 1, pp. 99–118, 1996.

[154] B. Hoomans, J. Kuipers and W. P. M. van Swaaij, 'Granular dynamics simulation of segregation phenomena in bubbling gas-fluidised beds', *Powder Technology*, vol. 109, no. 1-3, pp. 41–48, 2000.

[155] B. Hoomans, J. Kuipers, M. M. Salleh, M. Stein and J. Seville, 'Experimental validation of granular dynamics simulations of gas-fluidised beds with homogenous in-flow conditions using positron emission particle tracking', *Powder Technology*, vol. 116, no. 2-3, pp. 166–177, 2001.

[156] F. H. Harlow and A. A. Amsden, 'Fluid dynamics. a lasl monograph.', Los Alamos National Lab.(LANL), Los Alamos, NM (United States), Tech. Rep., 1971.

[157] S. Harris and D. Crighton, 'Solitons, solitary waves, and voidage disturbances in gas-fluidized beds', *Journal of Fluid Mechanics*, vol. 266, pp. 243–276, 1994.

[158] F. Auzerais, R. Jackson and W. Russel, 'The resolution of shocks and the effects of compressible sediments in transient settling', *Journal of Fluid Mechanics*, vol. 195, pp. 437–462, 1988.

[159] C. Di Blasi, 'Modeling and simulation of combustion processes of charring and non-charring solid fuels', *Progress in energy and combustion science*, vol. 19, no. 1, pp. 71–104, 1993.

[160] R. Jenkins, A. Sutton and D. Robichaud, 'Pyrolysis of biomass for aviation fuel', in *Biofuels for Aviation*, Elsevier, 2016, pp. 191–215.

[161] Y. Zhang *et al.*, 'Gasification technologies and their energy potentials', in *Sustainable resource recovery and zero waste approaches*, Elsevier, 2019, pp. 193–206.

[162] S. Vikram, P. Rosha and S. Kumar, 'Recent modeling approaches to biomass pyrolysis: A review', *Energy & Fuels*, vol. 35, no. 9, pp. 7406–7433, 2021.

[163] G. Wang *et al.*, 'A review of recent advances in biomass pyrolysis', *Energy & fuels*, vol. 34, no. 12, pp. 15 557–15 578, 2020.

[164] S. R. Kersten, X. Wang, W. Prins and W. P. van Swaaij, 'Biomass pyrolysis in a fluidized bed reactor. part 1: Literature review and model simulations', *Industrial & engineering chemistry research*, vol. 44, no. 23, pp. 8773–8785, 2005.

[165] H. E. Kissinger *et al.*, 'Variation of peak temperature with heating rate in differential thermal analysis', *J. Res. Natl. Bur. Stand*, vol. 57, no. 4, pp. 217–221, 1956.

[166] T. Akahira, 'Trans. joint convention of four electrical institutes', *Res. Rep. Chiba Inst. Technol.*, vol. 16, pp. 22–31, 1971.

[167] T. Ozawa, 'A new method of analyzing thermogravimetric data', *Bulletin of the chemical society of Japan*, vol. 38, no. 11, pp. 1881–1886, 1965.

[168] X. Ku, T. Li and T. Løvås, 'Eulerian–lagrangian simulation of biomass gasification behavior in a high-temperature entrained-flow reactor', *Energy & fuels*, vol. 28, no. 8, pp. 5184–5196, 2014.

[169] Z. Wang, Y. Teng and M. Liu, 'A semi-resolved CFD-DEM approach for particulate flows with kernel based approximation and hilbert curve based searching strategy', *Journal of Computational Physics*, vol. 384, pp. 151–169, 2019.

[170] A. Anca-Couce, 'Reaction mechanisms and multi-scale modelling of lignocellulosic biomass pyrolysis', *Progress in Energy and Combustion Science*, vol. 53, pp. 41–79, 2016.

[171] Y. Chen, S. Charpenay, A. Jensen, M. A. Wójtowicz and M. A. Serio, 'Modeling of biomass pyrolysis kinetics', in *Symposium (international) on combustion*, Elsevier, vol. 27, 1998, pp. 1327–1334.

[172] A. Frassoldati, G. Migliavacca, T. Crippa, F. Velata, T. Faravelli and E. Ranzi, 'Detailed kinetic modeling of thermal degradation of biomasses', in *Proceeding of the 29th Meeting on Combustion*, 2006.

[173] M. Corbetta *et al.*, 'Pyrolysis of centimeter-scale woody biomass particles: Kinetic modeling and experimental validation', *Energy & fuels*, vol. 28, no. 6, pp. 3884–3898, 2014.

[174] J. Piskorz, D. S. A. Radlein, D. S. Scott and S. Czernik, 'Pretreatment of wood and cellulose for production of sugars by fast pyrolysis', *Journal of Analytical and Applied Pyrolysis*, vol. 16, no. 2, pp. 127–142, 1989.

[175] T. Faravelli, A. Frassoldati, G. Migliavacca and E. Ranzi, 'Detailed kinetic modeling of the thermal degradation of lignins', *Biomass and bioenergy*, vol. 34, no. 3, pp. 290–301, 2010.

[176] M. Luo and B. Stanmore, 'The combustion characteristics of char from pulverized bagasse', *Fuel*, vol. 71, no. 9, pp. 1074–1076, 1992.

[177]   N. M. Laurendeau, 'Heterogeneous kinetics of coal char gasification and combustion', *Progress in energy and combustion science*, vol. 4, no. 4, pp. 221–270, 1978.

[178]   M. Barrio and J. Hustad, 'CO2 gasification of birch char and the effect of CO inhibition on the calculation of chemical kinetics', *Progress in thermochemical biomass conversion*, p. 47, 2008.

[179]   M. Barrio, B. Gøbel, H. Risnes, U. Henriksen, J. Hustad and L. Sørensen, 'Steam gasification of wood char and the effect of hydrogen inhibition on the chemical kinetics', *Progress in thermochemical biomass conversion*, vol. 1, pp. 32–46, 2001.

[180]   K. J. Hüttinger and W. F. Merdes, 'The carbon-steam reaction at elevated pressure: Formations of product gases and hydrogen inhibitions', *Carbon*, vol. 30, no. 6, pp. 883–894, 1992.

[181]   P. Ollero, A. Serrera, R. Arjona and S. Alcantarilla, 'The CO2 gasification kinetics of olive residue', *Biomass and Bioenergy*, vol. 24, no. 2, pp. 151–161, 2003.

[182]   M. Kumar and R. C. Gupta, 'Influence of carbonization conditions on the gasification of acacia and eucalyptus wood chars by carbon dioxide', *Fuel*, vol. 73, no. 12, pp. 1922–1925, 1994.

[183]   C. Branca and C. Di Blasi, 'Global kinetics of wood char devolatilization and combustion', *Energy & Fuels*, vol. 17, no. 6, pp. 1609–1615, 2003.

[184]   C. Branca, A. Iannace and C. Di Blasi, 'Devolatilization and combustion kinetics of q uercus c erris bark', *Energy & fuels*, vol. 21, no. 2, pp. 1078–1084, 2007.

[185]   *ANSYS inc, commercial software*, https://www.ansys.com.

[186]   *Openfoam foundation, Openfoam-the open source CFD tool box-user guide (version 6)*, https://cfd.direct/openfoam/user-guide/.

[187]   *Gerneral public license,http://www.oecd-nea.org*, https://mfix.netl.doe.gov.

[188]   *CPFD software commercial software*, https://cpfd-software.com.

[189]   *CFDEM project general public license*, https://www.cfdem.com.

[190]   *COMSOL inc. commercial software*, http://www.plm.automation.siemens.com.

[191]   *CD-adapco (acquired by siemens plm software) commercial software*, http://www.plm.automation.siemens.com.

[192]   *Altair engineering commercial software*, https://www.altair.com.

[193] J. Chomiak and A. Karlsson, 'Flame liftoff in diesel sprays', in *Symposium (International) on Combustion*, Elsevier, vol. 26, 1996, pp. 2557–2564.

[194] L. Yan, C. J. Lim, G. Yue, B. He and J. R. Grace, 'Simulation of biomass-steam gasification in fluidized bed reactors: Model setup, comparisons and preliminary predictions', *Bioresource Technology*, vol. 221, pp. 625–635, 2016.

[195] W. E. Ranz and W. R. Marshall, 'Evaporation from drops, Part I', *Chemical Engineering Progress*, vol. 48, pp. 141–146, 1952.

[196] T. Hazenberg and J. van Oijen, 'Structures and burning velocities of flames in iron aerosols', *Proceedings of the Combustion Institute*, vol. 38, no. 3, pp. 4383–4390, 2021.

[197] D. Snider, P. O'Rourke and M. Andrews, 'Sediment flow in inclined vessels calculated using a multiphase particle-in-cell model for dense particle flows', *International Journal of Multiphase Flow*, vol. 24, no. 8, pp. 1359–1382, 1998, ISSN: 0301-9322. DOI: https://doi.org/10.1016/S0301-9322(98)00030-5. [Online]. Available: https://www.sciencedirect.com/science/article/pii/S0301932298000305.

[198] P. E. A. Debiagi *et al.*, 'Detailed kinetic mechanism of gas-phase reactions of volatiles released from biomass pyrolysis', *Biomass and Bioenergy*, vol. 93, pp. 60–71, 2016.

[199] L. Yan, Y. Cao, H. Zhou and B. He, 'Investigation on biomass steam gasification in a dual fluidized bed reactor with the granular kinetic theory', *Bioresource technology*, vol. 269, pp. 384–392, 2018.

[200] C. Loha, H. Chattopadhyay and P. K. Chatterjee, 'Three dimensional kinetic modeling of fluidized bed biomass gasification', *Chemical Engineering Science*, vol. 109, pp. 53–64, 2014.

[201] J. C. Wurzenberger, S. Wallner, H. Raupenstrauch and J. G. Khinast, 'Thermal conversion of biomass: Comprehensive reactor and particle modeling', *AIChE Journal*, vol. 48, no. 10, pp. 2398–2411, 2002.

[202] H. Fatehi, M. Costa and X.-S. Bai, 'Numerical study on K/S/Cl release during devolatilization of pulverized biomass at high temperature', *Proceedings of the Combustion Institute*, 2020.

[203] H. Fatehi, Z. Li, X. Bai and M. Aldén, 'Modeling of alkali metal release during biomass pyrolysis', *Proceedings of the Combustion Institute*, vol. 36, no. 2, pp. 2243–2251, 2017.

[204] M. B. Nikoo and N. Mahinpey, 'Simulation of biomass gasification in fluidized bed reactor using aspen plus', *Biomass and bioenergy*, vol. 32, no. 12, pp. 1245–1254, 2008.

[205] J. Capecelatro and O. Desjardins, 'An Euler-Lagrange strategy for simulating particle-laden flows', *Journal of Computational Physics*, vol. 238, pp. 1–31, 2013.

[206] A. Patil, E. Peters and J. Kuipers, 'Comparison of CFD-DEM heat transfer simulations with infrared/visual measurements', *Chemical Engineering Journal*, vol. 277, pp. 388–401, 2015.

[207] C. Loha, H. Chattopadhyay and P. K. Chatterjee, 'Energy generation from fluidized bed gasification of rice husk', *Journal of Renewable and Sustainable Energy*, vol. 5, no. 4, p. 043 111, 2013.

[208] A. V. Patil, E. Peters, V. S. Sutkar, N. Deen and J. Kuipers, 'A study of heat transfer in fluidized beds using an integrated DIA/PIV/IR technique', *Chemical Engineering Journal*, vol. 259, pp. 90–106, 2015.

[209] T. Lichtenegger and T. Miethlinger, 'On the connection between Lagrangian and Eulerian metrics for recurrent particulate flows', *Physics of Fluids*, vol. 32, no. 11, p. 113 308, 2020.

[210] P. Basu, *Biomass gasification and pyrolysis: practical design and theory*. Academic press, 2010.

[211] H. Thunman, F. Niklasson, F. Johnsson and B. Leckner, 'Composition of volatile gases and thermochemical properties of wood for modeling of fixed or fluidized beds', *Energy & Fuels*, vol. 15, no. 6, pp. 1488–1497, 2001.

[212] T. Klason and X.-S. Bai, 'Computational study of the combustion process and no formation in a small-scale wood pellet furnace', *Fuel*, vol. 86, no. 10-11, pp. 1465–1474, 2007.

[213] G.-S. Liu and S. Niksa, 'Coal conversion submodels for design applications at elevated pressures. part II. Char gasification', *Progress in Energy and Combustion Science*, vol. 30, no. 6, pp. 679–717, 2004.

[214] T. Maki and K. Miura, 'A simulation model for the pyrolysis of orimulsion', *Energy & fuels*, vol. 11, no. 4, pp. 819–824, 1997.

[215] N. Hossain and R. Metcalfe, 'Performance analysis of a 2D numerical model in estimating minimum fluidization velocity for fluidized beds', *Particuology*, 2022.

[216] S. Wang, K. Luo, C. Hu, L. Sun and J. Fan, 'Effect of superficial gas velocity on solid behaviors in a full-loop CFB', *Powder Technology*, vol. 333, pp. 91–105, 2018.

[217] F. Winter, C. Wartha and H. Hofbauer, 'NO and N2O formation during the combustion of wood, straw, malt waste and peat', *Bioresource technology*, vol. 70, no. 1, pp. 39–49, 1999.

[218]   R. Bassilakis, R. Carangelo and M. Wojtowicz, 'TG-FTIR analysis of biomass pyrolysis', *Fuel*, vol. 80, no. 12, pp. 1765–1786, 2001.

[219]   K.-M. Hansson, J. Samuelsson, C. Tullin and L.-E. Åmand, 'Formation of HNCO, HCN, and NH3 from the pyrolysis of bark and nitrogen-containing model compounds', *Combustion and Flame*, vol. 137, no. 3, pp. 265–277, 2004.

[220]   J. Leppälahti and T. Koljonen, 'Nitrogen evolution from coal, peat and wood during gasification: Literature review', *Fuel Processing Technology*, vol. 43, no. 1, pp. 1–45, 1995.

[221]   A. Weissinger, T. Fleckl and I. Obernberger, 'In situ FT-IR spectroscopic investigations of species from biomass fuels in a laboratory-scale combustor: The release of nitrogenous species', *Combustion and flame*, vol. 137, no. 4, pp. 403–417, 2004.

[222]   A. Brink, P. Kilpinen and M. Hupa, 'A simplified kinetic rate expression for describing the oxidation of volatile fuel-n in biomass combustion', *Energy & fuels*, vol. 15, no. 5, pp. 1094–1099, 2001.

[223]   W. Ma *et al.*, 'Nox formation in fixed-bed biomass combustion: Chemistry and modeling', *Fuel*, vol. 290, p. 119 694, 2021.

[224]   H. G. Weller, G. Tabor, H. Jasak and C. Fureby, 'A tensorial approach to computational continuum mechanics using object-oriented techniques', *Computers in physics*, vol. 12, no. 6, pp. 620–631, 1998.